Fakultät für Medizin

Nuklearmedizinische Klinik und Poliklinik

Novel High Resolution Photon Detectors for PET Imaging

Ian Andreas Somlai Schweiger

Vollständiger Abdruck der von der Fakultät für Medizin der Technischen Universität München zur Erlangung des akademischen Grades eines

Doctor of Philosophy (Ph.D.)

genehmigten Dissertation.

Vorsitzender: Univ.-Prof. Dr. Arthur Konnerth

Betreuerin: apl. Prof. Dr. Sibylle Ziegler

Prüfer der Dissertation:

1. Univ.-Prof. Dr. Markus Schwaiger
2. Univ.-Prof. Dr. Gil G. Westmeyer

Die Dissertation wurde am 7.11.2014 bei der Fakultät für Medizin der Technischen Universität München eingereicht und durch die Fakultät für Medizin am 12.01.2015 angenommen.

Abstract

Positron emission tomography (PET) is the most specific and sensitive in-vivo imaging technique. Different technical aspects related to the underlying measurement process are involved in the achievement of high resolution images. This thesis addresses, from two different points of view, diverse detector-related factors involved in high resolution PET imaging.

In the first one, newly developed *digital silicon photomultipliers* are characterized. The combination of five different parameters (trigger scheme, validation scheme, cell inhibition, temperature and overvoltage) and their impact on both the intrinsic as well as the PET-oriented performance is analyzed when coupled to two different scintillators, LYSO and GAGG. The results show that detector properties (dependency of breakdown voltage with temperature, optical crosstalk) as well as PET-relevant values (coincidence time resolution (CTR) and energy resolution) are similar to those achievable with state-of-the-art analog devices. The main differences are induced by the logic of the acquisition sequence. Dark-count-rate reduction is mandatory to avoid false-positive events, which induce dead-time and loss in detection sensitivity. This phenomenon is considerably improved by cooling the sensor, enhancing photodetection efficiency and CTR as well.

The second approach is the definition of a novel PET detector with time-of-flight and three-dimensional depth-of-interaction (DOI) abilities detecting only *Cherenkov* photons. The concept relies on the six-sided readout of a cubic crystal to fully benefit from the properties of this radiation. The investigation through theoretical calculations and Monte Carlo simulations of ten different cube sizes showed that a suitable photodetector should be a two dimensional array of micro-cells with high photodetection efficiency. The accuracy of the DOI recognition using the conical Cherenkov geometry depends on the

photodetector's ability to provide individual time-stamps and detection coordinates, as well as on the crystal's refractive index. The latter defines the detector's intrinsic energy-based rejection of scattered PET events. Currently, no photodetectors are able to meet all these requirements, although ongoing developments are already aiming towards sensors featuring some of these characteristics.

To my soon-to-be wife

Acknowledgements

The work presented in this thesis is the result of being immersed in a multidisciplinary and scientifically rich environment. I would first like to thank my supervisor, professor Sibylle Ziegler, for the opportunity to become a member of her research group, for the educational guidance during my thesis work and her constant availability to answer questions. I would also like to thank the members of my thesis committee, professor Markus Schwaiger and professor Gil Westmeyer, for their suggestions and valuable discussions. Thanks a lot to all my current and former colleagues at the Nuclear Medicine Department for both the great work and good times together, especially Florian Schneider, Jorge Cabello, Negar Omidvari, Giaime Rancan, Karl Kunze, Sebastian Fürst, Rupert Trager, Birgit Meißner, Christine Koppenhöhl, Iina Laitinen, Brigitte Dzewas, Michael Herz, Isabel Dregely, Eliane Farrell, Gizem Şeker and Jožef Pulko. Many thanks as well to Taiga Yamaya, Eiji Yoshida and Hideaki Tashima from NIRS and Kenji Shimazoe, Tadashi Orita and Hiroyuki Takahashi from the University of Tokyo for the productive collaborations and very interesting experiences in Japan. Further thanks to Tomás Egaña, Maymi Chávez, Tomás Vega and Cristian Gutierrez for the opportunity to work in their teams to complete my lab rotations. Thanks also to Paul Lecoq, Edoardo Charbon and Erika Garutti for the interesting discussions within the framework of the EU project EndoTOFPET-US, which partially funded my research work. Thanks as well to Ralf Schulze from Philips Digital Photon Counting for his reliable technical support and to Kei Kamada from C&A Corporation for providing the analyzed GAGG crystals. Finally a lot of thanks to Katrin Offe and Desislava Zlatanova from the PhD Program for their always helpful answers and assistance. And last but not least, big thanks to my future wife, family and friends from Chile, Italy and Germany for their support, patience and positive vibes.

Contents

1

Introduction

1.1 Motivation

Positron emission tomography (PET) is the most specific and sensitive in-vivo, non-invasive molecular imaging technique providing quantitative images and data on biochemical pathways, molecular interactions, drug pharmacokinetics and pharmacodynamics in man (1)(2). To achieve this, PET imaging is based on a complex combination of phenomena merging different fields, such as biology, chemistry, physics, engineering, mathematics, informatics, and medicine. Its main clinical application is in oncology, but several examinations are also performed in other areas like cardiology and neurology, while also being widely used in preclinical and basic research.

The underlying principle behind a PET system is the detection of coincidental pairs of high-energetic photons being emitted by a radiolabelled compound, which targets a specific biochemical process in the human body and has been previously delivered to the patient being examined. The outcome of an examination is a tomographic image, with its resolution playing a crucial role in the qualitative identification and precise quantitative analysis of small-scaled processes. In oncology, for example, the size of a tumour is usually related to the developmental stage of the disease. The ability to identify small lesions contributes thus to an early diagnosis and the consequent better prognosis and treatment decision.

Traditional scanners consist of a ring of detector blocks measuring these pairs of high-energy photons, known as gamma-rays, originating within the system's field of view. When these rays hit the crystals inside the detectors, their energy is converted into scintillation light, which is then measured by a photodetector coupled to one face of the crystal. The common emission point of each detected

pair is then assigned to be located along the line of response (LOR) connecting the two coincident detectors. By measuring a large number of LORs, it is possible to reconstruct the origins of the gamma-rays inside the scanner's field of view and thereby the distribution of the radioactivity in the patient.

The term *high resolution* in PET involves different technical aspects related to this measurement process. One of them is the system's *coincidence time resolution* (CTR), which characterizes the accuracy to register the time difference in the detection of both gamma-rays. The CTR of a scanner serves to discard unwanted acquisitions and potentially enhance each event's positioning along its LOR. Another factor is the *energy resolution*, which represents the precision in the measurement of the gamma-ray's energy and contributes to reject unwanted events as well. A third relevant concept is the *depth-of-interaction* (DOI) ability of a PET system. It refers to an improved assignment of LORs, closer to each event's true origin. The *sensitivity* of a PET scanner also affects its achievable resolution through the amount of detected events required to obtain a good image. Finally, the geometrical arrangement between scintillators and photodetectors defines the obtainable spatial resolution, which is ultimately limited by the *crystal's size*. One-to-one coupling schemes using small scintillators allow a better resolution compared to light-sharing schemes with bigger crystals and multiple photodetectors.

The work presented in this thesis addresses these topics and the question of improvement in resolution from two different angles, namely the characterization of newest available detector technology and the development of a novel acquisition concept for PET.

In the first approach, the improvement in terms of CTR, energy resolution and sensitivity offered by recently developed photosensors (*digital silicon photomultipliers*) is thoroughly investigated. Their performance is experimentally evaluated aiming not only for a full understanding of the unprecedented possibilities offered by the newly incorporated technology, but also to assess its real potential towards an implementation in PET.

The second presented strategy is based on the definition of a fundamental change in the underlying detection principle of PET sensors. Instead of the standard conversion of high-energy photons into scintillation light, the newly proposed concept relies on another physical phenomenon known as *Cherenkov radiation*. The advantages and limitations imposed by this alternative light generation mechanism impose a redesign of the detector's geometry and the event acceptance decision. Through computational simulations of ten different crystal

sizes, the new concept's potential for improvements in timing, energy acceptance, DOI and sensitivity is analyzed.

By means of these two approaches, the ultimate goal of the presented thesis is to contribute to a substantial improvement to the state-of-the-art resolution of PET, aiming through this optimization for a positive impact on a broad spectrum of applications.

1.2 Overview

Following the present introduction, this thesis work is divided in three main chapters.

The first of them, *"Introduction to Positron Emission Tomography (PET)"* (chapter 2), explains the underlying principles behind PET imaging. Particular attention is paid to the instrumentation required and its influence on image resolution, to allow a better understanding of the more detailed studies presented in the thesis core, comprised of chapters 3 and 4.

The third chapter, *"Characterization of Digital SiPMs for PET with LYSO and GAGG Scintillators"*, is a thorough performance analysis by means of experimental results using two different scintillators for PET. The effect of the diverse possible sensor configurations within the wide parameter space over the factors affecting image resolution is investigated in detail. Based on the achieved conclusions, the configuration for an optimum outcome is defined considering all studied factors.

Chapter 4, *"Monte Carlo Simulation Study of a novel Cherenkov-Based Detector Block for PET"*, defines a new detector concept for PET. The theoretical background and the principle of the projected idea are initially introduced, followed by the results and corresponding analysis of the executed computational simulations. The potential improvements of the factors affecting the image resolution are presented, together with the current technological bottlenecks for a practical implementation.

Finally, chapter 5 summarises the main results of the developed work, concluding about its main achievements and limitations. In the end, a brief mention to possible enhancements and future work is included.

2

Introduction to Positron Emission Tomography (PET)

2.1 Positron Decay and Radiotracers

The fundament of positron emission tomography relies on the radioactive decay of a positron-emitter atom, known as beta plus decay. This process is summarized by the following equation:

$$p^+ \rightarrow n + e^+ + \nu_e \tag{2.1}$$

where p is a proton from a radioactive atom being converted into a neutron n, a positron e^+ and a neutrino ν_e (3). The emitted positron has an initial energy up to a radionuclide-characteristic maximum. When it passes through matter, it loses kinetic energy and is deflected from its original path due to interactions with other electrons and nuclei. Both the positron's initial energy as well as the surrounding material define thus the range this particle can reach until its complete energy deposition. At that point, the positron annihilates with its antiparticle, an electron, resulting in electromagnetic radiation in the form of two photons of 511 keV each, corresponding to the equivalent rest-mass of each particle. In very few cases, 3 photons can be emitted (<1% probability) (4). Because of momentum conservation, these two photons, also known as gamma-rays, are emitted in opposite directions. However, residual momentum of the positron during annihilation induces a non-collinearity that results in an angle of approximately $180 \pm 0.25°$ between the two photons. This pair of photons is the signal that is detected in a PET scanner. A schematic representation of the

nuclear decay and the generation of the two 511 keV gamma-rays can be seen in figure 2.1:

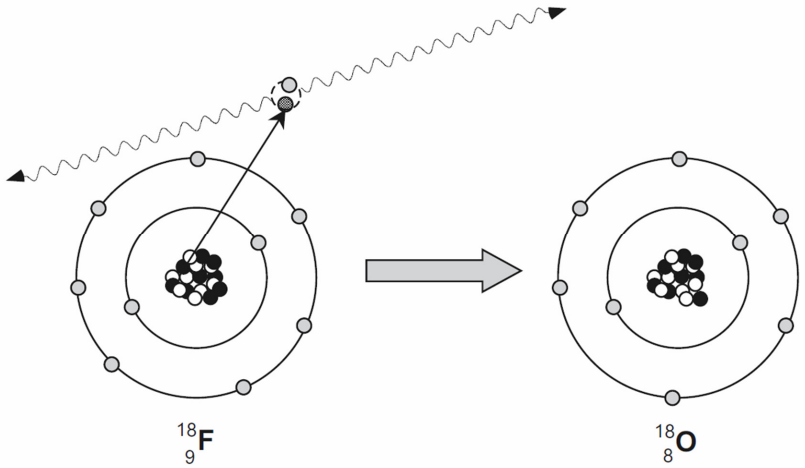

Figure 2.1: Beta plus decay of a $^{18}_{9}$F atom into $^{18}_{8}$O. The emitted positron annihilates with an electron giving rise to two 511 keV antiparallel gamma-rays. Image reproduced from (4).

Figure 2.1 shows the beta plus decay from an unstable atom of radioactive fluorine-18 ($^{18}_{9}$F) into a stable atom of oxygen. ^{18}F is among the most commonly used positron-emitting isotopes for PET, gathering application-suited properties such has short half-life, low positron maximum energy and beta plus as the preferred decay mode, in order to have mainly 511 keV annihilation photons emission. Table 2.1 shows some of the most used nuclides in PET together with these properties.

Nuclide	**Half-life [mins]**	$\mathbf{E}_{max}$ **[MeV]**	$\mathbf{R}^{water}_{mean}$ **[mm]**	**Decay Mode**	**Production**	**Use in PET**
^{11}C	20.4	0.96	1.1	β^+, EC	Cyclotron	^{11}C-CHO
^{13}N	9.96	1.19	1.5	β^+	Cyclotron	$^{13}NH_3$
^{15}O	2.03	1.74	2.5	β^+	Cyclotron	$H_2{}^{15}O$
^{18}F	109.8	0.63	0.6	β^+, EC	Cyclotron	^{18}F-FDG
^{68}Ga	68.3	1.89	2.9	β^+, EC	Generator	^{68}Ga-PSMA

Table 2.1: Properties of positron-emitting nuclides commonly used in PET(4)(5). (E = Energy, R = Range, EC = Electron Capture)

Radionuclides themselves have generally a relative small range of biological

interesting properties (5). Consequently, these are traditionally used to label a compound that does have useful biomedical characteristics, a biomarker. The most attractive radionuclides are those of elements that are found naturally in many biomolecules and can be easily incorporated into the biomarker's molecules, without significantly changing their biochemical properties. Examples of these isotopes are ^{11}C, ^{13}N and ^{15}O, which allow labeling by direct substitution, i.e. replacing a stable atom in the molecule with a radioactive atom of the same element. Another common labeling strategy is the creation of analogs, in which the original compound is modified with an isotope that offers beneficial imaging properties but is not so widely found in nature (e.g. ^{18}F). A third method is to label using a metal such as ^{68}Ga, which is then bound to the biomarker by *chelation*, a technique that shields the metal atom from the biologically active sites of the molecule.

The radioisotopes are usually produced in a cyclotron or a generator and subsequently attached to the biomarker to create the radiotracer. This radiopharmaceutical is then typically injected into the patient and its distribution within the body must be related to the physiological response to measure functionality of the biochemical process under investigation (6). The labeled compounds need to fulfill different common criteria for all PET applications, for example a high affinity for its target (for high-contrast PET images), high specificity (to avoid interaction with other types of molecules) and clearance of non-specifically bound radioactivity within the time scale of the examination (to discriminate between specific and non-specific uptake)(7). Both the isotope's half-life as well as the bound stability of the radioactive label need to match the pharmacokinetics of the biomarker in the body, to encompass the temporal characteristics of the biologic process being analyzed. Furthermore, PET radiotracers must be synthesized and imaged within a time frame compatible with the half-life of the selected radionuclide, to avoid loss of specific activity that is often critical for PET studies (8).

Because of all these practical considerations, only a reduced number of radionuclides are routinely used in clinical practice. The number of labelled compounds, however, is much larger and subject to ongoing development for different applications in nuclear medicine. Among them, the most widely used is ^{18}F-Fluorodeoxyglucose (^{18}F-FDG), an analog of glucose resulting from the replacement with ^{18}F of an hydroxyl (OH) group at the second position of the molecule. FDG undergoes only the first metabolic pathway for glucose, after which the missing OH group, which is needed in normal glucose for further glyco-

lysis, prevents the labeled molecule from being released from the cell. When the fluorine-18 decays into oxygen (see fig. 2.1), a positron is emitted and the resulting molecule is normally metabolized in the same way as normal glucose. Since cancer cells have been shown to have an increased energy demand and thus higher glucose metabolism (9), ^{18}F-FDG has become the gold-standard PET radiotracer for most cancers and their metastases since its invention (10) and first imaging application (11) in the late 1970s. It also has the advantage of the relatively long half-life of ^{18}F, making it possible to be distributed for its application in clinical centers within short distances of a cyclotron-equipped production facility.

An example of a newly developed PET radiotracer is ^{68}Ga-PSMA. The prostate-specific membrane antigen (PSMA) is a cell-surface protein that shows a significant over-expression on prostatic cancer cells, especially in advanced stage prostate carcinomas, and with low expression in normal human tissue (12)(13). Recent clinical studies have demonstrated that ^{68}Ga-PSMA is more specific than the commonly used choline PET tracers, performs better at low PSA values, has a higher uptake by prostate carcinoma lesions and a low background signal (14). In addition to the purely medical benefits, its radioactive label with the generator-produced isotope ^{68}Ga makes its synthesis logistically easier compared to the cyclotron-demanding choline compounds (^{18}F-CHO or ^{11}C-CHO). The combination of these reasons make ^{68}Ga-PSMA likely to become the standard PET radiotracer for clinical routine prostate examinations in the near future.
^{18}F-FDG and ^{68}Ga-PSMA are two examples out of a broad list of existing PET radiotracers, whose possible utilization depends not only on the clinical application but also on the production availability at or near the medical imaging center.

2.2 Image Reconstruction

A PET scanner detects pairs of emitted gamma rays by means of a ring of detectors. Every detected pair of photons is called a coincidence and its originating annihilation position is assigned to have taken place along the *line-of-response* (LOR) connecting the two involved detectors. For the simplified case of only one ring, each LOR can be fully characterized by its orientation inside the scanner plane (angle ϕ) and its distance s from the center of the detector ring. The measured 2D PET raw data is the accumulation of events that were detected on each LOR during the acquisition, i.e., the line integrals of the tracer distribution f, which can be defined as (4):

$$p(s,\phi) = \int_{-\infty}^{\infty} f(x = s\cos\phi - t\sin\phi, y = s\sin\phi + t\cos\phi)\, dt \tag{2.2}$$

where t is the coordinate along the line and (x, y) represents a Cartesian coordinate system centered in the detector's plane. The resulting function $p(s, \phi)$ is called a *sinogram*, since the LORs containing a fixed point (x_0, y_0) constitute a sinusoid described by $s = x_0 \cos\phi + y_0 \sin\phi$ in the (s, ϕ) plane. The mathematical transformation of the function $f(x, y)$ into its line integrals $p(s, \phi)$ (i.e., the conversion of the image into its sinogram) is called the *X-ray transform*, which in 2D coincides with the *Radon transform* (15). The transformation from the detected pair of coincidence photons into a sinogram is graphically shown in figure 2.2:

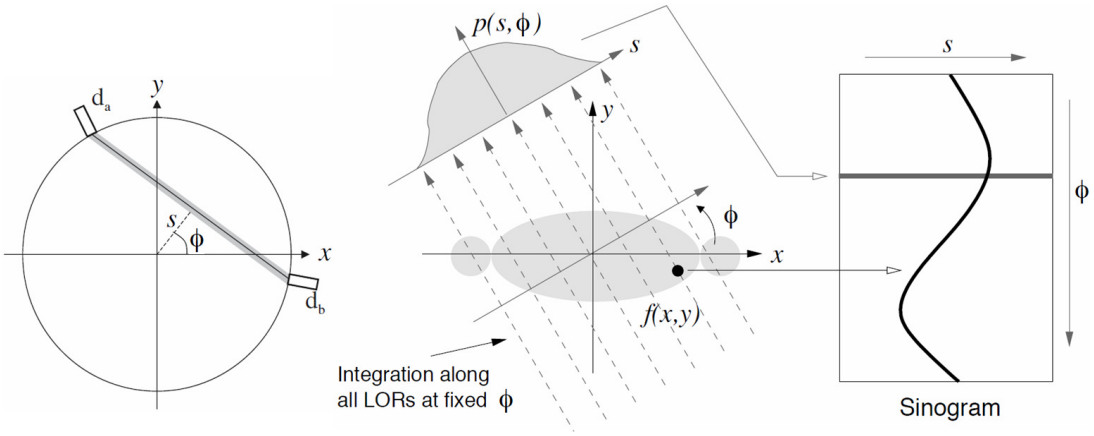

Figure 2.2: Schematic representation of a ring scanner and the LOR between two detectors $d_{a,b}$ (left), the projection $p(s, \phi)$ from the integration of all parallel LORs at an angle ϕ (middle) and the arrangement of all projections into a sinogram (right), showing the correspondence between a point in $f(x, y)$ and the sinusoid in the (s, ϕ) plane. Images reproduced from (4) and (16).

The process of image reconstruction consists in recovering the function $f(x, y)$ knowing its measured projection. Multiple projections from different angular views are needed in order to achieve a *tomographic image*, i.e. a two-dimensional representation of structures that are lying within a selected plane in a three-dimensional object. The outcome data of a PET acquisition are these multiple projections, including noise introduced by the measurement process. The reconstruction of the image starting from these projections obtained from emissions from radionuclides within the body is known as *emission computed tomography* (ECT) (5). The algorithms used in tomographic reconstruction can be divided

into two main categories: analytic and iterative methods. The former essentially apply the inversion of the Radon transform to the measured data, while the latter use models including the characteristics of the imaging system to converge to the original image by means of successive approximations to it. There are different approaches for both methods, and some of their differences and properties are in the following exemplified with one of the most used algorithms for each of the two families.

2.2.1 Filtered Backprojection (FBP)

The most basic approach to reconstruct an image starting from its measured profiles is by *backprojection*. This concept is illustrated for a simplified point source object in figure 2.3:

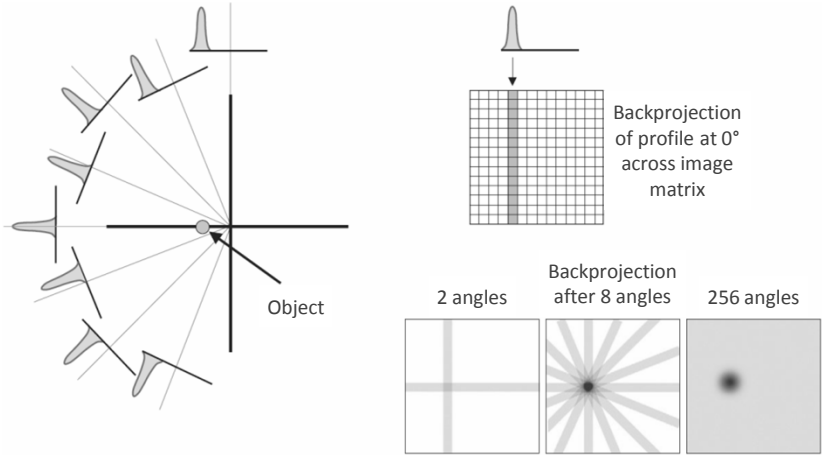

Figure 2.3: Illustration of the backprojection of a point source, showing the measured projection profiles (left) and the result obtained by the backprojection of all profiles into the image grid (right). Image reproduced from (5).

The idea is to obtain an approximation of the registered source distribution by projecting the data from each profile back across the entire image grid. This procedure, called *backprojection*, adds the projections of N profiles together and is mathematically described by the following equation(5):

$$f'(x,y) = \frac{1}{N}\sum_{i=1}^{N} p(x\cos\phi_i + y\sin\phi_i, \phi_i) \tag{2.3}$$

where ϕ_i is the i^{th} projection angle and $f'(x,y)$ the obtained approximation to the true image $f(x,y)$. The larger the number of projections N, the better

the resemblance of the backprojected image with the original one. However, the simple backprojection amplifies low frequencies and damps high frequencies, resulting in blurring of the projected image. To improve this, a filter in the frequency domain is applied to every projection before being backprojected. The resulting *filtered backprojection* (FBP) relies on the *central section* theorem, also called the projection slice theorem, which states that the one-dimensional Fourier transform of a parallel projection of an image f at an angle ϕ is equivalent to the two-dimensional Fourier transform of that image at the same angle along the radial line in the frequency plane. For the reconstruction, this implies that if the projections are measured for all angles $\phi \in [0, \pi]$, then the image f can be reconstructed by the inverse 2D Fourier transform. By this means, it is not only possible to apply a filter to the projections in the frequency domain, but also to analytically compute the inverse of the Radon transform by means of (4):

$$f(x, y) = \int_0^{\pi} p^F(s = x\cos\phi + y\sin\phi, \phi)\, d\phi \tag{2.4}$$

where p^F are the filtered projections, with usually a ramp filter being applied. However, the Radon transform is an ill-posed problem, where an arbitrarily small perturbation of p due to measurement noise can cause an arbitrarily large error on the reconstructed image f. Since the ramp filter amplifies high frequencies that usually contain noise, the FBP can be further stabilized using other adequate filter functions like Shepp-Logan or Hann.

2.2.2 Maximum-likelihood expectation maximization (ML-EM) and Ordered Subsets Expectation Maximization (OSEM)

The global idea of iterative image reconstruction algorithms is shown in figure 2.4. The underlying principle is the successive actualization of an image estimate $f^*(x, y)$, aiming to converge to the true image $f(x, y)$. The algorithm starts with a simple initial estimate, which is then *forward projected* to obtain the projections that would have been measured for the estimated image. The generated sinogram is then compared to the real measured set of projections and the difference between them is used to update the image estimate. The process is then repeated until $f^*(x, y)$ converges to $f(x, y)$ within an acceptable level.

The most widely used iterative algorithms in PET are the *maximum-likelihood expectation maximization* (ML-EM) and its accelerated version OSEM (*ordered*

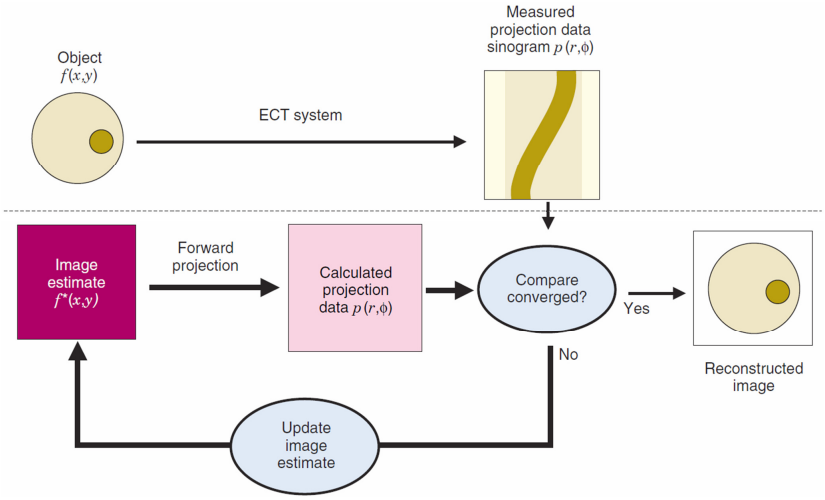

Figure 2.4: Schematic representation of an iterative algorithm. The forward projection of an image estimate is succesively compared to the measured data until the difference between both converges. Image reproduced from (5).

subsets expectation maximization). This numerical approach incorporates statistical considerations to compute the most likely source distribution that would have created the observed projection data. The image estimate is updated from the current f^k onto the next estimate f^{k+1} by (5):

$$f_i^{k+1} = \frac{f_i^k}{\sum_j M_{i,j}} \times \sum_j M_{i,j} \frac{p_j}{\left(\sum_l M_{l,j} f_l^k\right)} \tag{2.5}$$

where $M_{i,j}$ is the *system matrix*, a characterization of the particular imaging system that represents the probability of an emission in the pixel i on the detector plane to be detected in the LOR j. This matrix approach provides a model to relate projection profiles to the underlying source distribution that is more accurate than simple forward projection. The system matrix, crucial for the correctness of the reconstructed image, can be determined by measurements or simulations to take into account any physical effects present during the data acquisition that are thus reflected in p. Equation 2.5 gives the iterated estimation value for every i^{th} pixel over the whole detector ring plane. The term in parentheses is the forward projection summed over all pixels and would equal the measured projection if f^k was the true image. The ML-EM algorithm requires several iterations to converge to the image that best fits the data, starting with the low frequency and then the high frequency components of the image. The latter start to introduce

artifacts, demanding to stop the algorithm after a number of iterations that is usually empirically determined in clinical implementations.

Since every iteration involves a projection and a backprojection, ML-EM is much slower than FBP. Although introduced in 1977 (17) and applied to PET in 1982 (18), the more demanding calculations and thus the time needed to reconstruct an image hindered the application of this method into clinical practice. It was the introduction of OSEM in the mid-1990s (19) that made iterative reconstruction practical. In it, the LOR data are partitioned in S disjoint subsets and the ML-EM iteration is applied in a well-defined order with data from only one subset each time, resulting in an empirically accelerated convergence by a factor $\simeq S$. Nowadays, iterative reconstruction algorithms are executed in powerful processing units such as GPUs (*graphical processing unit*), able to deliver the reconstructed image in a very short time. The combination of improved computer performance and intelligent coding (e.g. exploiting symmetries) has led to a routinely use of iterative algorithms for clinical PET.

Iterative and analytic methods have important differences. While the first ones rely on a discrete representation of both the data and the reconstructed image, the second ones are derived assuming a continuous data sampling and introduce the discrete character of the data a posteriori. In terms of execution time, FBP is much faster than OSEM. However, iterative algorithms improve image quality by allowing more accurate modeling of the data acquisition. Different studies have demonstrated improvements in image signal-to-noise ratio (SNR) with maximum likelihood (ML) algorithms compared to FBP (20)(21), making the reconstructed images easier to interpret and consequently improving tumor detection and localization (22). Nonetheless, the analytic approach remains important due to its linearity, allowing an easier control of the spatial resolution and noise correlations in the reconstruction, a control which is mandatory for quantitative data analysis (4).

The fundaments of image reconstruction presented here can be expanded to several detector rings (3D PET) as well as include correction methods for physical phenomena such as attenuation, scatter, radiotracer half-life, variations in detector efficiency, etc. It is worth noting that PET image reconstruction assumes perfect collinearity between the two generated 511 keV photons. Therefore, the $\pm 0.25^{\circ}$ non-collinearity (see section 2.1) introduces an intrinsic limitation to the maximum achievable spatial resolution, being more relevant for PET systems with a larger field-of-view. The positron range until annihilation causes the detected LOR to be displaced from the actual position of the atom decay, originating

another fundamental limitation for the system's spatial resolution.

2.3 PET Detectors

As explained in the previous sections, PET relies on the detection of 511 keV gamma-rays originating by annihilation inside the imaged object. To achieve this, a detection system is needed that is able to measure these high-energetic photons and convert them into a processable electric signal, while extracting characteristics such as their energy and time of arrival. Different types of radiation detectors have been implemented for PET, like proportional gas chambers, semiconductor detectors and scintillation-based detectors. The latter are by far the most commonly used in PET scanners, first converting the high-energy photons into visible light, which is then measured and further analyzed. In the following, the properties and functionality of this kind of PET detectors and the different possible configurations are explained. For a better understanding, a brief explanation is presented of the different mechanisms through which the 511 keV annihilation photons transfer their energy to matter.

2.3.1 Interactions of PET gamma-rays with matter

High-energy radiation interacts with matter by transferring its energy partially or completely to the material. At the energy levels of interest for PET (below 1 MeV), the annihilation generated gamma-rays interact with matter mainly by two mechanisms: the *photoelectric effect* and *Compton scattering*. A representation of both can be seen in figure 2.5.

The photoelectric effect is an interaction in which the high-energetic photon transfers all of its energy to one electron of an atom, usually from the inner shell. The absorbed energy serves to overcome the electron's binding potential and to eject it with the remaining energy in form of kinetic energy. The vacancy left by the emitted photoelectron is occupied by an outer orbital electron, which then emits the difference in binding energies in form of radiation known as a *characteristic X-ray*. As an alternative to this emission, the atom may remove the energy by ejecting a second electron, known as Auger electron.

In Compton scattering, the photon interacts with an outer orbital electron, whose binding potential is much smaller than the photon's energy. The interaction results in the ejection of that electron (known as Compton recoil electron) and a path deflection of the photon, whose energy loss equals that of the elec-

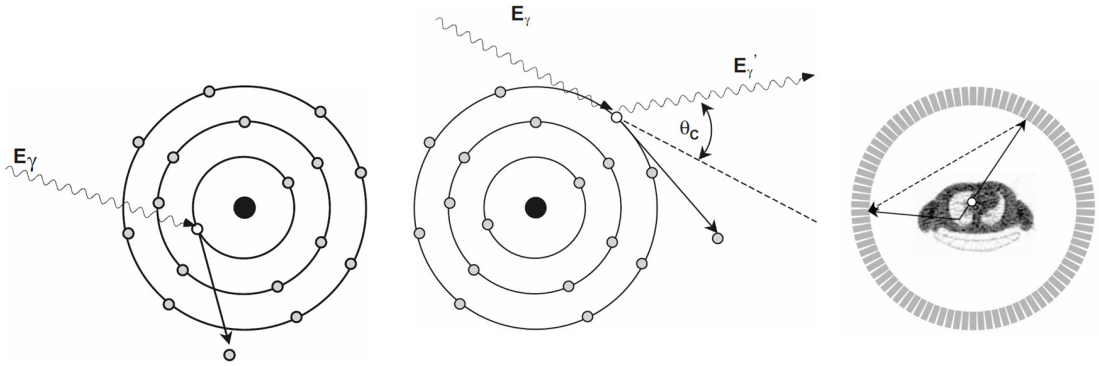

Figure 2.5: Interaction of a gamma-ray with an atom of matter by means of photoelectric effect (left) and Compton scattering (middle). The figure on the right shows the wrongly allocated LOR for a scattered photon. Images reproduced from (4).

tron's small binding energy and its gained kinetic energy. The remaining energy E'_γ is related to the deflection angle by the following equation (4):

$$E'_\gamma = \frac{E_\gamma}{1 + \frac{E_\gamma}{m_0 c^2}\,(1 - \cos\theta_C)} \tag{2.6}$$

where $m_0 c^2$ is the electron rest mass and θ_C the scattered angle as shown in figure 2.5. The probability of Compton scattering, which is not equal for all energies or angles, is given by the *Klein-Nishina* equation (23).

For both described phenomena, the ejection of an electron causes ionisation of the atom. In human tissue, the photoelectric effect predominates over Compton scattering at energies below 100 keV, having thus little impact at the 511 keV energy of annihilation photons. Nonetheless, the physics behind photoelectric interactions is relevant for the attenuation correction of PET data in combined PET/CT systems, where the measured X-ray attenuation factors are adequately adjusted to the 511 keV radiation.[1] On the other hand, at energies above 100 keV, Compton scattering in tissue plays an important role in PET, since a detected scattered photon is assigned to a mismatching LOR (see figure 2.5). If the measured energy of a detected photon is below a certain threshold, it is considered to have undergone a considerable scatter in the imaged object and thus usually discarded as valid data. These two mechanisms occur not only within the imaged object, but also inside the PET detectors, as explained in the following section.

[1] Attenuation correction is an important topic in PET imaging, which is out of the scope of this work. An introduction to it can be found, among others, in (4) or (5).

2.3.2 Scintillators

The interaction of 511 keV photons with matter results in the ionization of atoms and molecules, which then release energy after undergoing recombination or de-excitation. A scintillator is a particular kind of material that releases this energy in form of visible light, whose amount is proportional to the energy deposited in it by the incident ionizing radiation (here gamma-rays). Therefore, a high-energy photon that interacts with the scintillator by photoelectric effect produces more light than that by a Compton scatter in the same material. For PET, scintillators are usually inorganic crystalline solids. In the crystal lattice, electrons are allowed to have discrete energy levels called *allowed bands*, separated from each other by the *forbidden bands*. Through an atomic interaction with the photoelectron or the Compton recoil electron, electrons from the *valence band* (the last one filled) can absorb enough energy to get into the *conduction band* (the first unfilled one). The electron consequently de-excites to come back to its ground state by releasing scintillation photons, which are usually in the ultraviolet range due to the high value of the energy gap between the bands. By adding impurities to the scintillator material, further intermediate energy levels in the forbidden band are included. These so called *activator states* reduce hence the energy gap, resulting in scintillation photons in the range of visible light. This emitted optical light is the one detected later on by the photodetectors used in PET (see next section). Scintillation photons are emitted isotropically from the point of interaction and in a material-dependent amount, ranging from several hundred up to some tens of thousands at the PET radiation energy levels. The emission is timely distributed, with a sharp rising edge (e.g., a reduced portion of photons) usually in the range of tens of picoseconds (24)(25) and a much slower decay tail in the nanoseconds range.

The scintillator itself needs to fulfill different properties for its application in PET. First, it needs to maximize the number of high-energetic photons that interact with it, preferably by photoelectric effect. This so called *stopping power* of a scintillator is determined by the mean distance travelled by the gamma-ray until its energy deposition in the crystal. This is determined by the attenuation length of the material, which depends on its density ρ, the effective atomic number Z_{eff} and the size of the crystal. The stopping power is crucial for a PET scanner with high sensitivity. Besides, higher Z_{eff} values favor the interaction by photoelectric effect ($\propto Z^4$) over Compton scattering ($\propto Z$)(26). Another important characteristic is the scintillator's decay constant, which affects the timing characteristics

of the scanner. A short decay time is not only important to process each scintillation pulse individually at high activity rates, but also to reject coincidences due to randomly detected gamma-rays (see section 2.4.2). Also the light yield per amount of deposited energy is important. A bright scintillator can help to improve spatial resolution for particular detector configurations (see section 2.3.4) and, more generally, to achieve good energy resolution (see section 2.4.3). The energy resolution achieved by a PET detector, i.e. the combination of a scintillator and a photosensor, is highly influenced by the scintillator's intrinsic energy resolution, defined by inhomogeneities in the crystal growth process as well as non-uniform light output for interactions within it. Furthermore, a scintillator needs to be transparent to its own scintillation photons, to avoid self-absorption, and its emission wavelength profile should be compatible with the photosensor. Table 2.2 shows the properties of some commonly used scintillators in PET.

Property	**NaI(Tl)**	**BGO**	**LSO**	**GSO**
Density [g/cm^3]	3.67	7.13	7.4	6.71
Effective Z	50.6	74.2	65.5	58.6
Attenuation Length at 511 kev [cm]	2.88	1.05	1.16	1.43
Decay Constant [ns]	230	300	40	60
Light Yield [photons/MeV]	38000	6000	29000	10000
Peak Wavelength λ [nm]	410	480	420	440
Intrinsic ΔE/E [%]	5.8	3.1	9.1	4.6
Ratio Photoelectric to Compton	0.22	0.78	0.52	0.35
Index of refraction	1.85	2.15	1.82	1.85
Hygroscopic	Yes	No	No	No

Table 2.2: Commonly used PET scintillators and its physical properties(4)(27).

The first PET scanners were built using NaI(Tl) crystals (sodium iodide doped with thallium), which was the first scintillator available and reliably producible at large scales. It offered good energy resolution due to its high light yield, but a low stopping power and slow decay time. Eventually BGO (bismuth germanate) became available and turned into the most used scintillator for PET scanners due to its high detection efficiency at 511 keV. Although slightly slower and less bright than NaI(Tl), it also has the added benefit of being non-hygroscopic, making its implementation considerably easier. New PET systems are nowadays produced using LSO (lutetium oxyorthosilicate doped with cerium) (28) or the very similar LYSO (cerium doped lutetium-yttrium oxyorthosilicate), a scintillator combining

the advantages of the high light output of NaI(Tl) and the high stopping power of BGO. However, besides having an intrinsic energy resolution that is not as good as NaI(Tl), LSO has a naturally occurring radioactive isotope (^{176}Lu, 2.6% abundance) that emits low-energy gamma-rays. This background radiation is normally filtered out by the energy acceptance windows applied in PET. Some commercial systems have also been developed with GSO (gadolinium oxyorthosilicate), achieving better energy resolution than LSO although less bright and with lower stopping power.

New scintillator materials are continuously being developed and its potential for PET being evaluated. An example of it, compared to LSO, is the very fast and brighter but less dense and hygroscopic $LaBr_3$ (cerium doped lanthanum bromide), which has been used to build a time-of-flight PET system (29) (see section 2.4.2). Another example is GAGG (cerium doped gadolinium aluminum gallium garnet) (30), a very bright scintillator whose performance for PET is analyzed in chapter 3.

A different mechanism for visible light generation due to interaction of high-energetic photons with matter is the *Cherenkov radiation*. The very low number of produced Cherenkov photons by an interacting 511 keV gamma-ray has hindered its exploitation for PET. However, the latest technological developments have already allowed to realize measurements with a PET-like sensor configuration based on this phenomenon. Its properties, advantages and challenges together with a new detection concept for PET are explained in detail in chapter 4.

2.3.3 Photosensors

The photodetectors in a PET scanner are the sensors responsible of converting the scintillation light into a measurable electrical signal. For scintillator-based PET applications, they are usually either *photomultiplier tubes* (PMTs) or semiconductor-based photodiodes. The basic structure and working principle of both is shown in figure 2.6.

PMTs are the most common photosensors being applied in commercially available PET systems. An impinging optical photon entering the device excites the photocathode, a thin layer of a material that easily releases an electron by photoelectric effect. This photoelectron is then accelerated towards a first dynode by means of a strong electric field that is applied along the vacuum enclosed structure. The positively charged dynode is impacted by the electron, releasing on the order of 3 to 4 secondary electrons. These are then focused and accelerated

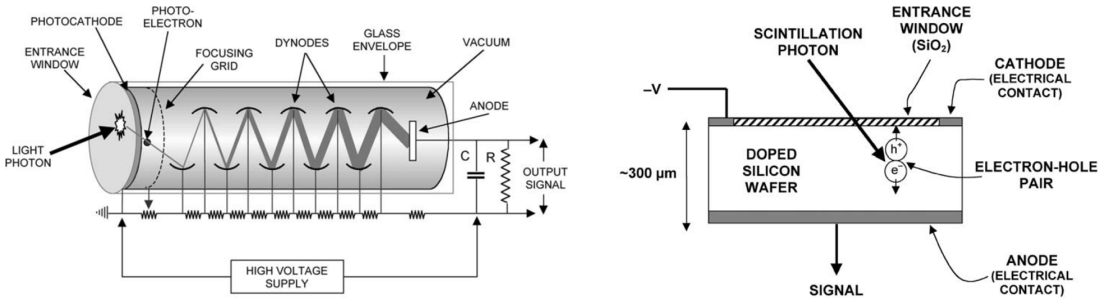

Figure 2.6: Basic structure and working principle of a photomultiplier tube (left) and a semiconductor-based photodiode (right). Images reproduced from (27).

towards a second dynode stage, which upon impact multiplies them again. By means of successive dynode stages, the resulting avalanche of electrons is finally amplified at the output anode to the order of 10^6 electrons, creating a detectable current in the milliamp range. Herewith, the magnitude of the output signal is related to the number of scintillation photons being detected, thus correlated to the amount of energy deposited by the gamma-ray in the scintillator. PMTs for PET have an entrance window with dimensions in the range of some centimeters and are available in different shapes, with some models also including multichannel readout or position sensitive abilities. The main advantages for PET are the high gain obtained, that leads to a very good signal-to-noise-ratio (SNR) for the low light levels emitted by the crystal, and their fast response. However, besides being expensive and bulky for their integration in systems with a large number of densely packed channels, the probability of emission of a photoelectron at the photocathode is in the range of only 25% (27). This parameter is the *quantum efficiency* of a PMT and is crucial to improve the detection efficiency of a PET detector and, consequently, of the system. Additionally, the PMT performance is considerably disturbed in the presence of a magnetic field.

The latest PET systems are being equipped with semiconductor photodetectors instead of PMTs. These are based on the silicon photodiode and have high sensitivity to detect the low-energy scintillation photons. The basic structure of the device (see figure 2.6) is a thin piece of silicon in the range of hundreds of micrometers which has been doped with impurities to create a favorable electric field across its profile. An impinging scintillation photon has sufficient energy to produce an electron-hole pair in the detector that, under the applied electric field, constitutes a small electrical current that can be externally measured. The problem introduced by the extreme low internal gain and high noise levels was

solved by the development of *avalanche photodiodes* (APDs). An APD is a p-n semiconductor device with intrinsic gain due to the high internal field at the junction of positive and negative doped silicon (31). A photoelectron, created by the impact of a scintillation photon, gains enough energy in this field to create an electron-hole pair. The electrons are then highly accelerated, creating further electron pairs and, consequently, an avalanche. The electric field is not too high to prevent the accelerated holes from creating additional pairs, avoiding so a breakdown of the device. This results in a moderate amplification of a factor 50 to 200, with higher gains being possible although difficult to operate stably. APDs have a quantum efficiency up to 80% (i.e. superior than PMTs) and are available as single-units, with sizes ranging from 1 mm up to some centimeters, as well as multi-channel arrays. Although their gain is some orders of magnitude lower than PMTs, they have been successfully implemented in PET systems with limited space, such as in high-resolution animal PET systems (32), or when operating inside high magnetic fields, such as in simultaneous PET/MR scanners (33). The introduction of these multimodality imaging systems into clinical practice over the last years (34) has reaffirmed the importance of the response of PET photodetectors to magnetic fields. A comparison of the resulting output of a scintillator block detector (see section 2.3.4) in the presence of a magnetic field using PMTs and APDs is shown in figure 2.7, exemplifying also the size difference between both kinds of photodetectors.

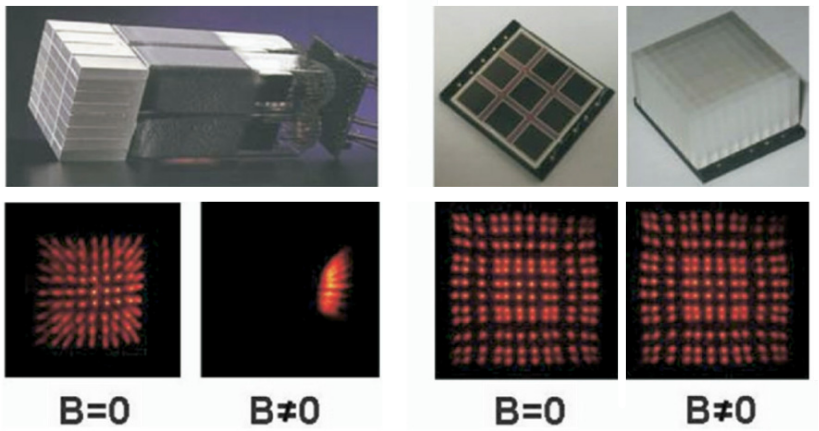

Figure 2.7: Response of a position-sensitive block detector with ($B \neq 0$) and without ($B = 0$) an applied magnetic field for a conventional PMT-based detector (left) and an APD-based detector (right). Image reproduced from (35).

A new variant of a semiconductor-based photodetectors have been recently

developed, the *Geiger-mode* APDs. Widely known as SiPMs (*silicon photomultipliers*), they are highly sensitive devices, able to measure single photons, insensitive to magnetic fields and with a gain factor comparable to that of PMTs (about 10^6). SiPMs are a matrix arrange of a large number of miniature APDs (*"micro-cells"*), connected in parallel to each other by a small integrated resistor and independently operating a few volts above breakdown voltage. A schematic representation of this basic structure and the operating principle is shown in figure 2.8.

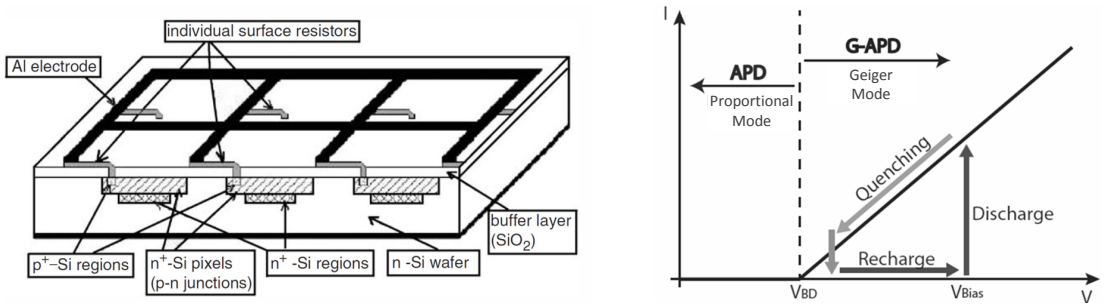

Figure 2.8: Basic structure (left) and operating principle (right) of a Geiger-mode APD (SiPM). Images reproduced from (36) and (37).

When biased, the depletion region of every micro-cell is in a metastable state until an electron or a hole destabilizes it, generating a self-sustainable avalanche breakdown. Thanks to the individual *quenching* resistor, when the current reaches an upper limit the bias voltage drops to the breakdown voltage and the multiplication process stops, avoiding the destruction of the cell. The SiPM starts then to recharge the cell until the voltage returns to the set bias. The dis- and recharge times are defined by the resistor and the capacitances of the structure. Each fired micro-cell produces a unit pulse of signal, independent of the photons absorbed in it during the avalanche process. The output signal of the SiPM is then the sum of all micro-cells that have been triggered by the impinging photons. For a lower number of simultaneously arriving photons, the SiPM signal is proportional to that number and, consequently, correlated to the energy deposited in the scintillator by the gamma-ray. For a high a photon flux though (comparable or larger than the number of cells), the signal is nonlinear and saturated, since more than one photon can be absorbed by each micro-cell during its discharge, but only the unit pulse is generated (38).

SiPMs have several properties that are relevant for their implementation in PET. One of the most important is the *photon detection efficiency* (PDE), which

relates the quantum efficiency to the geometrical design of the device by (39)(37):

$$PDE\left(\lambda, V_{Bias}, T\right) = QE\left(\lambda\right) \cdot P_a\left(\lambda, V_{Bias}, T\right) \cdot FF \tag{2.7}$$

where $QE(\lambda)$ is the quantum efficiency dependent on the photon wavelength, $P_a(\lambda, V_{Bias}, T)$ is the avalanche probability of the micro-cell (dependent on the photon wavelength, the applied bias and the temperature) and FF is the *fill factor*, which is the ratio of the sensitive area to the total surface of the SiPM. The PDE relates thus to the emission wavelength profile of the scintillator, where an as-good-as-possible match is needed to improve the light detection. Current commercially available SiPMs have a PDE of ca. 60% (40) at the peak wavelength of commonly used scintillators (see Table 2.2). Another relevant property is the *dark-count-rate* (DCR), which is the number of micro-cells that are triggered in absence of impinging photons. This is due to thermally generated electron-hole pairs and field-assisted generation of free charge-carriers that can start the avalanche process. DCR can be reduced by optimizing the production process minimizing the generation-recombination centers and by operating the device at lower temperatures and lower bias voltage (37). A lower bias voltage, however, reduces the PDE as well. Dark-count fired cells can not only disturb the value of the SiPM's output signal, but also reduce the number of effectively available cells for scintillation photons detection.

SiPMs can be manufactured as single devices of few millimeters size as well as matrix-like arrays, with micro-cell dimensions ranging from some tens to a few hundreds of micrometers. Thanks to their high gain, single photon measurement ability, fast signal output and insensitivity to magnetic fields, together with the development of cheaper mass-production procedures, SiPMs are already being applied in both clinical (41) and preclinical (42)(43) multimodal PET/MR systems and are likely to become the standard photodetector for PET applications.

All photodetectors here presented have in common the need of specifically designed external electronics to process the output signal in order to extract the information relevant for PET. A recently developed approach integrating both photodetectors and the processing electronics are the so called *digital silicon photomultipliers*. Their characteristics and functionality are thoroughly analyzed in chapter 3.

2.3.4 Detector Configurations

There are different possibilities to connect a scintillator to a photodetector in order to optimize the light detection for PET. Not only the optical interface between both plays an important role (similar refractive indexes to improve transmission over internal reflection; matching emission and detection wavelengths to improve efficiency), but also the geometrical arrangement between both elements is crucial. In the following, the three main different configurations are explained: large monolithic crystals being read by multiple photodetectors, block detectors with segmented crystals and a reduced number of photodetectors and, finally, one-to-one coupling of a small scintillator to one sensor (see figure 2.9). The three differ in the methodology to assess the position of energy deposition in the crystal by the gamma ray, with the common goal of determining the LOR (see section 2.2) assigned to a detected coincident event. A diagram of the three common configurations is shown in fig. 2.9:

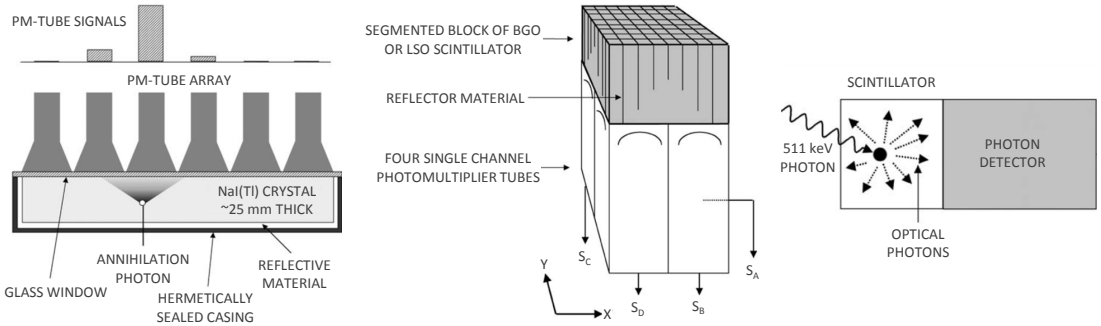

Figure 2.9: Schematic representation of the three most common configurations of scintillator and photodetector for PET systems: large monolithic crystals with multiple photodetectors (left), block detectors with segmented crystals and a reduced number of photodetectors (middle) and one-to-one coupling of a small scintillator to one sensor (right). Images reproduced from (27).

The first PET scanners were equipped with the best available scintillator at the time, NaI(Tl). Although very bright, the low stopping power at 511 keV (see section 2.3.2) demanded the utilization of large volumes of material to improve the system's sensitivity. A direct individual readout of a large crystal, however, implies a very low spatial accuracy of the LOR determination. This was solved by the use of the Anger detector (44), in which the light output of a large scintillator is read by an array of multiple PMTs through a light guide. A centroid positioning algorithm is used for estimation of the interaction position within the detector, by summing up the weighted signals of all the individuals PMTs and

normalizing it by the total signal detected. The weight used for each individual signal depends on the PMT's position within the array. The key to this algorithm is the light sharing of each scintillation event among all detectors, for which the light guide (usually glass) and, more important, a very high light-output is essential to achieve good spatial resolution. The resulting large detector of 30-50 cm size can be implemented in PET either rotating it around the imaged object or by a fixed ring arrangement of them. An example of this configuration is a clinical PET scanner built with 6 modules of curved NaI(Tl) plates with 48 PMTs each (45). Although being a simple and cost-effective design, the light spread over a large area results in significant detector dead time at high count rates.

The introduction of BGO and its high detection efficiency for 511 keV photons made the development of the so called "block detector" possible (46). In principle, it is a restricted version of the Anger concept with only 4 PMTs reading together the light spread of a crystal. The difference lies in the inner structure of the scintillator block, which is sectioned by partial saw cuts into discrete detector elements. A light reflector is placed in between every element and the depth of the cuts follows a scheme that changes the light pattern projected to the PMTs according to the element where the scintillation started. This allows then to assign the point where the gamma-ray deposited its energy to one of the crystal segments, as shown in figure 2.7 (section 2.3.3). Standard block detectors rely on the high detection efficiency of BGO to have usually 8×8 small segments of $4 \times 4 \times 30$ mm^3, effectively reducing the crystal size and improving so the spatial resolution. This detector design became the standard concept used in clinical PET systems, with newer systems using APDs and LSO instead of PMTs and BGO (47). Thanks to its reduced area and modularity it allowed the construction of scanners with multiple parallel rings of detectors. The restricted light spread and number of PMTs per unit over a smaller area results in a lower sensor dead time compared to the Anger concept. Nonetheless, the count-rate performance still represents the major drawback of this kind of PET detectors, as every module can only process one single event from one particular crystal segment at a time. This directly affects the clinical protocol by restricting the amount of radiotracer that can be injected to the patient.

The intuitive solution to overcome the count-rate problem is to couple one small scintillator to one photodetector. The spatial resolution achievable with this configuration is thus limited by the size of the crystal. One-to-one coupling was unpractical for a long time due to the large size of photomultiplier tubes, a limitation that disappeared initially with the development of position-sensitive

multichannel PMTs (48) and, more concretely, with the application of the small sized APDs (32) and SiPMs (49) (see section 2.3.3). The small volume of these semiconductor-based detectors makes them suitable for dense arrangements of large number of crystals in a detector ring. This results though in a very large number of individual signal channels to be processed, increasing the complexity and the cost of the full system. The latter is nowadays dominated more by the high production costs of a large quantity of small scintillators with homogenous high quality than by the photodetectors and the required electronics. The large number of individual channels and small discrete elements allow to achieve high counting rates, being thus less susceptible to dead time problems compared to larger area configurations. A characterization of two different scintillators coupled one-to-one to state-of-the-art digital SiPMs is presented in chapter 3.

Further configuration approaches have been realized, combining design characteristics of these three families and the advantages offered by the small-sized semiconductor-based photodetectors. One example is a modification of the block detector, with all crystal segments being equally long and adding at the front side of the scintillator an array of silicon photodiodes coupled one-to-one to every segment (50). The photodiodes recognize then which crystal element received the interaction and the PMTs measure the time and energy information of the scintillation pulse, while the ratio between the signals of both detectors provides information about the *depth-of-interaction* (DOI) (see section 2.4.4) of the gamma-ray inside the scintillator. Some groups are also working in miniaturized versions of the Anger concept using SiPMs for the readout, commonly known as "monolithic block". The area of the crystal is in the range of a few centimeters and is read out by an array of detectors. By means of different algorithms analyzing the measured light distribution it is possible to determine not only the 2D position of the energy deposition in the crystal but also its depth within the block (51)(52).

The decision on which detector configuration to apply is related to the final PET application and the goal performance of the system. Generally, full-body clinical scanners are based on the segmented-block detector and light spread approach, to reduce the number of channels and costs in large systems. On the other hand, one-to-one coupling of small scintillators is more commonly used in research and preclinical systems for small-animal imaging or, for example, dedicated human brain scanners, where an improved spatial resolution is needed and the overall costs are limited due to the smaller scale of the device.

2.4 Detector-Related Factors Affecting PET Image Resolution

2.4.1 System Sensitivity

Sensitivity is one of the most important characteristics of a PET scanner. It represents the fraction of annihilation gamma-rays emitted from the imaged object that are effectively detected and validated by the system. Hence, it influences the amount of radiotracer that needs to be delivered to the patient and the duration of the imaging procedure to obtain a quantitative and qualitative image. The scanner geometry defines the upper boundary of its sensitivity through the solid angle covered by the rings of detectors, with modern clinical PET scanners having about 25 cm axial coverage and ca. 70 cm diameter. Due to its isotropic emission, a large amount of gamma-rays escape this confined field of view and are thus lost. Moreover, those reaching the detector rings are not always measured, because of the detection efficiency of both the scintillator (see section 2.3.2) and the photodetector (2.3.3). Furthermore, once a coincidence event is detected, it still cannot be considered as valid. Besides true coincidences, also scattered, random and multiple coincidences can be measured, as shown in figure 2.10:

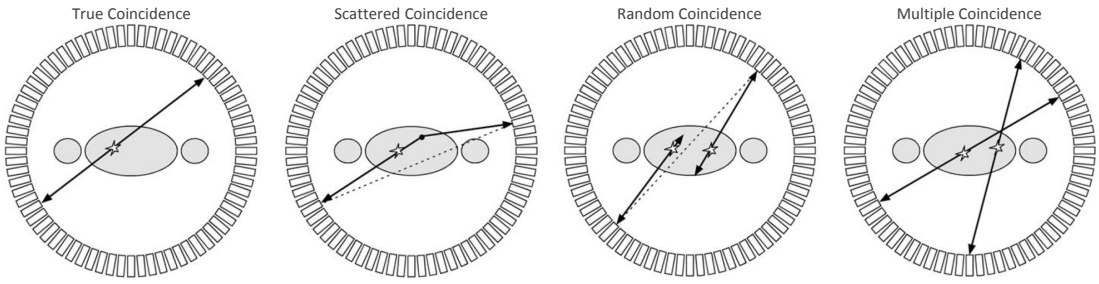

Figure 2.10: Different coincidences measured in a PET scanner. The dotted line shows the misaligned LORs for accepted scattered and random coincidences. Image reproduced from (27).

The decision about accepting or discarding these events is based first on the system's coincidence time window (to get rid of the randoms, see section 2.4.2), and energy resolution (to reject the scattered events, see section 2.4.3). Still, some scatter and accidental coincidences are accepted through these filters, yielding incorrect positional information and contributing with a relatively uniform background to the image that results in a loss of contrast (5). Multiple coincidences with three or more photons being simultaneously detected are normally directly

discarded.

2.4.2 Coincidence Time Resolution (CTR)

The *coincidence time resolution* (CTR, also commonly named *coincidence resolving time*, CRT) of a PET scanner describes the uncertainty in the timing characteristics of the scintillation detector on an event-by-event basis due to statistical fluctuations (4). The term *coincidence time* refers to the difference in time upon detection in opposite detectors of the two gamma-rays originating from the same annihilation event. Not only the size of the scanner influences this time difference (length of path traveled until detection), but also the detection process and the detector's intrinsic properties. These factors are:

Scintillator Size The length of the scintillator influences the acquisition time through the conversion depth of the gamma-ray as well as the transit time of the scintillation photons until being detected. Scintillation photons are emitted isotropically. Thus, those that flight directly towards the photodetector are detected earlier than those undergoing several internal reflections until reaching the sensor. If the energy deposition site is closer to the detector, a larger number of photons can promptly reach the photosensor.

Scintillation process Scintillation photons are emitted following a time distribution with a very fast initial stage and a much slower decay phase (see section 2.3.2). The detection time is therefore improved if the first emitted photons are also among the earlier detected ones.

Random photon loss Generated photons can be optically absorbed in the crystal itself or in the boundary to the photodetector. Additionally, not every photon reaching the sensor is detected due to photodetection efficiency. The influence on time resolution is higher if the *faster* photons are lost.

Photodetector response The photodetector has an intrinsic time response for the detection of a single photon, known as *single photon time resolution* (SPTR). A faster sensor improves thus the total detection time.

Signal conversion The electronics in charge of extracting the time information out of the generated electric pulse have an intrinsic delay that also influences the resulting CTR.

Noise Unwanted signals introduced by the photodetectors and the readout electronics can alter the time measurement.

A coincidence time window usually twice as long as the CTR of the system is fixed for the data acquisition. If two single high-energy photons are detected within this window, then they are accepted as a coincidence event, assuming both were generated together at the annihilation point. However, it is possible that two unrelated single gamma-rays are accidentally recorded during the coincidence window. The resulting *random coincidence* cannot be distinguished from a true coincidence, creating an incorrect LOR that is not related to an annihilation site (see figure 2.10). As a consequence, the added uncorrelated background decreases the contrast of the PET image. A narrow coincidence window helps to reduce the detection rate of randoms, at the cost of losing true events being detected in opposite extremes of the field of view, which is more relevant in large systems allowing coincidences between multiple detector rings (3D PET). Detectors with good timing resolution are thus essential to decrease the number of random coincidences and thereby reduce the image background.[1]

CTR is also crucial for systems where *time-of-flight* (TOF) acquisition is implemented. In TOF-PET, every measured time difference upon detection is used to estimate the position of the corresponding annihilation point along the LOR. Since gamma-rays travel at the speed of light, it is currently technically impossible to exactly determine their origin based solely on their time difference (100 ps correspond to 1.5 cm). Therefore, a probability distribution based on the measured time difference is included along the LOR, to assign the region where the annihilation most likely happened. In non-TOF systems, the annihilation point is assumed to have an equally distributed probability of occurrence over the full LOR, as depicted in figure 2.11:

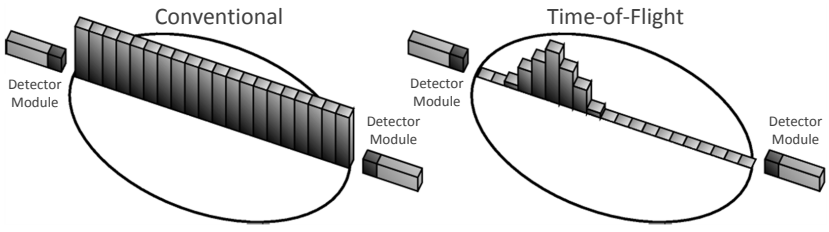

Figure 2.11: Probability of localization of the annihilation site along the LOR without TOF (left) and with TOF (right). Image reproduced from (53).

For TOF-PET, an extreme good CTR in the range of hundreds of picoseconds is needed (54), with the timing properties of the scintillator playing a relevant role.

[1]Random correction techniques can be applied to the measured data. An introduction to them can be found, among others, in (4) or (5).

Clinical TOF scanners equipped with LSO or LYSO scintillators have a system CTR around 600 ps (55)(56)(57). Improvements in timing resolution by means of faster scintillators ($LaBr_3$) or enhanced readout electronics (digital SiPMs) have resulted in systems reaching CTR values of 375 ps (29) and 350 ps (58) respectively. Performance analyses based on the clinical applications of TOF-PET systems have shown that some of the main benefits of this technique are (59):

- Better contrast and lower noise (i.e., higher *signal-to-noise* (SNR) ratio).
- Higher SNR gain for patients with higher BMI.
- Faster convergence of iterative reconstruction methods.
- Larger impact on lesions located in the abdomen and thorax than those in head and neck.
- Reduction of image artifacts, impacting the diagnosis due to improved image quality.
- Better definition of small lesions and image details.

The improvement in CTR is a very active field of research. Measurements with two single detectors in coincidence have already achieved CTR values below 100 ps in an optimized setup using small fast scintillators (60). Similar experiments with standard PET-suited scintillators are commonly below 200 ps (see chapter 3), a goal resolution being currently aimed by projects developing full systems for multimodal clinical imaging procedures (61).

2.4.3 Energy Resolution

As explained in section 2.3.1, high-energy photons interact with matter depositing either partially (Compton scatter) or completely (photoelectric effect) its energy. During a PET examination, the annihilation-created 511 keV gamma-rays can exit the imaged object with its full energy or with part of it after being scattered. As they interact with the detectors, they may undergo one or more Compton scatter and then exit the detector (i.e., depositing only a portion of their energy), or deposit its full energy through multiple scatters or direct photoelectric interaction. The combination of these possible scenarios leads to large variations in the energies registered by the detector, which histogrammed for all detected events result in an energy spectrum with a characteristic two-region shape (see figure 2.12).

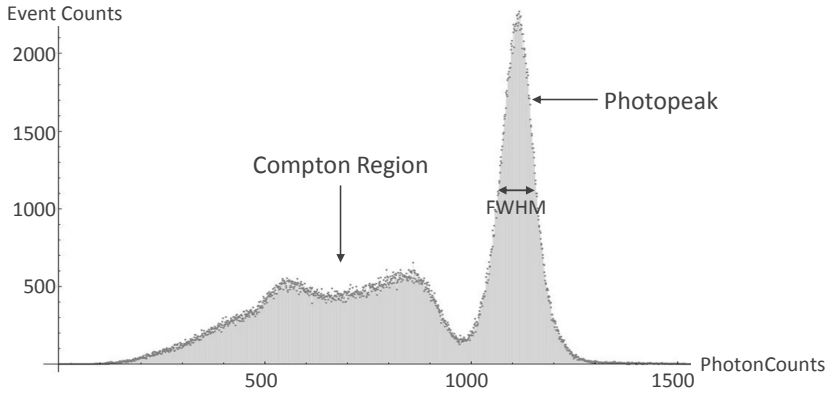

Figure 2.12: Energy spectrum of ^{18}F measured with a 2x2x8 mm^3 LYSO scintillator optically coupled one-to-one to a digital SiPM. For this setup, the Compton region corresponds to events with less than approximately 1000 photon counts.

The region on the left of figure 2.12 represents all registered events with incomplete deposition of energy (Compton region), while the region on the right represents those with full energy deposition. The peak of this region, known as *photopeak*, corresponds to the energy of the incident radiation, being 511 keV for PET radiotracers. The fluctuations around this peak are mostly due to the statistical variations during the conversion process of the gamma-ray into scintillation photons an then into a measurable electric signal. The width of the photopeak characterizes thus the accuracy of the detector to measure the deposited energy and is defined as the *energy resolution* of it. It is generally measured as the *full width at half maximum* (FWHM) of the photopeak's amplitude and usually given as a percent of the energy to be detected (511 keV). Consequently, a higher energy resolution value denotes a less accurate detector.

This ability to distinguish between different energies is highly relevant for PET. During an examination, a high number of 511 keV photons undergo Compton scatter within the human body, a number that increases in larger-sized patients due to the bigger cross-section being traversed by the gamma-ray. They reach then the detectors with reduced energy through a deflected path. The scattered event is detected within the coincidence time window (see section 2.4.2) and is so associated to a LOR that doesn't comprise the annihilation site. To filter out these coincidences, an acceptance energy window around the photopeak can be applied, with its width determined by the energy resolution. The better this characteristic of the detector, the narrower the energy window can be, increasing the rejection of scattered events. However, if the energy measured by one detector

is lower than 511 keV, it is not possible to discriminate whether the gamma-ray had previously been scattered in the imaged object or it only partially deposited its energy in the crystal. For this reason, the energy acceptance threshold cannot be set too high, to avoid reducing sensitivity by discarding events that are indeed valid. The consequent acceptance of small-angle scattered gamma-rays contributes to image degradation through misalignment of LORs, adding background counts that result in worsen contrast.

The energy acceptance of clinical PET scanners varies according to the detectors being used. For example, the good energy resolution of NaI(Tl)-based detectors allows an energy-cut at ca. 450 keV, corresponding to a single-scattered angle of about 30°. For BGO-based systems instead, a lower threshold between 300 - 400 keV is implemented, which translates into approximately 70° of maximum deviation (4). To compensate for the introduced image contrast loss, scatter correction techniques are applied to the measured data.[1]

2.4.4 Depth of Interaction (DOI)

Every coincidence event detected in PET is assigned to the LOR connecting the two involved detectors. As seen in section 2.2, a large number of measured LORs is needed to reconstruct the image. The correctness of the reconstruction relies on the truthful relation between the involved LORs and the activity distribution being imaged. The *depth-of-interaction* (DOI) of the gamma-ray in the scintillator, i.e. the point of energy deposition within the crystal, is not determined in conventional clinical PET scanners. Based on this, the line-of-response between two detectors is usually projected to connect both front faces. However, gamma-rays can enter the scintillators also through its sides and interact in any position inside the crystal volume. As a consequence, the real line of interaction lies within a three dimensional "tube-of-response" representing all possible lines connecting the two involved detectors. This phenomenon, known as *parallax effect*, is depicted in figure 2.13. The gray areas indicate all possible interactions between two detectors, the segmented arrows give an example of a possible coincidence and the dotted line shows the LOR assigned to that event. The detectors located in the outer regions of the field of view have an increased obliqueness relative to each other, broadening the uncertainty between the assigned LOR and the true path of the gamma-ray. The LOR-based reconstruction algorithm cannot account for

[1] The detail of scatter correction techniques are out of the scope of this work. An introduction to them can be found, among others, in (4) or (5).

this uncertainty, leading to a blurred image.

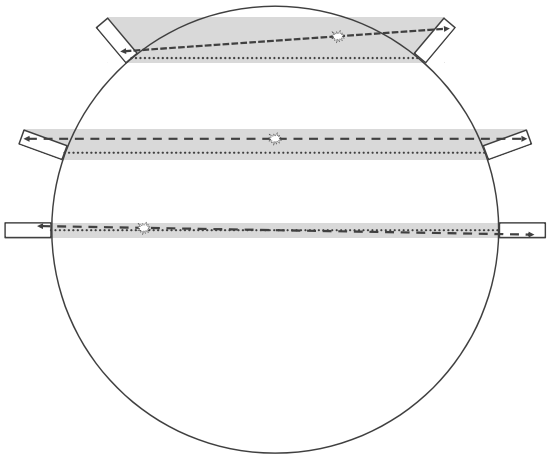

Figure 2.13: Parallax effect introduced by annihilation events being detected in the outer regions of the field of view. The difference between the assigned LOR (dotted line) and the true photon path (segmented arrow) increases at larger radial distances.

The size of the detectors influences the achievable spatial resolution by defining the accuracy of the LOR. As shown in figure 2.13, this precision decreases for events being detected at increased radial distances from the center of the scanner. The parallax effect is therefore strongly dependent on the scanner's and detector's geometry and has a greater impact on systems with small diameters (62), for example for small-animal imaging or dedicated brain scanners. The direct solution to reduce this error and improve spatial resolution is the implementation of small scintillators. This approach is limited though by the loss in system sensitivity due to the reduced stopping power for high-energy photons with smaller crystal volume. Some systems mitigate the parallax effect assuming a constant DOI equal to the mean distance travelled by a 511 keV gama-ray in the scintillator material. Further strategies exist for a more accurate DOI determination, combining different detector configurations and offline analysis of the acquired signals. The following list summarizes the most relevant among them:

Phoswich This technique involves the optical coupling on top of each other of two or more kinds of scintillators with significantly different decay times. An analysis of the acquired signal based on pulse shape discrimination allows to recognize which of the crystals interacted with the high-energy photon (63). The DOI accuracy is limited to the size of each crystal layer.

Dual radial detector layer This approach consists in two concentric rings of detectors, with one-to-one coupling of scintillators and photodetectors (64). Each radial layer comprises smaller scintillators compared to the standard one-ring structure, with the total volume of crystal assuring a high detection efficiency. The use of small photodetectors (APDs or SiPMs) allows a dense arrangement of detectors, avoiding non-sensitive gaps in the structure. The individual readout limits the DOI capability to the size of each scintillator and the recognition of the internal or external ring.

Double-sided crystal readout This method is based on the use of photodetectors at both ends of a long scintillator. The photodetector closer to the energy deposition detects a larger number of scintillation photons, allowing the DOI to be obtained by the ratio of the two simultaneously detected signals. Different approaches consider combining semiconductor-based photodiodes on one extreme and photomultiplier tubes on the other (65) or both readouts by means of APDs (66), achieving a DOI resolution of 5 - 8 mm and 4 - 6.5 mm respectively.

Layered Arrays This technique is based on stacking multiple layers of matrix-arranged segments of scintillators, with reflectors inserted between the individual elements. By changing the crystal overlap and reflector pattern between layers, the light spread projected to an array of photodetectors creates a *flood map*, allowing individual recognition of each small scintillator (67). An expansion of this concept including photodetector arrays on every face of the scintillator block allows a more accurate recognition of every crystal segment (68). The DOI resolution of a few millimeters is limited for both approaches to the minimum clearly recognizable crystal size.

Light spread from monolithic crystals This approach relies on the readout of a monolithic scintillator by means of an array of photodetectors. The detected light distribution changes according to the position of the energy deposition in the crystal volume. For a scintillator volume of 12x12x10 mm^3 a three dimensional DOI accuracy of less than 1 mm is achieved (52), increasing to 1 - 4.5 mm for a larger crystal of 20x20x12 mm^3 (51).

The application of these different techniques is so far limited to research systems, with no DOI-capable PET system being currently used in clinical practice. A new detection concept of gamma-rays for PET with three-dimensional DOI ability is introduced and analyzed in chapter 4.

3

Characterization of Digital SiPMs for PET with LYSO and GAGG Scintillators[1]

3.1 Introduction to digital SiPMs

As introduced in section 2.3, silicon photomultipliers (SiPMs) represent an alternative to photomultiplier tubes (PMTs) in both clinical (41) and preclinical (42)(43) positron emission tomography (PET) scanners, thanks to properties like compactness, insensitivity to magnetic fields, high signal gain and high photodetection efficiency (PDE) (39). For their implementation in a PET system, the analog signal generated by these sensors needs to be further processed in application specific electronics to obtain the necessary information regarding energy and time of each acquired event. Recently, a device has been developed by Philips Digital Photon Counting, which combines SiPMs with electronics integrated on cell level to deliver a fully digital signal, providing the detected photon counts per pixel and their time stamp (69)(70). The so-called DPC (Digital Photon Counter) consists of a tile with an 8x8 matrix of pixels, covered by a thin glass plate. The acquisition of events and data processing is performed separately on subgroups (dies) of 4 pixels each (71). The DPC offers functions that the traditional analog SiPMs don't, such as the possibility to deactivate individual cells to reduce the dark-count-rate, enable only a custom-defined area of the sensor or measure

[1]The content of this chapter is based on the publication "Performance Analysis of Digital Silicon Photomultipliers for PET", submitted to the scientific journal *Journal of Instrumentation* (JINST) in February 2015 and currently under review. See Appendix D.

the impinging photons on slave pixels being triggered by a light-intensity-defined master pixel. Figure 3.1 shows the difference between the analog and digital approach.

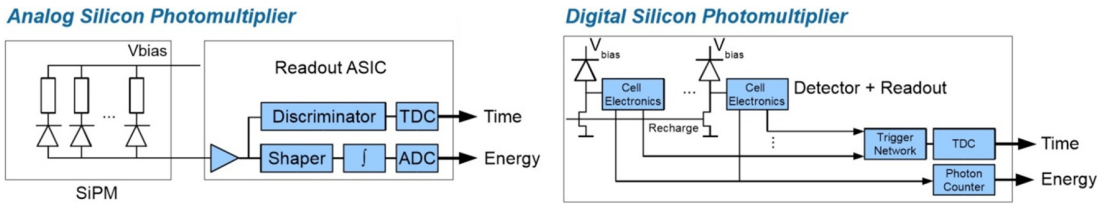

Figure 3.1: Representation of the different acquisition concepts and readout approach between analog (left) and digital (right) SiPMs. Image reproduced from (70).

The functionality of this novel sensor architecture and detection concept has been analyzed for its implementation in different applications. In (72) and (73), probabilistic and statistical models have been developed and validated to evaluate the impact of the number of detected photons in the sensor's performance. This impact is defined by the different possible configurations of the device, which need to be adjusted for the specific application. Among them, PET has been the most studied one. Different groups have analyzed the results in terms of energy, time and spatial resolution as well as depth-of-interaction when coupling single scintillators (74), crystal arrays (75)(76) or monolithic blocks (77)(78). Based on these different approaches, the first prototypes of stand-alone preclinical PET systems have been developed, achieving 266 ps (FWHM) system coincidence timing resolution by means of one-to-one coupling of $4\times4\times22$ mm^3 LYSO crystals (79) and 0.7 mm spatial resolution with a thin monolythic LYSO scintillator of $32 \times 32 \times 2$ mm^3 (80). The device is also being used to construct a fully digital PET/MR insert (81), while its manufacturer is using the DPC to equip the first clinical PET/CT scanner based only on digital SiPMs (58). The sensor's performance has also been analyzed for its implementation in other applications, such as single photon emission computed tomography (SPECT) (82)(83), the development of a compton camera for environmental radiation surveillance (84) and the detection of Cherenkov photons in a high-energy-physics experiment (85). In parallel, new approaches of digital SiPMs for PET based on different soft- and hardware architectures are being developed by several groups (86)(87)(88), forecasting further improvements of this technology in the upcoming years.

Due to the DPC's combination of intrinsic properties of analog SiPMs together with a specifically developed acquisition protocol, several operational parameters

can be adjusted. In the following sections, the combination of five different parameters and its impact on both the intrinsic as well as the PET-oriented sensor's performance is experimentally analyzed when coupled to two different scintillator candidates. The scope is to define the best possible operational configuration for a potential implementation in a PET system in terms of energy resolution, coincidence time resolution and detection sensitivity.

3.2 Experimental Setup and Methods

3.2.1 System Setup

One tile of the analyzed model, DPC-3200-22_C, consists of 4×4 dies, each of them grouping 2×2 pixels. One pixel has an area of 3.2×3.8775 mm^2 and contains 3200 cells. Cell area is 59.4×64 μm^2 and the pixel fill factor is 74%, with the peak of light sensitivity at 420 nm (89). Typical breakdown voltage is about 23.5 V with a specified operating bias range up to 3.5 V overvoltage. Each die has one pair of TDCs that generates a common time stamp for its 4 pixels. Once the number of detected photons reaches a configurable trigger threshold, the time stamp is registered and a validation process to discard dark-count-generated events is started. Both trigger and validation levels are defined based on specific distributions of discharged cells over the four quadrants of a pixel (sub-pixels) (71). If the event is successfully validated, it is followed by an integration period to determine the total number of detected photons. The acquisition sequence ends with the readout process and the recharge of the cells. During the full sequence, each cell is able to fire only once. For each detected and validated event, the resulting information is the photon counts for all pixels in a die and their common time stamp registered at the trigger. The schematic diagram in figure 3.2 shows the event acquisition chain.

The sensor's performance is also determined by the operating voltage, temperature and cell inhibition. The latter is a property of the DPCs, in which individual cells with high dark-count-rate (DCR) can be disabled to reduce the sensor's overall noise. Every cell's intrinsic dark-count-rate is measured by means of an incorporated function registering the firing frequency of each single cell in absence of impinging photons. The applied cell inhibition is based on the resulting dark-count map and defined as a percent of the cells with higher DCR per die.

Two opposing tiles are placed at 88 mm distance on a Peltier-based cooling

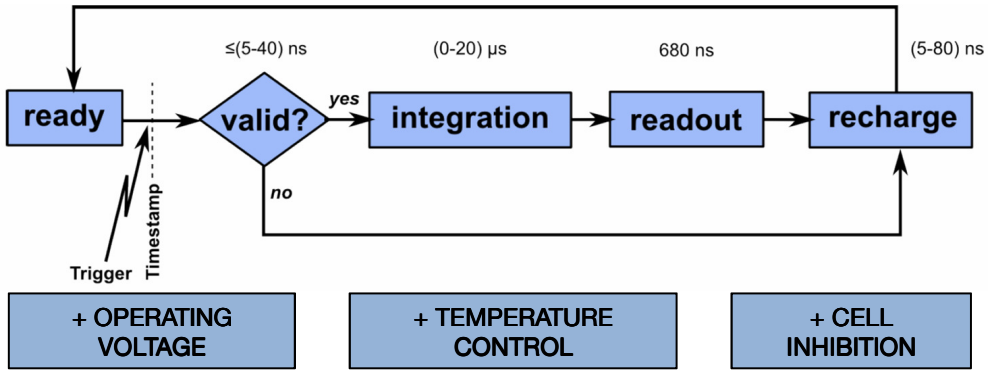

Figure 3.2: Diagram of the DPC's acquisition sequence (71) and operational parameters.

system. The heat dissipated by the Peltier elements is removed by a chiller-cooled water circuit. The operating temperature is measured by the sensor incorporated in each tile. To avoid condensation of air humidity at lower temperatures, the system is placed in a sealed housing from which air is flushed out with dry nitrogen gas. The complete setup, shown in figure 3.3, is placed in a light tight box.

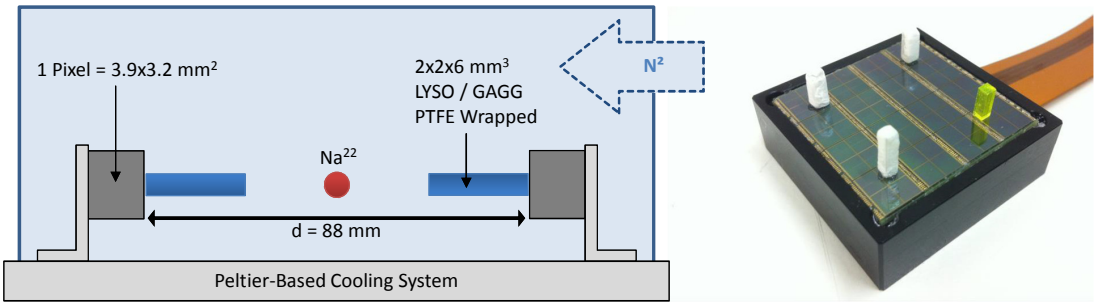

Figure 3.3: Schematic of the experimental setup showing the implemented cooling system (left). The image on the right shows an example of one DPC tile with different scintillators, with and without wrapping, and coupled to different pixels.

For measuring scintillation light, pairs of Teflon-wrapped LYSO (90) and GAGG (91) crystals were optically coupled with Dow Corning 1.2577 silicone (92) to the center of one pixel in each tile. Size of each crystal is $2 \times 2 \times 6$ mm^3. Only the pixel with the crystal coupled was enabled during the measurement. GAGG (gadolinium aluminum gallium garnet, Z_{eff}=54, 6.63 g/ccm, 4.5% energy res. FWHM@662 keV, 520 nm, 60000 ph/MeV, 88 ns (92%) and 230 ns (8%) decay times, non-hygroscopic, chemically and mechanically stable (30)) is a new scintillator that is being used in combination with these dSiPMs to set up a PET

prototype (93). Both for singles and coincidences acquisitions, a 1.7 MBq point source of ^{22}Na was placed centered and equidistant between a pair of crystals. The operational parameters analyzed were varied as shown in table 3.1. For all measurements, validation length was 10 ns and integration length 85 ns, with the sum of both resulting in a total counting time that comprises the decay time of both scintillators. The time duration of each complete measurement is defined in number of TDC frames, with 1 frame being 327.68 μs and a TDC bin size of 19.5 ps (71).

Parameter	**Values (standard)**
Trigger Scheme	1, 2, 3, 4 (1)
Validation Scheme	1, 2, 4, 8 (4)
Cell Inhibition [%]	0 - 85 (10)
Tile Temperature [°C]	-9.0 - 28.0 (5.6)
Overvoltage [V]	1.0 - 3.5 (3.0)

Table 3.1: Values and range of operational parameters analyzed. The number and spatial distribution of detected photons related to each scheme (trigger and validation) can be found in (71). The standard applied configuration is shown in parenthesis.

The trigger and validation schemes don't represent a number of detected photons, but a logic connection between sub-structures of the pixel. For the triggering decision, the configured scheme represents a spatial distribution of detected photons over the 4 sub-pixels conforming one pixel. As an example, trigger scheme 1 requires only photon to be detected in any region of the pixel, while the scheme 4 demands at least one photon to be detected in every sub-pixel. For the validation, the decision is made base on the photons detected on groups of cell rows in a sub-pixel. The elected scheme represents a logic connection (validation pattern) between these group of rows as well as between the sub-pixels (71). Figure 3.4 depicts the sub-pixel structure and shows the statistically calculated number of photons needed to reach the trigger and validation thresholds, according to the chosen scheme and assuming an homogenous light distribution over the whole pixel.

The two tiles are connected to a base unit provided by the manufacturer, which sends the data stream to the processing computer via USB, where an open-source (GPL) software provided by Philips acquires the measurement data. The DPC output (ASCII list-mode) is then analyzed using custom written C++

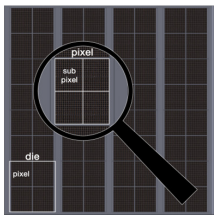

Trigger scheme	Logic connection	Avg. number of photons to trigger
1	sp1 ∨ sp2 ∨ sp3 ∨ sp4	1
2	[(sp1 ∨ sp2) ∧ (sp3 ∨ sp4)] ∨ [(sp1 ∨ sp4) ∧ (sp2 ∨ sp3)]	2.333
3	(sp1 ∨ sp2) ∧ (sp3 ∨ sp4)	3.0
4	sp1 ∧ sp2 ∧ sp3 ∧ sp4	8.333

Validation scheme	Validation pattern	Avg. number of photons to validate	Min. number of photons to validate
1	0x7F:OR	1	1
2	0x77:OR	4.6 (± 2.1)	2
4	0x55:OR	16.9 (± 6.2)	4
8	0x00:OR	52.2 (± 15)	11

Figure 3.4: Representation of the sub-pixel structure of the DPC sensor (left). The tables in the middle and in the right give the statistically calculated number of photons needed to reach the trigger and validation thresholds for the analyzed DPC model, assuming an homogenous light distribution over the whole pixel. Tables reproduced from (71).

and ROOT (94) programs.

3.2.2 Saturation Correction

Due to the brightness of the scintillators used (about 30 - 60 thousand ph/MeV for LYSO and GAGG, respectively) and the limited number of cells in a DPC pixel, the detector's response is not linear with the number of impinging photons. This phenomenon is further increased by the active cell recharge only at the end of an acquisition sequence. To correct the acquired data, the following equation is used based on the number of cells fired N_{fired}(95):

$$N_{fired} = N_{total} \cdot \left(\frac{t_{sc}}{t_d}\right) \cdot \left(1 - e^{\left(\frac{-N_{photon} \cdot PDE}{N_{total} \cdot \left(\frac{t_{sc}}{t_d}\right)}\right)}\right), \quad t_{sc} > t_d \tag{3.1}$$

where N_{total} is the total number of cells in the pixel, N_{photon} is the number of incident photons, PDE is the photon detection efficiency, $N_{photon} \cdot PDE$ is the number of detected photons, t_{sc} is the scintillator's decay time and t_d the cell dead time during its recharge. For the particular case of the DPC, N_{total} represents the total number of cells available considering cell inhibition ($N_{total} = N_{max}$) and, since cells are able to fire only once, the factor t_{sc}/t_d is assumed to be equal 1. With this, N_{fired} represents the output information of the DPC, N_{ph}^{data}. As proposed in (96), taking the first order Taylor expansion of equation 3.1 as an estimate of the linear response and solving it for the number of detected photons, the equation to obtain the saturation corrected number of photons N_{ph}^{corr} is:

$$N_{ph}^{corr} = -N_{max} \cdot \ln\left(1 - \frac{N_{ph}^{data}}{N_{max}}\right) \tag{3.2}$$

Equation nr. 3.2 corresponds to the one provided by the manufacturer (69)(71). However, N_{max} can't be accurately determined a priori in this study, since the used scintillators cover approximately one third of the pixel's active area. The glass plate covering the sensor's surface introduces light spread to neigbhoring cells, i.e. photons can be detected by more cells than only those directly under the front face of the scintillator. Therefore, an approximation of N_{max} is obtained from each measured energy spectrum as the maximum count of discharged cells, taking thus the configured cell inhibition into account.

3.3 Experimental Results

In the following, sensor performance results are shown for different configurations of the operational parameters shown in table 3.1. Unless stated otherwise, the standard applied configuration was trigger scheme 1, validation scheme 4, 10% cell inhibition, tile temperature 5.6°C and overvoltage 3.0 V.

3.3.1 Temperature Behavior

The temperature of the digital silicon photomultiplier increases after starting data acquisition, e.g. due to the FPGA on the backside of each tile. As explained in section 2.3.3, the performance of semiconductor-based photosensors is affected by changes in temperature. Among others, relevant properties such as the photodetection efficiency (PDE) and the dark-count-rate (DCR) are temperature-dependent. It is therefore necessary to operate the sensor under stable temperature conditions.

The temperature behavior was measured with activated data acquisition for 5 minutes for 12 different initial temperatures between 1°C and 28°C. With the implemented cooling system, temperature rises rapidly in the first 30 seconds and stabilizes after approx. 3 minutes, with a mean increase of 4.47 ± 0.3°C for tile 1 and 3.6 ± 0.2°C for tile 2 (see figure 3.5). The dependency of the breakdown voltage (V_{BD}) versus temperature was measured in the same temperature range. The resulting temperature variation of V_{BD} is about 20 mV/K for both tiles (see figure 3.6), corresponding to the value given by Philips (71).

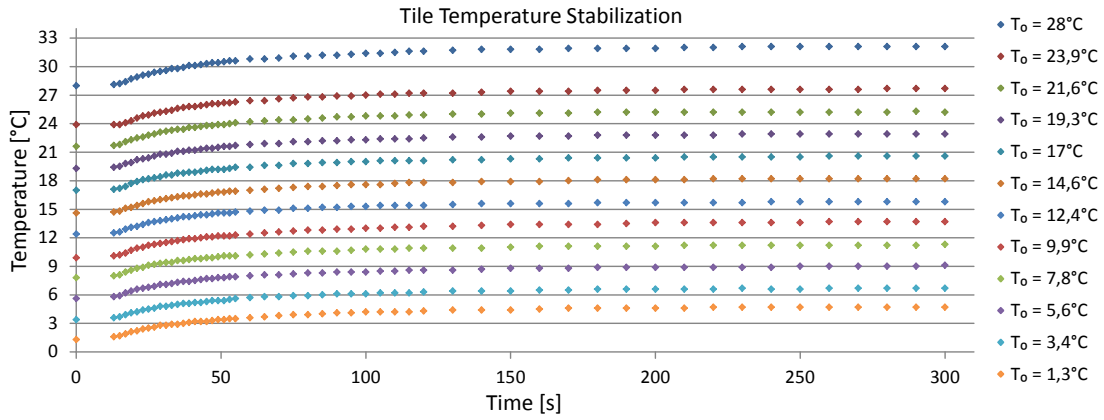

Figure 3.5: Tile temperature versus measurement time at different initial temperatures for tile 2.

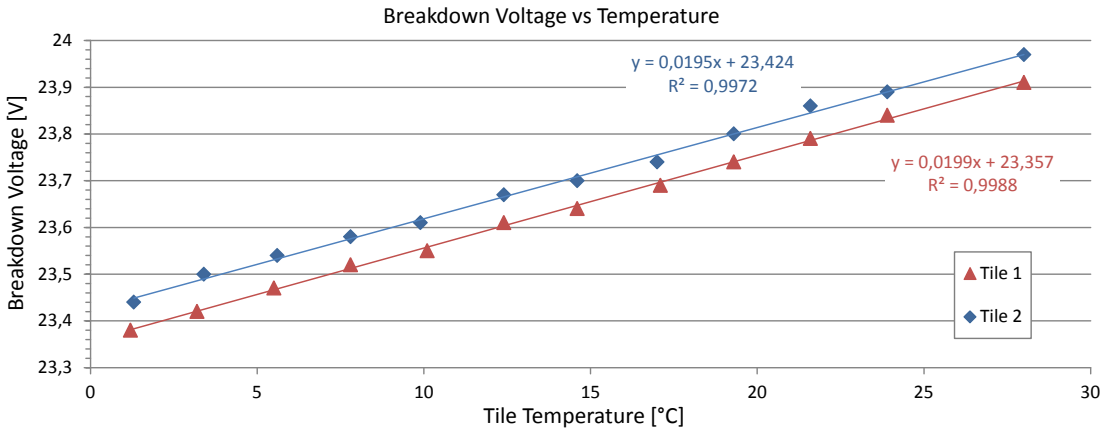

Figure 3.6: Breakdown voltage (V_{BD}) versus temperature. Temperature variation of V_{BD} is 20 mV/K for both tiles.

3.3.2 Optical Crosstalk

As introduced in section 2.3.3, when a photon is detected in the depletion region of a SiPM cell it triggers an avalanche of carriers. During this avalanche breakdown, an average of 3 optical photons are emitted per every 10^5 generated carriers (97). These photons can travel to a neighboring cell and trigger themselves another avalanche, similar to an external incoming photon. This phenomenon, known as *optical crosstalk*, is dependent on the applied operating voltage and can alter the relation between the SiPM output signal and the detected scintillation pulse. A lower crosstalk probability is thus required for an optimal photosensor performance.

The crosstalk probability can be experimentally extracted from a dark-count generated single-photon spectrum and defined as:

$$P_{Crosstalk}[\%] = \frac{counts > 1\ photon - count}{number\ of\ total\ photon - counts} \tag{3.3}$$

To obtain these single-photon values with the DPC, it is necessary to by-pass the previously described acquisition sequence. This was achieved by measuring in one slave pixel being triggered randomly by a master pixel located in opposite corners of the tile by means of the sensor's *neighbor logic* (71). The master pixel is coupled to a scintillator, while the slave pixel is left empty. When the master starts a validated acquisition sequence, the slave starts the acquisition as well, skipping the trigger and validation steps (see figure 3.2) and measuring only dark-counts. The total photon counting time to measure the single-photon spectrum is 40 ns and the dark-count-rate of the slave pixel is 153 kHz/mm^2 at 3.7°C with 100% active cells. Figure 3.7 shows the acquired dark-count-based single-photon spectrum and the resulting crosstalk probability calculated using equation 3.3. Within the restricted range of overvoltage allowed for the operation of the DPC, crosstalk behaves linearly with increasing bias (31). Above the initial linear range though, results obtained with analog SiPMs show an exponential growth of crosstalk at higher overvoltages (98).

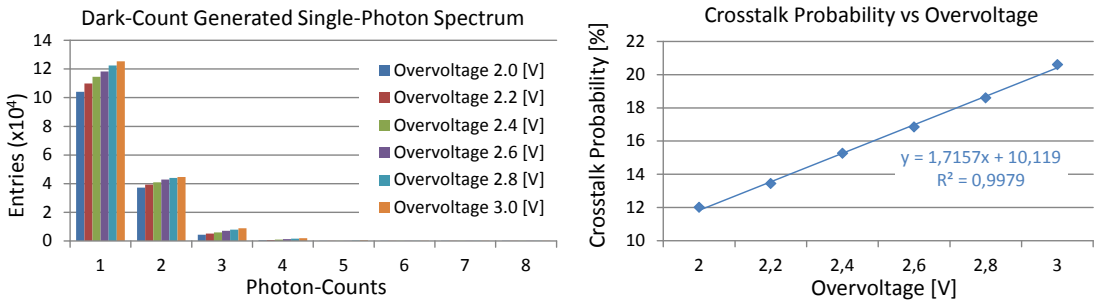

Figure 3.7: Optical crosstalk measured through a dark-count based single-photon spectrum (left). The calculated crosstalk probability (right) shows the expected initial linear behavior within the restricted DPC's overvoltage range (31)(98).

3.3.3 Dark-Count-Rate

The dark-count-rate (DCR) is an intrinsic property of a silicon photomultiplier (see section 2.3.3). The DPC device allows to measure the DCR by means of the so called dark-count maps. To obtain them, the sensor is activated in absence of

impinging photons (i.e., dark environment and no scintillators coupled). It then measures, for every cell, the number of self-triggered avalanches over a fixed period of time. The presented DCR results were measured thorugh dark-count maps at different temperatures and applied bias voltages for a length of 100 frames per cell. The impact of cell inhibition on DCR is calculated offline and included in the results as a third parameter. Due to the exponential increase of DCR, working at temperatures slightly below 0°C with 20% cell inhibition reduces the mean DCR per tile by almost 2 orders of magnitude compared to room temperature and 100% of active cells (see figure 3.8).

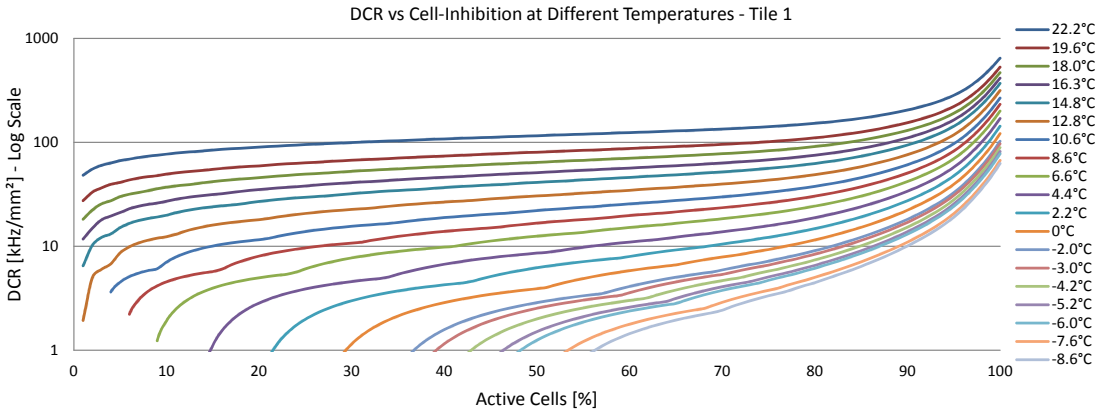

Figure 3.8: Mean DCR of tile 1 vs active cells at different temperatures. DCR (kHz/mm^2) at 10% cell inhibition is 204, 22 and 10 at 22.2°C, 0°C and -8.6°C respectively.

The values shown in figure 3.8 are averaged over the whole tile (64 pixels). Within a tile though, DCR varies among all pixels, as seen in figure 3.9.

The relative variation between pixels shows the same pattern at different percentages of cell inhibition. This characteristic remains unaltered for all the tile temperatures analyzed. Since DCR is related to the manufacturing process of the silicon-based sensor, the differences between pixels are most likely caused by impurities introduced in the semiconductor wafer during production.

The influence of bias voltage in DCR was measured for overvoltages between 1.0 V and 3.4 V, showing a similar behavior than that shown against temperature in figure 3.8 (plot in appendix A, figure A.1). The pattern among same-tile pixels shown in figure 3.9 is also not changed by modifications of the operating voltage. A summary of DCR values at 0% and 10% cell inhibition for different overvoltages and temperatures is presented in table 3.2.

The effect of the operating voltage on DCR can be seen in figure 3.10. The

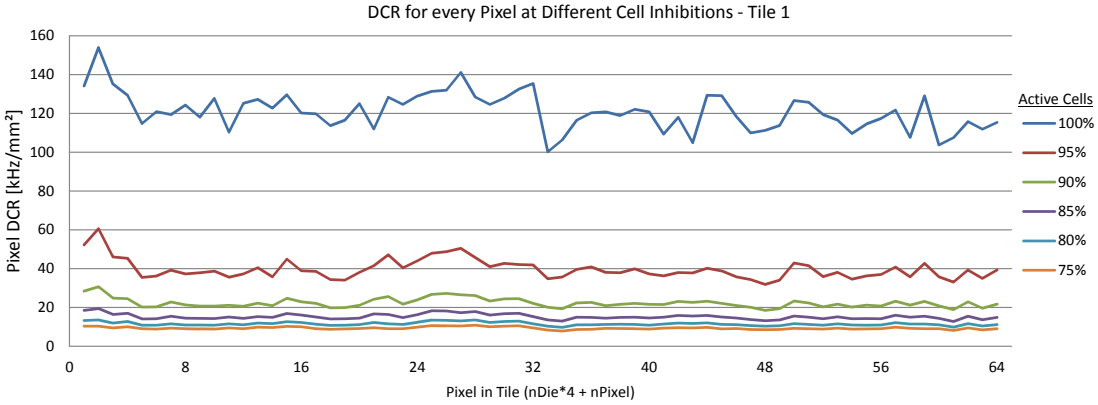

Figure 3.9: DCR variation among all pixels of one tile at different cell inhibition percentages.

		Tile Temperature [°C]			
Overvoltage [V]	Cell Inhibition [%]	5	10	15	20
2.4	0	135	201	260	445
	10	27	45	64	135
3.0	0	172	244	375	495
	10	35	54	96	141
3.4	0	195	284	365	631
	10	39	64	88	187

Table 3.2: Mean DCR values for tile 1 at different overvoltages, temperatures and cell inhibitions. DCR values are in kHz/mm^2 and rounded to the unit.

graphic on the left shows that, for a fixed temperature (in the figure, 5°C) and different percentages of active cells (in the figure, from 70 to 100%), the mean DCR increases linearly with overvoltage within 1.0 V and 3.4 V. The slope of each linear trend represents thus the *DCR coefficient per voltage*, i.e. the rate of change of DCR with overvoltage at a constant temperature and cell inhibition. The result of repeating the same linear trend analysis at 10, 15 and 20°C is shown in the right graphic of figure 3.10.

The DCR variation per volt is relevant (e.g., 60 kHz/(mm^{2}V) at room temperature and 10% cell inibition), especially at higher percentages of active cells. Nonetheless, due to the limited applicable range of bias voltage to operate the DPC sensor, DCR can be more effectively minimized by means of temperature reduction than lower overvoltages.

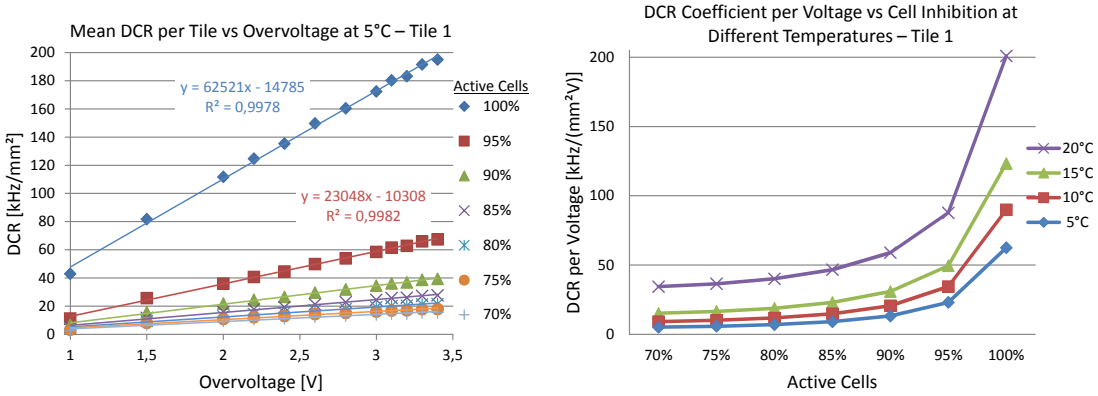

Figure 3.10: Left: Linear increase of DCR with overvoltage at constant 5°C and different cell inhibitions (10°C, 15°C and 20°C in appendix A.2). The slope of each linear trend corresponds to the DCR coefficient per voltage. For better visualization, only two linear trend parameters are shown. Right: behavior of the DCR coefficient per voltage at different cell inhibitions and temperature configurations.

3.3.4 Energy Resolution

Energy spectra with ^{22}Na have been acquired both as singles and coincidences, combining all the operational parameters shown in table 3.1. All given energy resolution values are the full width at half maximum (FWHM) of a single Gaussian fit to the 511 keV photopeak (see section 2.4.3). Each coincidence measurement was performed for approximately 55 minutes (10 million TDC frames) and single measurements for 5.5 minutes (1 million frames). An example of an energy spectrum with LYSO with and without saturation correction is shown in figure 3.11.

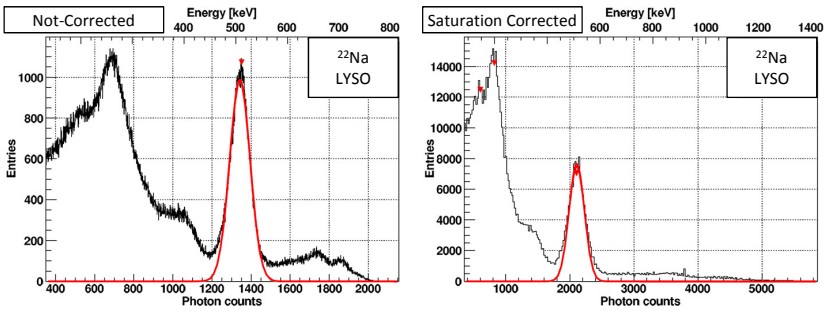

Figure 3.11: ^{22}Na singles energy spectrum with a LYSO scintillator before (left) and after (right) applying the saturation correction, showing in red the single Gaussian fit to obtain the FWHM energy resolution. The broadening of the corrected spectrum is reflected by the higher photon-counts of the photopeak and the better separation of the ^{22}Na high-energetic components.

As explained in section 2.4.3, the resulting energy resolution of the readout of a scintillator by a photodetector is determined by the amount of photons being detected, i.e. by the photodetection efficiency (PDE) of the sensor. The PDE is directly related, among others, to the sensitive area of the detector (see section 2.3.3), which in the DPC's case is directly influenced through the configured cell inhibition. The correlation between the measured energy resolution at different cell inhibitions applying different overvoltages is shown in figure 3.12.

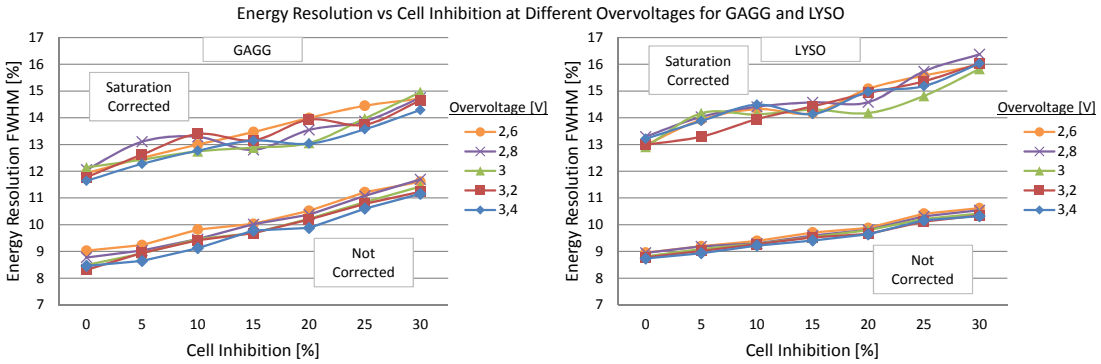

Figure 3.12: Singles energy resolution (% FWHM) versus cell inhibition at different overvoltages for GAGG (left) and LYSO (right). Fluctuations around the linear trend are due to the fitting procedure and the approximations of the applied saturation correction (see section 3.2.2).

Energy resolution worsens linearly with increasing cell inhibition between 0% and 30%. Without applying the saturation correction (see section 3.2.2), the linear trend has a mean coefficient (% energy resolution per % cell inhibition) of 0.09 for GAGG and 0.05 for LYSO. I.e., for every 10% of inhibited cells, energy resolution decreases by almost 1% and 0.5% for GAGG and LYSO, respectively. However, this coefficient is equal for both crystals after applying saturation correction (ca. 1% energy resolution per 10% cell inhibition), as shown by the slopes of the linear trend of each scintillator in figure 3.12. The energy resolution is also affected by the operating voltage, with a mean improvement of 0.55% for GAGG and 0.25% for LYSO by increasing the overvoltage from 2.6 V to 3.4 V.

The other studied operational parameters, namely trigger scheme, validation scheme and tile temperature, showed no effect on energy resolution for both scintillators (plots in appendix A, figures A.4 and A.5).

Table 3.3 summarizes the energy resolution values from measurements at standard conditions for both single and coincidence measurements, showing also the differing GAGG results between the two tiles analyzed. These differences

could be caused by factors affecting the light collection that are not directly related with the sensor itself, such as the individual optical coupling and crystal wrapping. Not-corrected coincidence values are slightly better than not-corrected singles because the high-energetic components of the ^{22}Na source are filtered out, improving the accuracy of the single Gaussian fit. This is no longer observable after applying the saturation correction, thanks to a better separation between the high-energetic components and the 511 keV peak.

		GAGG		LYSO	
		Singles	Coincidences	Singles	Coincidences
Tile 1	Not Corrected	11.6	10.3	9.2	8.2
	Saturation Corrected	13.9	13.8	13.4	13.7
Tile 2	Not Corrected	9.5	7.9	9.4	8.4
	Saturation Corrected	12.0	11.9	13.6	13.5

Table 3.3: Energy resolution values (% FWHM) for both scintillators with standard configuration of parameters.

The effect of changing only the applied overvoltage with all other parameters fixed can be seen in the overlapped energy spectra shown in figure 3.13.

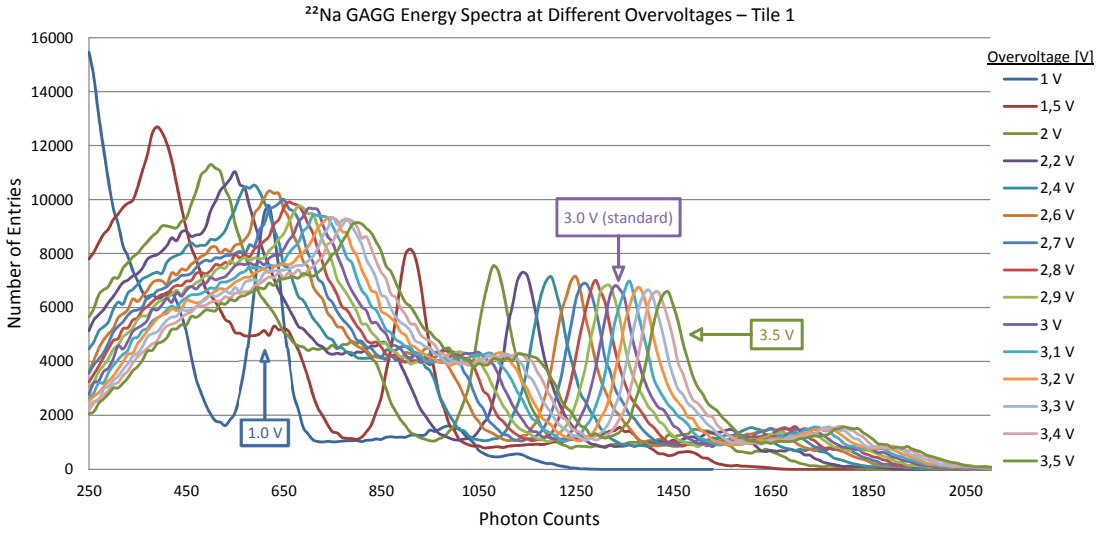

Figure 3.13: ^{22}Na singles energy spectra for GAGG applying different overvoltages (not corrected for saturation). LYSO energy spectra show the same behavior (see appendix A, figure A.6). For visualization purposes, only events with more than 250 photon counts are shown.

With increasing bias, the 511 keV photopeak is located at a higher value of photon counts, due to the increased photodetection efficiency. At the same time, the peak's amplitude in the histogram is reduced, i.e. the frequency of counted events decreases. This is caused by the higher DCR at higher operating voltages, which induces a larger number of dark-count validated events. Those events, due to their lower number of discharged cells, are located in the lower portion of the histogram. For a better visualization of the energy spectra, the curves in figure 3.13 show only events with more than 250 photon counts. The behavior of the lower-count events is addressed in section 3.3.5.

3.3.5 Duty-Cycle

As introduced in section 3.3.4, a configuration of operational parameters producing a higher dark-count-rate induces frequent validation of low-count events, which are histogrammed closer to the origin in the resulting energy spectrum. This phenomenon can be appreciated in figure 3.14.

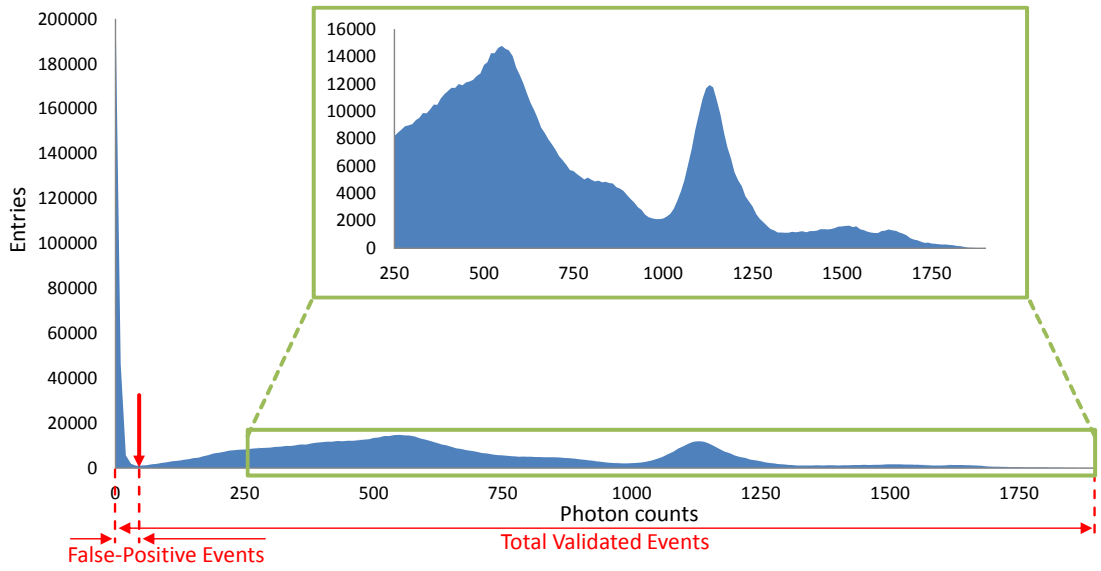

Figure 3.14: ^{22}Na singles energy spectra (not corrected for saturation) for LYSO with standard operational parameters, showing the high occurrence of dark-count validated events and their low photon count.

Despite the low photon counts per event, their frequency is much higher than that of events caused by scintillation light. Based on it, a new concept named the *dark-count induced duty-cycle* is introduced and defined as:

$$Duty - Cycle_{DCR} = \frac{False - Positive\ Events}{Total\ Validated\ Events} \tag{3.4}$$

where the false-positive events are defined as all events to the left of the minimum found between the dark-count peak and the Compton scattered events (see figure 3.14). With this definition, the false-positive events represent the acquisition time that the system is busy processing dark-count validated events and, consequently, the duty-cycle is the fraction of the total acquisition time spent on those events. This definition doesn't consider triggered but not validated events (see figure 3.2) and the resulting values are setup-dependent. The analysis is based on the energy spectra of single events. Coincidence measurements don't show the dark-count peak in the energy specta, since the low-count events are mostly filtered when the time coincidence window is applied. However, this filter is applied *a posteriori*, i.e., every sensor acquires single events and then the coincidences are automatically sorted off-line. Therefore, even acquiring coincidences, the sensors spend the same amount of time processing dark-count validated events.

The duty-cycle behavior has been analyzed against different combinations of all operational parameters mentioned in table 3.1. The results shown in figures 3.15, 3.16 and 3.17 are the average between the two analyzed pixels per crystal, since one sensor consistently showed higher duty-cycle values than the other. This behavior is compatible to the different DCR between the pixels in question (for the pixels with GAGG, 66.2 and 96.0 kHz/mm^2, for pixels with LYSO 66.8 and 97.0 kHz/mm^2, all values at -8.6 °C and 0% cell inhibition).

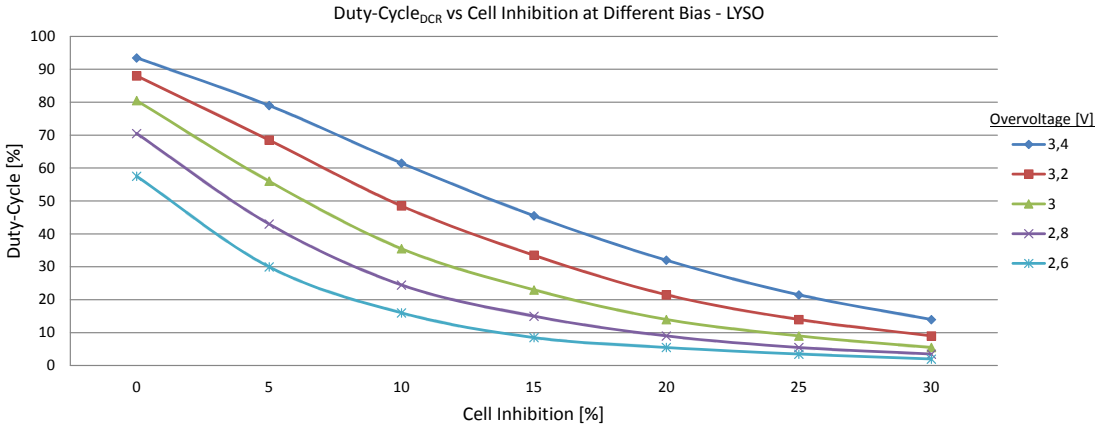

Figure 3.15: Duty-cycle versus cell inhibition for different overvoltages for LYSO (for GAGG, see appendix A.7). Values are averaged between both pixels.

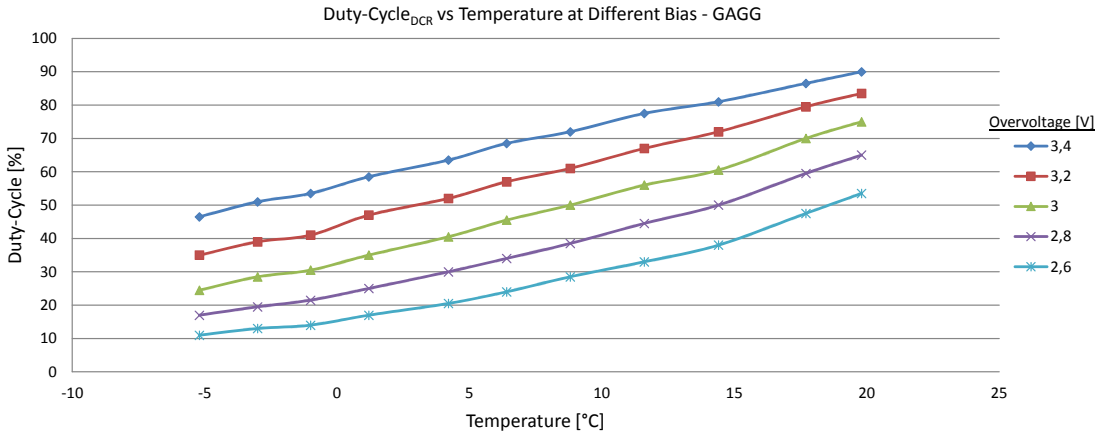

Figure 3.16: Duty-cycle versus tile temperature for different overvoltages for GAGG (for LYSO, see appendix A.8). Values are averaged between both pixels.

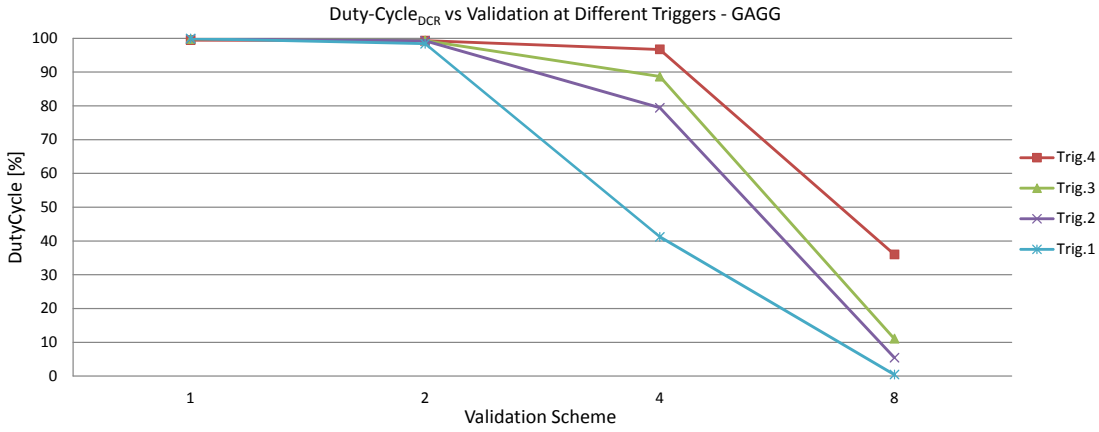

Figure 3.17: Duty-Cycle versus validation and trigger schemes for GAGG (for LYSO, see appendix A.9). Values are averaged between both pixels.

Under conditions increasing the DCR, i.e. higher temperature, higher bias and lower cell-inhibition, the resulting duty-cycle is also increased. With standard operation parameters, it reaches an average value of 42.5% for GAGG and 35.5% for LYSO. Figure 3.17 shows the importance of a proper selection of trigger and validation thresholds. At combinations of only schemes 1 and 2 of these two parameters, the sensor is busy almost 100% of the time acquiring and processing dark-count validated events. For the validation schemes 4 and 8, trigger 4 shows the highest duty-cycle value.

3.3.6 Coincidence Time Resolution

As explained in section 2.4.2, the coincidence time resolution (CTR) of a PET system is an important factor to improve the resulting image quality. For the analysis with the DPC, CTR was measured using a 2 ns coincidence window, combining all the operational parameters shown in table 3.1 and selecting only events with deposited energy between 420 and 600 keV. The energy window in a full PET system is applied to reject gamma-rays being Compton scattered within the patient. Compared to that scenario, the described experimental setup has no relevant scattering matter between the point source and the detectors. Nonetheless, the energy window serves to reject the high-energy photons that only deposit a reduced portion of their energy in the scintillator (Compton interaction), affecting the CTR due to the lower number of generated, and thus potentially detected, scintillation photons. All given CTR values are the full width at half maximum (FWHM) of a single Gaussian fit to the histogrammed time differences between the two involved sensors. Figure 3.18 shows the effect on CTR when an increasing cell inhibition is applied.

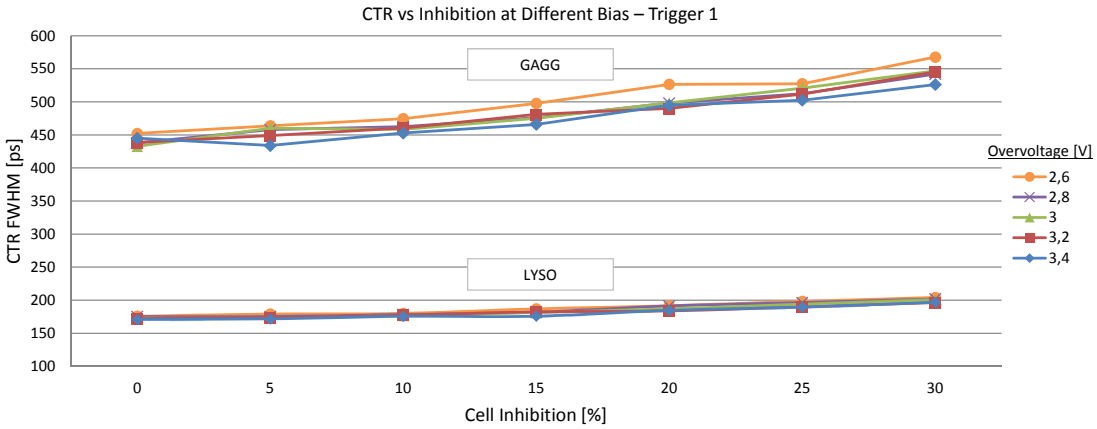

Figure 3.18: CTR against cell inhibition for LYSO and GAGG using trigger scheme 1. CTR decreases with an increasing number of deactivated cells.

When the number of available cells is reduced by 30%, the CTR value increases about 25 ps (15%) for LYSO and 100 ps (22%) for GAGG. The linear relation remains up to around 50% cell inhibition, after which timing resolution degrades much faster, reaching a CTR value of 800 ps for LYSO at 85% cell inhibition (see appendix A, figure A.3). The results also show that CTR is slightly improved by raising the bias voltage, with a mean improvement of ca. 27 ps (6%) for GAGG and 7 ps (4%) for LYSO when increasing the overvoltage from 2.6 V to 3.4 V.

The same behavior against bias is found in figure 3.19, where also the influence of temperature on time resolution is shown. For LYSO, CTR remains constant for all studied temperatures, while for GAGG it improves with increasing temperatures in the analyzed range.

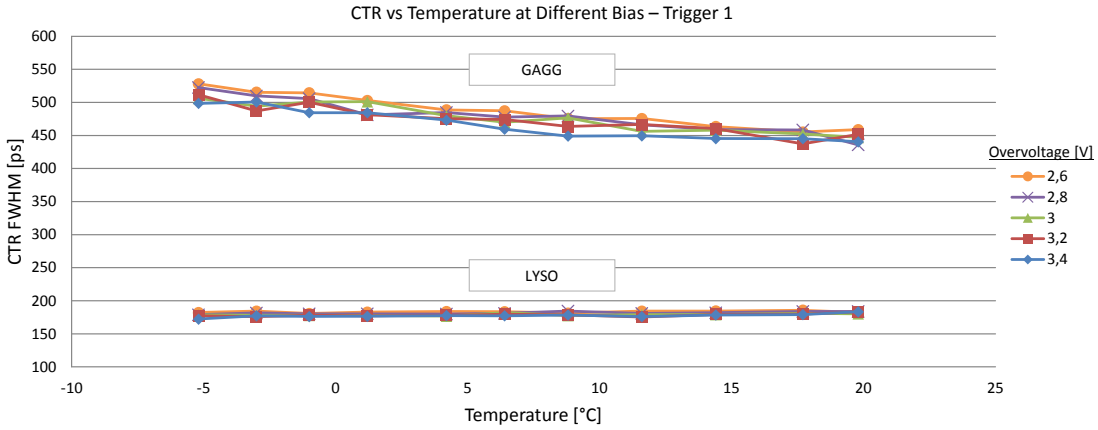

Figure 3.19: CTR against tile temperature at different overvoltages and trigger scheme 1. Values for LYSO remain constant, while GAGG shows an improvement with higher temperatures in the studied range.

In contrast to the trigger configuration, the different validation schemes don't influence the time resolution, as shown in figure 3.20.

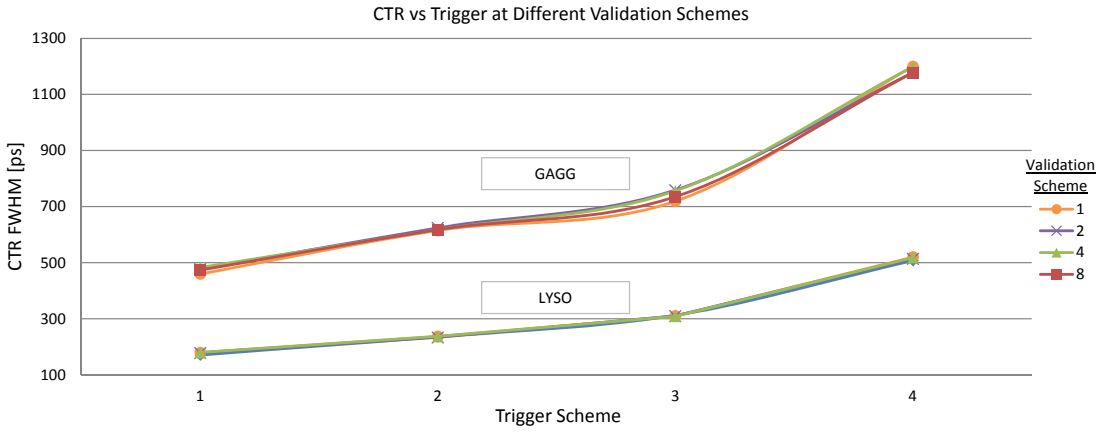

Figure 3.20: CTR against trigger and validation schemes for LYSO and GAGG. Higher trigger schemes result in worse CTR values due to the larger number of photons required to be detected with a specific spatial distribution.

As expected for higher trigger schemes, the CTR worsens due to the larger number of photons required to be detected, in a specific sub-pixel spatial distribu-

tion (and thus the longer waiting time), to reach the trigger threshold. Table 3.4 summarizes the CTR values from measurements at standard conditions changing only the trigger scheme, showing also the difference in timing performance of the two different scintillators. LYSO shows a CTR value below 180 ps, while GAGG is around 460 ps.

Trigger Scheme	1	2	3	4
Avg. nr. of photons to trigger (71)	1	2.333	3.0	8.333
LYSO	177	232	307	505
GAGG	458	593	710	1138

Table 3.4: Measured CTR values (ps, FWHM) for LYSO and GAGG at 3.0 V overvoltage, 5.6°C and 10% cell inhibition. Only events with deposited energy between 420 and 600 keV are considered.

3.4 Performance Analysis for PET

Intrinsic properties of silicon photomultipliers are comparable for the studied DPC and analog devices. Both, the breakdown voltage temperature coefficient and optical crosstalk (see sections 3.3.1 and 3.3.2), are similar to the ones of state-of-the-art analog SiPMs (40). The DPC's behavior against temperature and bias voltage variations is also as expected for a SiPM. The main differences between analog SiPMs and the analyzed digital approach are induced by the logic of the implemented acquisition sequence and its related parameters.

As introduced in section 2.4, the image quality of PET is affected by the performance of a detector in terms of detection sensitivity, energy resolution and coincidence time resolution. The experimental results obtained with the DPC are analyzed placing the main emphasis on these three characteristics and the impact caused by the different configuration parameters of this sensor.

3.4.1 Dark-Count-Rate and Duty-Cycle

The results shown in section 3.3.3 show the clear dependence of DCR on temperature and the applied bias voltage. Reducing both parameters decreases DCR. However, a lower overvoltage reduces the photodetection efficiency (PDE) of SiPMs. By means of inhibition of single cells, the sensor's DCR can also be strongly reduced, though consequently reducing the PDE by the same applied percentage,

due to the decrease of the pixel's effective fill factor (see section 2.3.3). Therefore, to avoid the tradeoff between loss of PDE and better DCR values, the latter can be more effectively reduced by working at lower temperatures. Nonetheless, since working at 0% cell inhibition results in a very high DCR, an inhibition of 10% is an appropriate configuration to achieve, in terms of DCR, a performance comparable to state-of-the-art analog SiPMS. This conclusion is based on the results shown in table 3.5, where a comparison is presented of the DCR between different SiPMs, obtained from measurements performed in our group.

Temperature	Philips DPC3200-22-44 0% Inhibition	Philips DPC3200-22-44 10% Inhibition	Ketek PM1150NT 1.2×1.2 mm^2	Ketek 3350 3×3 mm^2	Hamamatsu S12652-050C 3×3 mm^2
Room	770	260	420	300	400
Low	140	26	–	–	30
PDE	40%	36%	55%	55%	45%

Table 3.5: DCR (kHz/mm^2) comparison of digital and analog SiPMs. Overvoltage is 3.0 V/10%, room and low temperatures are 23.8°C/25°C and 1.2°C/0°C for the digital/analog devices. All PDE values are at the corresponding wavelength sensitivity peak.

Dark-counts have strong influence on a measurement, since DC-triggered events induce dead time in the involved die (2×2 pixels). At lower dark-count-rate, those events are not validated and the dead time is mainly the recharge period (20 ns) of the cells. At higher DCR though, DC-triggered events with enough photon counts are falsely validated and the complete acquisition sequence is performed, adding not only the integration time but also the readout process (680 ns) to the dead time (see figure 3.2). Scintillation light being detected during this time is not correlated to the time stamp registered due to dark-counts. Consequently, the integration time doesn't properly overlap with the scintillation decay, leading to a wrong energy information extracted from the scintillation pulse. The detected event is, therefore, not usable for PET. The higher the number of events that are lost because of this phenomenon, the lower the resulting system sensitivity, as introduced in section 2.4.1.

As shown in figure 3.13, these false-positive events reduce the detection frequency of true events originating from incoming light. The ratio of acquisition time with the sensor being busy processing these unwanted events has been defined as the dark-count induced duty-cycle in section 3.3.5. A configuration producing higher DCR induces a larger duty-cycle of the sensor, as shown against

cell inhibition, tile temperature and bias voltage in figures 3.15 and 3.16.

The scintillator properties play a role in the duty-cycle value as well, since a higher interaction probability of the 511 keV results in a higher probability of true validated events. The measurements with LYSO consistently showed a lower (better) duty-cycle value than GAGG, being compatible to its slightly higher density and higher effective atomic number. Hence, a scintillator with a better detection efficiency (*stopping power*, see section 2.3.2) reduces the DPC's duty-cycle and, consequently, improves the system sensitivity. Further setup-related conditions, such as the activity of the source and its distance to the crystals, also impact the resulting duty-cycle values. Therefore, a quantitative analysis of it is only valid for every particular application and system setup.

The adjustable trigger and validation schemes have no direct influence on the DCR value of the DPC. However, their repercussion in the acquisition sequence is clearly demonstrated in figure 3.17. For a lower combination of both thresholds, almost 100% of the time is spent processing false events. Counterintuitively, the more restrictive threshold combinations (trigger 4 plus validations 4 or 8) produce higher duty-cycle values, i.e. a higher number of dark-count validated events, compared to less demanding trigger configurations. The reason for this behavior lies in the logic of the acquisition sequence and the requirements to reach both thresholds, as introduced (see figures 3.2 and 3.4). The count of cells being discharged is summed up from the beginning of each sequence until the final recharge process, which happens either after a non-validation or at the end of a full acquisition. The fulfillment of the predetermined trigger condition can happen at any time until the end of a TDC frame is reached (i.e., during a time window of up to 327.68 μs with deactivated RTL refresh (71)). If no trigger is generated during this time, a reset occurs and the count is restarted. The longer it is waited for the threshold to be exceeded, the higher the probability of cells to be fired by dark-counts. Therefore, during the"trigger-waiting-time", and since the trigger scheme imposes a sub-pixel-based spatial distribution of fired cells, a high number of cells can be discharged before the trigger threshold is reached. These cells are also taken into account during the following validation stage (which also imposes a sub-pixel-based spatial distribution of the fired cells). Thus, a higher trigger scheme passes a higher cell-count to the validation stage, making that event more likely to be validated. For the same reason, a lower trigger scheme passes a lower cell-count to the validation stage, making that event less likely to be validated in absence of scintillation light. This behavior is shown in figure 3.21, where the ratio of validated events out of the total triggered ones is depicted.

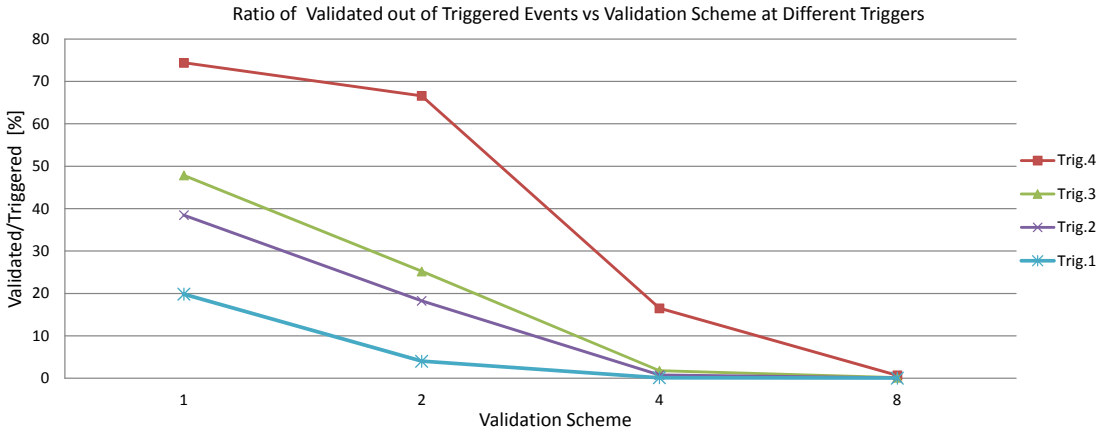

Figure 3.21: Ratio of validated events out of the total triggered ones versus different validation schemes. Lower trigger schemes are validated less frequently than higher trigger schemes.

As a consequence, a higher trigger scheme can generate more dark-count validated events than a lower scheme, explaining the duty-cycle behavior from figure 3.17.

Summarizing, the trigger and validation configuration has a very important impact on the sensitivity of the sensor, since high duty-cycle values imply a high fraction of time acquiring not useful events. This dead-time has been shown to be also relevant when several dies share light from an incoming event (e.g. crystal arrays or monolythic blocks), resulting in loss of an important fraction of light (75). A proper configuration of these two parameters, together with a lower dark-count-rate, has a positive impact in the sensitivity for the sensor's implementation in a PET scanner. Since PDE also affects the detection sensitivity, DCR should be preferably reduced by means of low operating temperatures instead of low bias voltages and high cell inhibition. However, the most active cells need to be inhibited, since the duty-cycle at the standard operational configuration is reduced at more than half between 0% and 10% cell inhibition (see figure 3.15).

3.4.2 Energy Resolution

The energy resolution is directly influenced by the ability of a silicon photomultiplier to detect as many as possible scintillation photons caused by the energy deposition of a 511 kev gamma-ray in the crystal. To achieve this, the PDE of the sensor plays a crucial role. Similar to analog SiPMs, the DPC's PDE can be increased with higher bias voltages, as shown by the resulting better energy

resolution values as well as the larger number of photon counts at the 511 keV photopeak (see figure 3.13). However, due to the limited range of applicable overvoltage supported by the DPC, its impact is lower compared to that of cell inhibition, the other operational parameter influencing the detection efficiency (see figure 3.12). This influence of cell inhibition on the performance is higher for a brighter scintillator like GAGG, due to the comparatively higher loss of photon counts when fewer cells are enabled. On the other hand, energy resolution is not directly affected by the DCR, as evidenced by the constant measured values for all temperatures in the analyzed range between -5°C and 20°C (see appendix A, figure A.5). However, due to the active recharge of cells only at the end of each acquired event, dark-count fired cells induce a lower number of effectively available cells, altering the count of real impinging photons while also increasing the sensor saturation. This represents a main drawback of the DPC compared to analog SiPMs, where cells are passively recharged during one acquisition and able to fire again, increasing dynamically the number of effectively available cells. Therefore, lower sensor temperatures can indirectly influence the energy resolution, by reducing the DCR and consequently allowing a lower cell inhibition, thus increasing the PDE.

The two other analyzed operational parameters, namely the trigger and validation schemes, showed no influence in the energy resolution values. This is due to the constant validation length adjusted for all measurements (10 ns). Indepently of the applied scheme, the validation phase is always run for this defined time, even if the threshold is reached earlier. As a result, the total time for counting photons is always the fixed validation and integration lengths (here, 10 plus 85 ns) plus the variable trigger time. In the case of a very fast trigger, the total time is at least 95 ns, which comprises the decay time of both analyzed scintillators, allowing to properly count the majority of the generated photons.

The energy resolution measured at standard operational conditions including saturation correction is comparable to that reported for same-size LYSO crystals and analog SiPMs in (40). The same study shows around 2% better values for GAGG, as expected for a brighter scintillator (30). This difference is caused by different factors. First, the PDE of the DPC is lower for the peak emission wavelength of GAGG compared to LYSO (respectively 30% at 520 nm and 39% at 420 nm, at 0% cell inhibition (69)) and about 10% lower than that of the device used in the referenced study. Due to the doubled light yield of GAGG versus LYSO and the saturation of the DPC, this results in a comparatively larger number of photons not being detected and, thus, a reduction of the energy

resolution.

Second, the energy histograms of the GAGG crystals showed permanently a prominent "shoulder" from the 511 keV peak towards higher energies, which wasn't observable with LYSO. This was initially believed to be caused by the Compton events from the 1273 keV gamma-rays of the ^{22}Na source being overlapped with the 511 keV photopeak due to the sensor's saturation. However, this phenomenon neither disappeared after applying the saturation correction, nor when measuring coincidences. To completely discard the influence of the high-energetic components, measurements with the same described setup and standard operational parameters with a 2 MBq ^{18}F source as well as a 3.7 MBq ^{137}Cs were performed. The results, shown in figure 3.22, proof that this phenomenon is not originated by higher energy events from ^{22}Na.

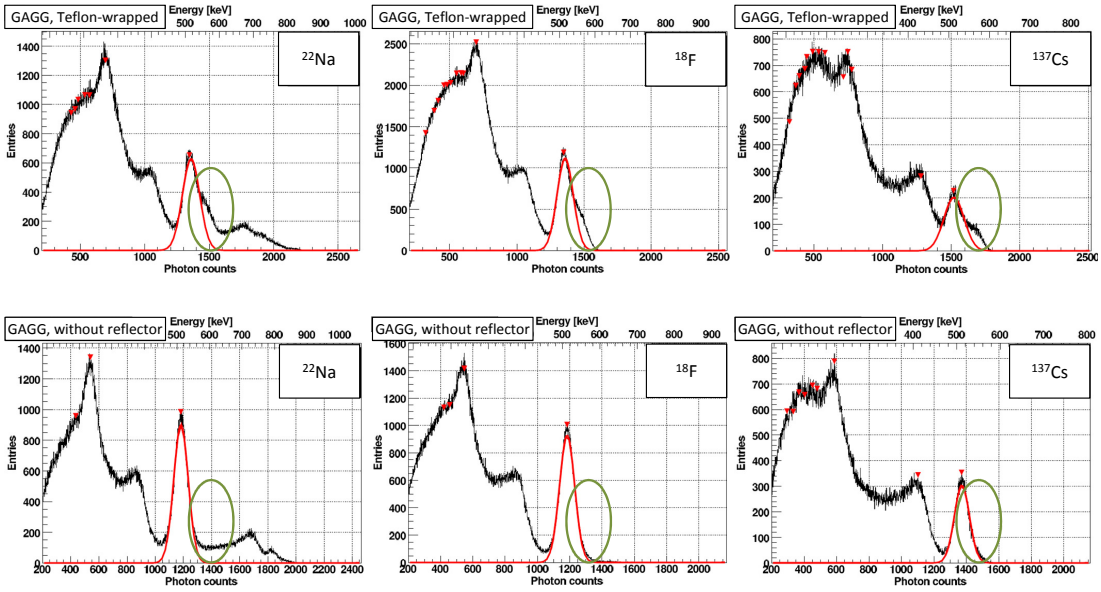

Figure 3.22: Singles energy spectra (not saturation corrected) of a $2 \times 2 \times 6$ mm^3 GAGG with ^{22}Na (left), ^{18}F (middle) and ^{137}Cs (right). The upper row corresponds to Teflon-wrapped crystals and the bottom row to non-wrapped. The red line indicates the applied single Gaussian fit and the green circle the "shoulder" anomaly, which disappears without the reflective wrapping. This behavior is not shown by LYSO (see figure 3.11).

Repeating the same measurements but without the Teflon-wrapping showed no evidence of this phenomenon. Furthermore, measurements with a bigger Teflon-wrapped crystal matching the DPC's pixel size ($3.2 \times 3.8775 \times 8$ mm^3) didn't show this behavior (93), nor did it when measuring with the same ($2 \times 2 \times$

6 mm^3) crystal and analog SiPMs (40). An explanation for this response of the DPC to a high number of photons (GAGG + Teflon-wrapping) concentrated on a reduced sensitive surface (ca. 1/3 of the pixel) is currently subject to further investigation. This phenomenon also denotes that deeper knowledge of this new technology is needed towards an optimum application in PET systems.

The described anomaly in the energy spectrum reduces the accuracy of the applied single Gaussian fit, affecting the thereby calculated energy resolution values for GAGG. Regardless of the scintillator, a fitting procedure including compton-background rejection should be applied, in order to extract more accurate energy resolution values from the data. Nonetheless, the implemented algorithm gives reliable values to assess the influence and trends caused by changing the DPC's operational parameters. It also proves that the DPC's performance in terms of energy resolution is comparable to similar analog-SiPMs-based setups, allowing its potential implementation in a PET system for rejection of small-angle scattered events (see section 2.4.3).

3.4.3 Coincidence Time Resolution

The dSiPM can be configured to trigger at 4 different schemes, each one associated with an average number of incoming photons that have to fulfill a specific sub-pixel-based spatial distribution upon detection (71). The time stamp for each event is saved when the photon count threshold is reached. Due to this implementation, CTR increases with higher trigger schemes due to the higher waiting time needed to reach the configured threshold. This behavior can be appreciated for both scintillators in figure 3.20, which also shows that different validation schemes have no influence on the coincidence time resolution.

The experimental results show that CTR worsens when the sensor's PDE is lowered by both reducing the bias voltage and, more significantly, increasing cell inhibition (see figure 3.18). This is due to the fact that, with a reduced number of available cells, it is less likely to detect the fastest arriving photons. Therefore, CTR can be indirectly improved by operating at low temperatures, decreasing so the sensor's DCR and consequently allowing a higher percentage of active cells. However, the dark-count-rate itself doesn't directly affect the time resolution of the DPC, as proven by the constant CTR values for LYSO when temperature is changed between -5°C and 20°C (see figure 3.19). The same measurement shows the better (lower) time resolution values for GAGG with higher temperatures. This behavior is not attributable to the DPC but compatible with the scintillator's

intrinsic properties reported by its manufacturer in (99) for the analyzed range of temperature.

The difference in timing properties between the two studied scintillators is clearly reflected by the achieved results, showing the faster characteristics of LYSO over GAGG. Operating the DPC at the standard configuration, CTR FWHM values of less than 180 ps and 460 ps are achieved with LYSO and GAGG, respectively, being comparable to values reported for same-sized crystals coupled to analog SiPMs in (40). Therefore, the DPC, thanks to its integrated processing electronics and combined with a fast scintillator, is suitable for its application in a *time-of-flight* (TOF) PET system, with the consequent improvements in image quality as explained in section 2.4.2.

3.5 Conclusion

A characterization of five operational parameters affecting the performance of a fully digital silicon photomultiplier, the DPC, has been performed for its implementation in a PET system. The analysis considered two candidate scintillators, a commonly used one (LYSO) and a newly developed one (GAGG). The studied parameters included the trigger scheme, validation scheme, cell inhibition, bias voltage and temperature and their influence on the dark-count-rate, photodetection efficiency and detection sensitivity. In terms of energy and time resolution, the analyzed device performs similar to state-of-the-art analog SiPMs. The main differences are induced by the logic of the implemented acquisition sequence and its related parameters.

At operating conditions resulting in a high DCR, dark-count-triggered events are more likely to be falsely validated. Scintillation events being detected during a dark-count-started acquisition have wrong energy and time information, and are thus not useful for PET. This induces a sensor's dead time, reducing the detection frequency of true events and thus the system sensitivity. This can be improved by selecting a proper combination of trigger and validation schemes, but most importantly reducing the dark-count-rate. This can be achieved by means of cell inhibition, reduction of the bias voltage and operation at lower temperatures. However, the two first (i.e. less active cells or lower overvoltage) also induce a reduction in the photodetection efficiency, negatively affecting the resulting energy and coincidence time resolution.

Based on all presented results and aiming to improve crucial properties of a PET scanner, such as energy and time resolution and system sensitivity, the most

suitable combination of DPC operational parameters for their implementation in a TOF-PET system is trigger scheme 1, validation scheme 8, 10% cell inhibition and 3.0 V overvoltage. Temperature should be as low as possible, which might represent a technical challenge for the integration in a full PET system. Working slightly over 0°C already improves considerably the performance compared to room temperature.

The analyzed digital SiPMs are good candidates for their implementation together with a fast scintillator, like LYSO, in a time-of-flight capable PET system. GAGG is a good candidate for a high energy resolution system, although not for TOF-PET, due to its slower timing properties, and not in combination with the DPC, due to the low PDE at the GAGG preferred emission wavelength. To take better advantage of the GAGG's high light yield avoiding saturation, a suitable sensor should have a larger number of cells and/or a higher dynamic range for the cell recharge during the acquisition of an event.

4

Monte Carlo Simulation Study of a novel Cherenkov-Based Detector Block for PET[1]

4.1 Introduction to Cherenkov Radiation for PET

As explained in chapter 2, traditional PET scanners consist of a ring of detector blocks registering high-energetic photons through its conversion into scintillation light. Accurate coincidence time resolution (CTR) and depth-of-interaction (DOI) measurements of every detected event are crucial for the resolution of the resulting PET image, with the properties of the scintillator playing a fundamental role (100). The scintillation mechanism contributes to the CTR through its intrinsic rise and decay time as well as the light transport in the crystal (101). In a traditional single-readout scheme, reflected photons can spend a significant amount of time travelling to the detection surface, thus affecting the time resolution (102). The precision of the DOI determination is also influenced by the scintillator through its size as well as the isotropic photon emission.

In this chapter, a novel concept for a scintillation-independent and DOI capable TOF-PET detector is introduced and analyzed. Instead of the standard single-sided crystal readout of isotropically emitted scintillation light, the concept defines for the first time a PET sensor unit based only on the detection of Cher-

[1]The content of this chapter is based on the publication "CHERENCUBE: Concept Definition and Implementation Challenges of a Cherenkov-based Detector Block for PET", accepted for publication in the scientific journal *Medical Physics* in April 2015, in press. See Appendix D.

enkov photons, by taking into account the well-defined geometrical and fast temporal properties of this particular radiation.

Cherenkov photons are emitted when a charged particle travels faster than the speed of light in the same medium (26). The photons are promptly emitted with a fixed angle along the parent particle's trajectory, forming the so called Cherenkov cone. This angle is only defined by the velocity of the particle (i.e., its energy) and the refractive index of the medium, n, which defines the speed of light in it. Defining β as the ratio of the particle velocity, v, to that of light in vacuum, c, the Cherenkov angle is determined by the equation (103):

$$\cos\theta = \frac{1}{\beta\, n}, \qquad \beta = v/c \tag{4.1}$$

The contribution of Cherenkov radiation to the time resolution of a PET detector has been studied in (101)(104), showing that Cherenkov photons can improve the total rise-time of the optical signal emitted from the crystals (i.e. considering both scintillation and Cherenkov photons) due to their faster generation mechanism. The rise-time of the crystal's light-yield, on its turn, plays an important role in the timing resolution of a TOF-PET system, since coincidence timing is determined by the earliest portions of the rise-time distribution (60)(105)(106). The feasibility to measure Cherenkov photons generated by 511 keV gamma-rays using lead crystals and fast photodetectors has already been proven (102), reaching coincidence time resolutions of 80 ps (sigma) in a back-to-back setup with 15 mm long crystals. In (107), lead glass was used as a Cherenkov radiator in a similar setup, achieving a coincidence time resolution of 170 ps (FWHM). In the same work, the authors propose a conceptual design of a TOF-PET system based only on Cherenkov radiation and estimate its performance by means of Monte Carlo simulations.

However, all these approaches consider either combining scintillation and Cherenkov photons, without a possible discrimination among the two phenomena, or are exclusively based on single-sided readout of the crystal. In both scenarios, the geometrical properties of Cherenkov radiation are not considered. On the other hand, multiple-sided readout has been already implemented for PET detectors, to measure distribution patterns of scintillation light inside highly voxelated scintillators. By means of several photodetectors covering each crystal's face, the crystal voxel where the energy deposition occurred is precisely determined and, therefore, the depth-of-interaction of the gamma-ray (68). Still, no studies of 6-sided detection of Cherenkov radiation for PET have been performed.

This study analyzes by means of theoretical calculations and Monte Carlo simulations a newly defined detection concept and its potential advantages towards reaching a Cherenkov-only detector block for TOF-PET with DOI capability, while simultaneously defining its constraints and the requirements for its practical implementation considering both the Cherenkov radiator and the photodetector.

4.2 Concept Definition and Theory

The proposed detection concept, the "CHERENCUBE", consists of a cubic Cherenkov radiator with one photodetector coupled individually to every face of the crystal. The sensitive area of the photodetector matches that of the cube face. A 511 keV gamma-ray originating from a PET radiotracer enters the radiator and transfers its energy to one electron either by Photoelectric Effect or Compton scattering (see section 2.3.1), ejecting it from the atom with a velocity proportional to the absorbed energy. If this velocity is higher than the Cherenkov threshold $\beta > 1/n$ a Cherenkov cone is generated, with its axis defined by the electron's trajectory and its lateral surface by both the Cherenkov angle and the trajectory of the emitted photons. The number of generated Cherenkov Photons, N, is defined by the following equation (101):

$$\frac{dN}{dx} = 2\pi\alpha \left(\frac{1}{\lambda_1} - \frac{1}{\lambda_2}\right)\left(1 - \frac{1}{\beta^2\, n^2}\right) \tag{4.2}$$

where x is the path length of the electron in the radiator's material, α the fine structure constant and $\lambda_{1,2}$ the wavelength range. Upon their arrival on one or more faces of the cube, the photons project a circular or elliptical pattern, depending on the relative orientations of the cone and cube axes. A simplified 2D-scheme of the detection concept can be seen in figure 4.1.

The electron can be scattered multiple times before its energy has been deposited completely. If its velocity after each interaction is still over the Cherenkov threshold, then a new cone can be emitted, belonging to the same interacting gamma-ray but centered in the modified electron's trajectory. Every new oriented cone results in the projection of another photon pattern in the detectors, creating a phenomenon defined as multiple Cherenkov cones per event. A graphical representation can be seen in figure 4.2.

The 6-sided readout scheme aims to detect the optical photons before any internal reflection, allowing the use of the geometrical properties of Cherenkov radiation while also reducing the influence of the light transit time inside the

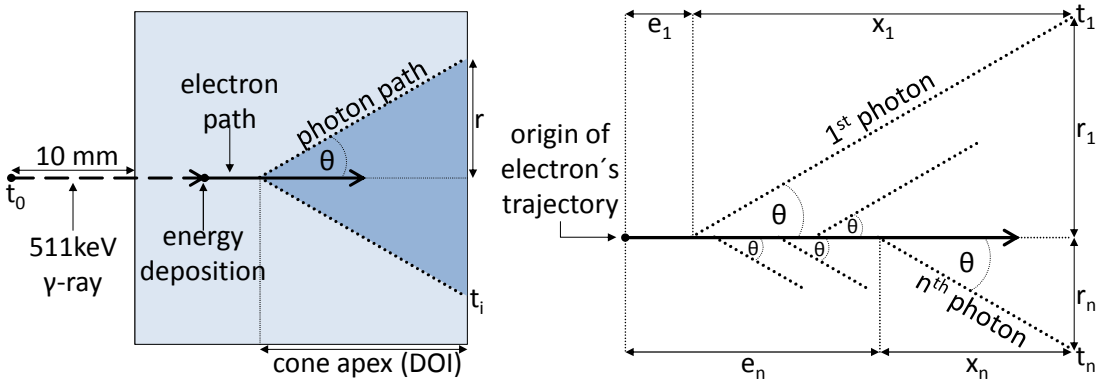

Figure 4.1: 2D-scheme of: left) a Cherenkov cone aligned perpendicularly to one cube face projecting a circular pattern of photons; right) photon emission distribution along the electron's path.

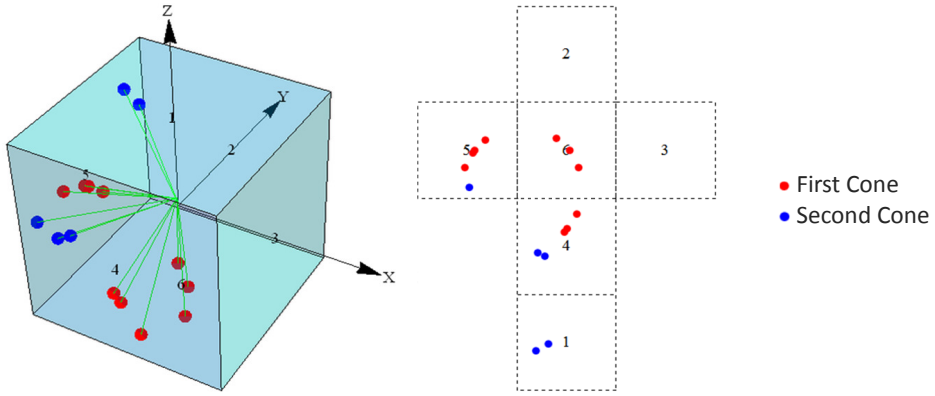

Figure 4.2: Graphic representation of multiple Cherenkov cones belonging to the same event. The 2D diagram shows the projections of the detected patterns and the photon distribution per detector.

crystal. To achieve this, the photodetector is assumed to have 100% detection efficiency and a pixelated position-sensitive surface with a spatial resolution in the range of tens of micrometers, to provide individual detection coordinates of each photon. Since the condition for Cherenkov radiation is $v > c/n$, the threshold particle speed fulfills $\beta_{th} = 1/n$ and $\theta_{th} = 0°$. The energy threshold for an electron to cause Cherenkov radiation is given by (108):

$$E_{th} = \frac{mc^2}{\sqrt{1-\beta_{th}^2}} = \frac{mc^2 n}{\sqrt{n^2-1}} = \frac{(511keV)\,n}{\sqrt{n^2-1}} \tag{4.3}$$

From equations 4.1 and 4.3, it follows that:

$$\beta^2 = 1 - \left(\frac{mc^2}{E}\right)^2 \rightarrow \cos\theta = \frac{1}{\sqrt{1 - \left(\frac{mc^2}{E}\right)^2}\, n} \tag{4.4}$$

The cone angle is then confined to a range, with its lower limit defined by the Cherenkov threshold and the upper by the maximum energy of the electron after being ejected by the photoelectric effect of a 511keV gamma-ray. These limits intrinsically imply an energy cut to potentially reject some of the gamma-rays that have been previously scattered, e.g. inside the patient in a PET scanner (see section 2.4.3).

Since the refraction index of the Cherenkov radiator is known, by using the spatial distribution of the detected photons (i.e., the cone radius) and the Cherenkov angle range, the position of the cone apex could also be estimated and with it the depth of interaction (DOI) inside the crystal. This implies the assumption that the photon emission distribution along the electron's path (see figure 4.1) is negligible compared to both the length of the corresponding photon paths and the size of the radiator and, therefore, the precision of the DOI estimation is not compromised by this factor. With the proposed approach, the time elapsed between photon generation and detection is minimized. Furthermore, due to the prompt emission of the Cherenkov photons, no delay is induced as compared to the scintillation rise time in standard PET detectors.

In the best-case scenario, all these characteristics combined would allow to have a detector block with the potential to build a PET system with high time and spatial resolution. In the following sections, the practical and model inherent constraints to achieve this scenario are analyzed by means of Monte Carlo simulations.

4.3 Monte Carlo Simulation

The Monte Carlo simulations of the proposed detection concept were performed with Geant4, v9.4. p01 (109). The reliability of the Geant4 electromagnetic physics models at the simulated low-energy level has been quantitatively validated against external reference libraries as well as experimental data (110)(111)(112).

The simulated detector block consisted of a cubic crystal with one photodetector attached directly to each one of the cube's faces. The sensitive area of the detector matched exactly the size of the crystal. The crystal dimensions were varied in 1 mm steps starting from $1 \times 1 \times 1$ mm^3 up to $10 \times 10 \times 10$ mm^3,

with the size of the photodetector being adjusted accordingly. For every crystal configuration, 5 independent simulations of ten thousand 511 keV gamma-rays were triggered at a fixed distance of 10 mm, perpendicular and centered towards one cube face. The trigger of each gamma-ray sets the starting time t_0 for the simulation (see figure 4.1).

The crystal material chosen was $PbWO_4$ (lead tungstate, commonly known as PWO), which has been proposed as a promising Cherenkov radiator in terms of detection efficiency (102)(107) and has been characterized in detail (113). The material definition for $PbWO_4$ was obtained from the NIST database included in Geant4 and its optical properties from (114) for the wavelength range between 330 nm and 840 nm. Within this range, the refractive index varied between 2.52 and 2.17. The scintillation properties of PWO were included in the simulations, but only Cherenkov generated photons were considered in the data analysis.

The photodetectors were simulated to be ideal, i.e. with perfect photodetection efficiency and infinite time resolution. Therefore, every photon that arrived at a cube face was detected and all timing values consider only the travel and spread time between t_0 and the photon's detection upon arrival at the photodetector, t_i (see figure 4.1). An example of the setup and one simulated gamma-ray can be seen in figure 4.3.

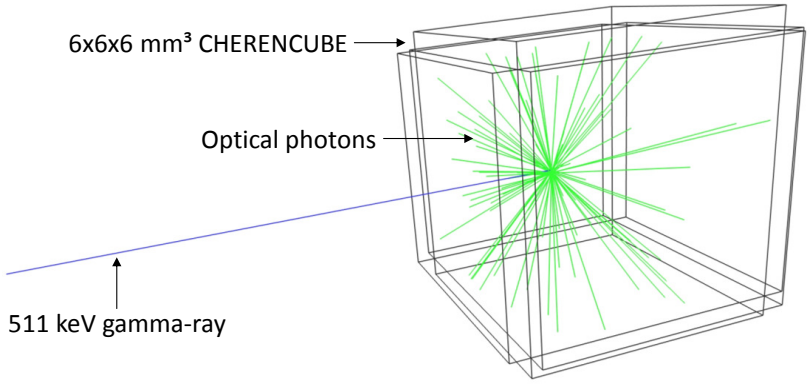

Figure 4.3: One 511 keV gamma-ray shot from 10 mm distance to a $6 \times 6 \times 6$ mm^3 CHERENCUBE. Both scintillation and Cherenkov photons are generated and ideally detected upon arrival at one of the six photodetectors. Only Cherenkov photons are considered in the analysis.

For every generated and tracked particle, the information about its creation process, parent and daughter particles, energy, origin coordinates, trajectory and time and position of detection were exported in list mode and analyzed using the computation software Mathematica (115).

4.4 Simulation Results

In the following, the Monte Carlo simulation results are presented showing one particular CHERENCUBE size, as an example for every analyzed characteristic. The corresponding results obtained for all other simulated dimensions are included in appendix B.

4.4.1 Detection Statistics

As explained in section 2.4.1, the sensitivity of a PET scanner is highly influenced by the detection efficiency of the individual detector blocks, which is related (among others) to the crystal material and its geometry. For the analysis of the CHERENCUBE, a detected event is defined as one gamma-ray that deposited energy in the crystal and generated Cherenkov photons, from which at least one was detected. Detection efficiency is then defined as the ratio of detected events to the total number of triggered 511 keV gamma-rays. The graph in figure 4.4 illustrates the rapid drop in detection efficiency if a minimum threshold on the number of photons to be detected is included.

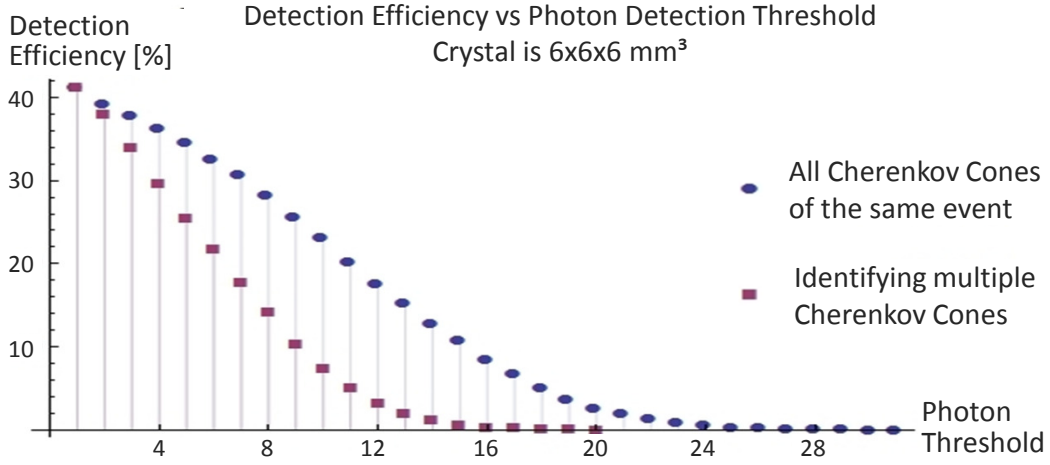

Figure 4.4: Detection efficiency vs photon threshold for a $6 \times 6 \times 6$ mm^3 CHERENCUBE. For further dimensions, see appendix B, figure B.1.

Larger crystals have higher detection efficiency due to the increased interaction volume of the detector. A comparison for the different crystal sizes at a threshold of 1, 10 and 20 photons showing the mean value over the 5 independent simulations is shown in Table 4.1:

Photon Threshold	Cube Length [mm]									
	1	**2**	**3**	**4**	**5**	**6**	**7**	**8**	**9**	**10**
1	8.2	15.8	22.9	29.2	35.3	40.7	45.5	50.1	54.4	58.6
10	4.3	8.6	12.4	16.0	19.4	22.3	24.4	26.9	29.1	30.4
20	0.7	1.3	1.7	2.1	2.3	2.5	2.6	2.6	2.9	2.8

Table 4.1: Detection efficiency (%) for all crystal sizes at a threshold of 1, 10 and 20 detected photons.

Figure 4.4 also shows how the detection efficiency is influenced through the multiple Cherenkov cones per event (previously introduced in figure 4.2): without cones discrimination, the total number of photons per event is larger (sum of photons from all same-event cones) and the detection threshold is less restrictive. However, multiple Cherenkov cones per event generate a larger number of different detected patterns, each one with a portion of the total number of same-event photons. If detection efficiency is defined considering each individual detected cone, then the photon-detection threshold is more restrictive, represented by the lower curve in the graph of figure 4.4. Table 4.2 shows these values averaged over the 5 independent simulations for the different crystal sizes at a threshold of 1 and 10 photons per cone. In contrast to the values presented in table 4.1, the detection efficiency for all crystal sizes has already dropped to zero at the 20-photons-threshold.

Photon Threshold	Cube Length [mm]									
	1	**2**	**3**	**4**	**5**	**6**	**7**	**8**	**9**	**10**
1	8.2	15.8	22.9	29.2	35.3	40.7	45.5	50.1	54.4	58.6
10	0.8	2.6	4.2	5.4	6.3	7.1	8.1	8.6	9.1	9.5

Table 4.2: Detection efficiency (%) individually analyzing multiple cones per event for all crystal sizes at a threshold of 1 and 10 detected photons. Detection efficiency is zero at a 20-photons-threshold.

A histogram of the number of scattered parent trajectories per detected event (i.e., different Cherenkov cones) is shown in figure 4.5. Independent of the crystal size, about 30% of the detected events generated three Cherenkov cones, 70% between two and four and over 90% from one to five. In average, a single Cherenkov cone was produced in approximately 10% of the cases.

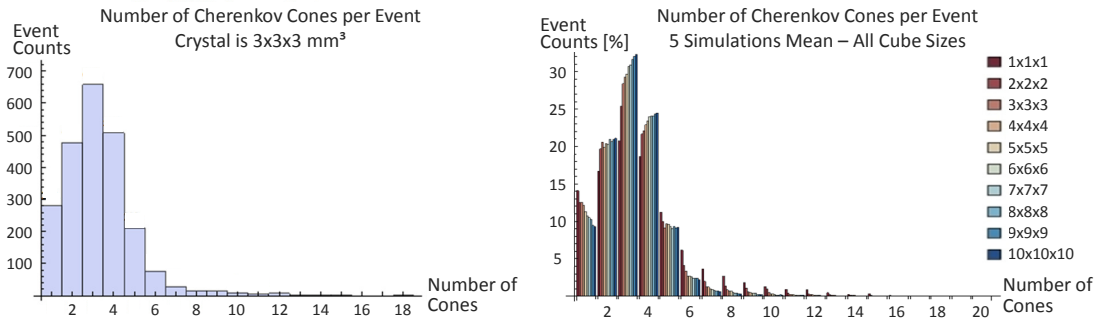

Figure 4.5: Left: Number of different Cherenkov Cones per detected event for a $3 \times 3 \times 3$ mm^3 CHERENCUBE. For further dimensions, see appendix B, figure B.2. Right: 5-simulations-mean for every CHERENCUBE size.

The orientation in which the electron is ejected from the atom is completely independent of the incoming direction of the gamma-ray, leading to an isotropic emission of Cherenkov cones inside the CHERENCUBE.[1] Figure 4.6 shows the uniform distribution of all detected photons over the 6 photodetectors, averaged over the 5 independent simulations for each crystal size.

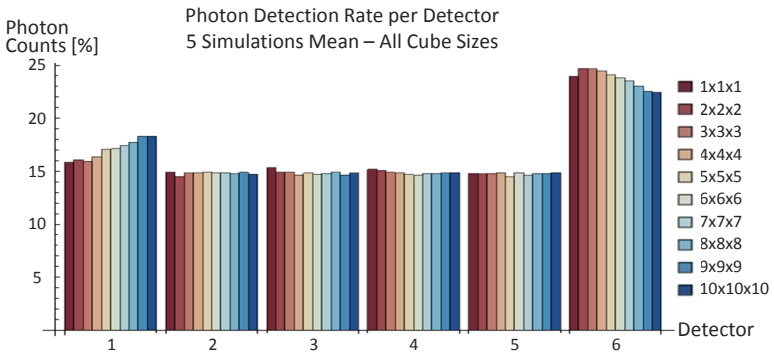

Figure 4.6: Photon detection rate per detector for all crystal sizes averaged over the 5 independent simulations. Higher rates in detector 1 (gamma entry) and 6 (opposite face) are due to the simulated setup.

Because of the fixed relative positions in the simulated setup, most of the cones originate along the central axis of the cube. Due to the isotropic cone orientation, the photodetectors located equally distant from the central axis (detectors 2 to 5) show a constant photon detection rate. Only the detector in the gamma-

[1]Due to the short electron range until its complete energy deposition, its direction is not influenced by including a uniform strong magnetic field of 7 Tesla to the simulation, making it impossible to previously estimate the cone's orientation.

impinging face (detector 1) and that on the opposite side (detector 6) detect a higher number of photons. This is due to both the 511 keV photons interacting with the crystal in their vicinity as well as the cone-like emission of the optical photons.

4.4.2 Energy and Cherenkov Angle

In figure 4.7, a histogram of the initial kinetic energy of the electrons producing the first Cherenkov cone per detected event (i.e., before any loss of energy) is presented, discriminating between those electrons generated by Compton scattering or photoelectric effect. For the latter, two energy peaks are clearly recognizable. Their values, $E_1 = 422.99$ keV and $E_2 = 441.47$ keV, correspond to the deposited gamma-ray energy (511 keV) minus the energy of the two characteristic x-ray emissions of $PbWO_4$.

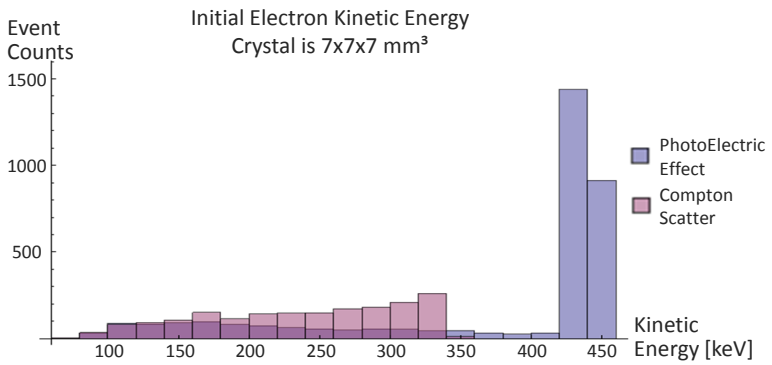

Figure 4.7: Initial kinetic energy of the photoelectric and Compton generated electrons producing the first Cherenkov cone per detected event. The two photoelectric energy peaks, $E_1 = 422.99$ keV and $E_2 = 441.47$ keV, correspond to the deposited gamma-ray energy (511 keV) minus the energy of the two characteristic x-ray emissions of PWO. For further cube dimensions besides the shown one, see appendix B, figure B.3.

The total energy of an electron corresponds to the sum of its kinetic energy and its rest mass (511 keV). From equation 4.3, the threshold total energy E_{th} a recoil electron needs to generate Cherenkov photons can be calculated. The Cherenkov angles $\theta^{CKOV}_{E_{1,2}}$ for the two PWO main energy peaks (E_1 and E_2) are obtained by means of equation 4.4. The resulting values are shown in table 4.3. Since the refractive index n varies through the simulated wavelength range, calculated E_{th} values for the minimum, mean and maximum n are presented.

Refractive Index n	E_{th}^{Total}	$E_{th}^{Kinetic}$	$\theta_{E_1}^{CKOV}$	$\theta_{E_2}^{CKOV}$
2.17	575.8 keV	64.8 keV	56.6°	56.9°
2.26	569.8 keV	58.8 keV	58.1°	58.4°
2.52	556.7 keV	45.7 keV	61.7°	61.9°

Table 4.3: Calculated values of the threshold energy (E_{th}) and Cherenkov angle (θ^{CKOV}) for the two main energy peaks of photoelectric generated electrons. The mean refractive index over the simulated range is $n = 2.26$. The difference between total and kinetic energy corresponds to the electron's rest mass (511 keV).

4.4.3 Path Lengths and Detection Distances

As depicted in figure 4.1, Cherenkov photons are not all emitted from the same point along the electron's path but at randomly distributed distances e_i. The histogram in figure 4.8 (left) shows these distances between the origin of each electron's trajectory and the point of emission of its related photons for a $10 \times 10 \times 10$ mm^3 CHERENCUBE.

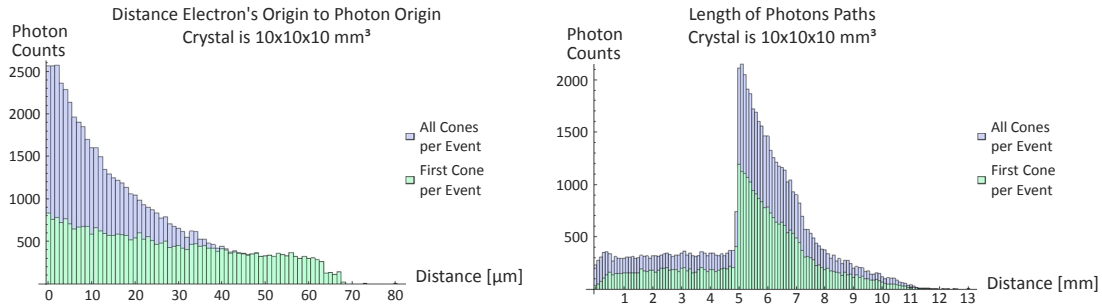

Figure 4.8: Distance histograms for a $10 \times 10 \times 10$ mm^3 CHERENCUBE for all cones as well as the first cone per event. For further dimensions, see appendix B, figures B.4 and B.5. Left) Distance between the origin of each electron's trajectory and the point of emission of its related Cherenkov photons. The maximum distance is of the order of 70 μm, regardless of the crystal size. Right) Length of each Cherenkov photon's path from generation until detection. The sharp rise at 5 mm, half the cube's size, is due to the simulated scenario and the short electron range.

In the case of the first cone emitted per event, i.e. before the electron's trajectory is modified, the electron's origin represents the point of interaction of the impinging gamma-ray with the radiator. Regardless of the crystal size, for all simulated configurations the maximum distance e_i is in the order of 70 μm, which is determined by the maximum distance the electron can travel before its complete energy deposition. This range, in turn, is defined by the particle's energy and the

radiator's material properties. Before any scatter, the electron has higher energy and is therefore more likely to prolong its trajectory. This is reflected in the fact that all photons being emitted further away (in the histogram, above 0.045 mm) belong to the first cone per event.

From their emission point, optical photons travel until detection upon their arrival at one of the cube's faces. The length of each photon path for all cones as well as for the first cone per event can be seen in the right histogram of figure 4.8. Due to the simulated scenario (gamma-ray entering the cube perpendicularly and centered) and the comparatively short electron range before its complete energy deposition, 511 keV photons depositing energy before being scattered generate Cherenkov cones with their apex close to the central cube's axis. The flight path of the Cherenkov photons until detection is then, at least, half of the cube's length, causing the sharp rise depicted in the histogram.

Since most photon paths are longer for larger crystal sizes, the resulting projected pattern is consequently wider due to the increased distances between photons upon detection. This parameter is related to the spatial resolution to be provided by the photodetector to allow individual identification of each photon and, with it, of the projected Cherenkov cones. Figure 4.9 (left) shows a histogram of the distance between every photon and the nearest detected photon for a $2\times2\times2$ mm^3 and a $9\times9\times9$ mm^3 CHERENCUBE, considering all photons from all Cherenkov cones belonging to the same event.

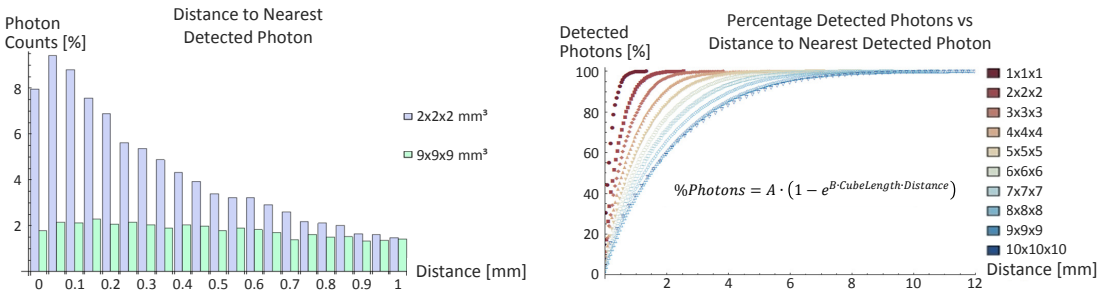

Figure 4.9: Distance upon detection between each photon and the nearest detected photon belonging to the same event. Left) Comparison between a small ($2 \times 2 \times 2$ mm^3) and a large ($9 \times 9 \times 9$ mm^3) CHERENCUBE. For better visualization, only distances shorter than 1mm are shown. The counts at zero distance represent those events with only one detected Cherenkov-Photon. Right) Cumulative percentage of photons with their closest neighbor within a certain distance. The exponential behavior is directly related to the cube length.

For smaller cube sizes, the percentage of near detected photons located at

shorter distances is higher. The cumulative percentage of photons having its closest neighbor within a certain distance is presented in the plot on the right of figure 4.9, showing an exponential behavior that is directly related to the cube length. For every simulated crystal size, 20 percent of the detected photons have their closest same-event detected photon within a distance of approx. 5 percent of the cube's length (e.g., 50 μm distance for a $1 \times 1 \times 1$ mm^3 cube). Based on this, a pixelated photodetector with grid size bigger than 50 μm in a $1 \times 1 \times 1$ mm^3 CHERENCUBE will not be able to individually recognize 20% of the photons, thus reducing the probability to identify the projection of each related Cherenkov cone.

4.4.4 Detection Time

The absolute detection time t_i of the i_{th} Cherenkov photon is defined as the time elapsed between t_0, i.e. the trigger of the gamma-ray at 10 mm from the cube face, and the time of arrival at the photodetector (see figure 4.1). For every crystal size, the histogram of the absolute detection times t_i of all photons presents the same distribution as that shown for the photon path lengths in figure 4.8 (right), with an offset (due to the gamma-ray time-of-flight until interaction in the crystal) and slightly blurred due to the different propagation velocities of the 511 keV photon (c) and the Cherenkov photons (c/n). These histograms for all simulated CHERENCUBE sizes are shown in appendix B, figure B.6. In figure 4.10, an example of the absolute detection time t_i of every photon belonging to one single detected event is presented.

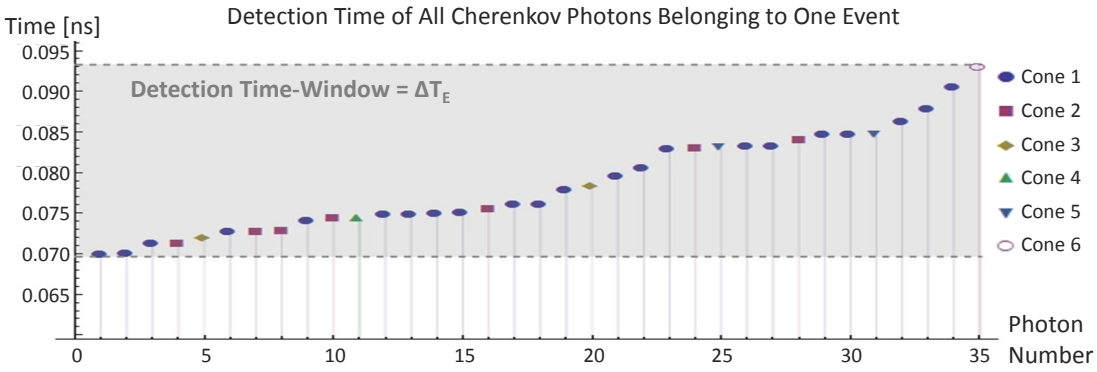

Figure 4.10: Example of absolute detection times t_i for all photons belonging to one detected event, showing the definition of the detection time-window ΔT_E. Photons belonging to different Cherenkov Cones are not detected sequentially but randomly interlaced.

The photons in figure 4.10 are ordered based on their detection time, showing that those belonging to different Cherenkov cones are not sequentially detected, but randomly interlaced due to the differing orientation and origin point of their emission. Hence, even with an infinite time resolution, it is not possible to associate a detected photon to an individual cone based solely on timing.

The detection time window between the first and the last same-event photon, defined as ΔT_E, is characterized for all the simulated cube sizes in the cumulative histogram in figure 4.11. It shows that the possible values of this parameter are restricted to a limited range, which is narrower for smaller crystals. For a $1 \times 1 \times 1$ mm^3 CHERENCUBE, all photons belonging to the same event are detected within a window $\Delta T_E \leq 30$ ps, while for a $10 \times 10 \times 10$ mm^3 radiator the window is $\Delta T_E \leq 150$ ps. The event counts for the different curves in the histogram don't start from zero due to the number of events with only one detected Cherenkov Photon (i.e., $\Delta T_E = 0$ ps).

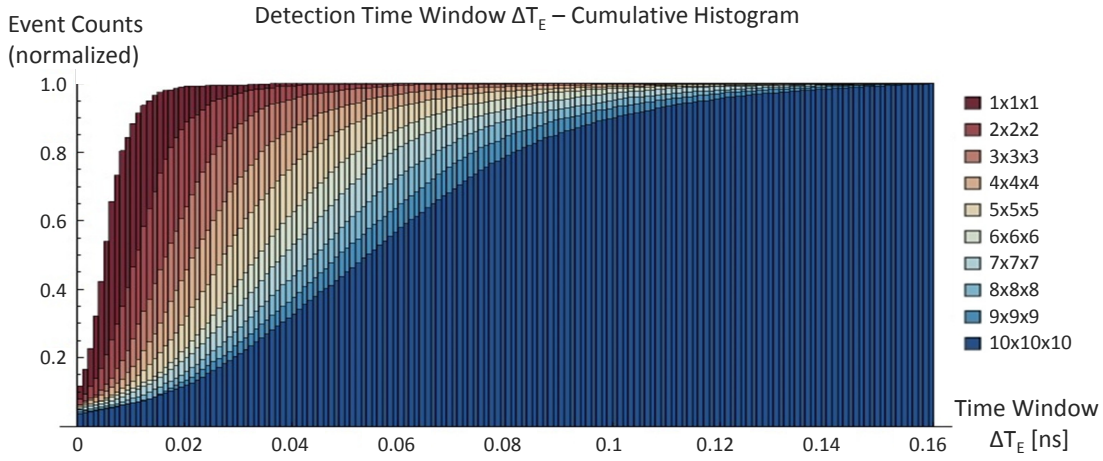

Figure 4.11: Cumulative histogram of detection time windows ΔT_E for all crystal sizes. Same-event photons are detected within a narrower window for smaller radiator cubes.

4.5 Discussion

The proposed detection concept, the CHERENCUBE, relies strongly on its potential ability to detect the Cherenkov photons and associate them to a single 511 keV gamma-ray. In order to achieve this, a detector with high photodetection efficiency is needed. The structure of the detector's sensitive surface should

be a two dimensional array of micro-cells, each of them being able to provide its individual coordinates and time-stamp when a photon is detected. Based on the presented simulation results, it is possible to analyze these requirements as well as further constraints that the main components of the detector block, the photodetector and the Cherenkov radiator, have to fulfill.

4.5.1 Detection Time

The individual detection time of every Cherenkov photon is a crucial parameter to assess their common emission. As shown in section 4.4.4, all photons belonging to the same interacting gamma-ray are detected within a time window ΔT_E whose width depends on the crystal size. For the simulated setup geometry, bigger cubic radiators have a larger ΔT_E value. However, same-event photons coming from different Cherenkov cones are detected randomly interlaced during this window. Even with an infinite time resolution, it is impossible to assign them to an individual cone according to their individual detection time. Based on this, the candidate photodetector would have to be able to provide individual time stamps for every detected photon, with an intrinsic time resolution less than or equal to ΔT_E. Assuming no event pile-up, i.e. no overlap between detection windows from different impinging gamma-rays, all photons with the same time-stamp could then be associated to a single detected event.

In an ideal scenario, every detector's micro-cell would include a time-stamp generator. However, due to the reduced number of photons in this particular application, the timing circuitry could be shared between several cells that are unlikely to be triggered simultaneously, i.e. during the same detection window, thus reducing the complexity of the sensor. As shown in figure 4.2, multiple photodetectors are involved in the detection of Cherenkov photons belonging to the same event, requiring for the time-stamp generation to be synchronized among the six CHERENCUBE sensors. Intrinsic photodetector properties like dark-count-rate (DCR) or afterpulses should have temporal components that are negligible compared to ΔT_E. A DCR generated photon signal within ΔT_E would alter the photon count associated to that event, while afterpulses might modify the time window itself or disturb the photon count of a different event detected later on.

4.5.2 Detection Coordinates

The recognition of a projected Cherenkov cone is only possible if the spatial distribution of the corresponding photons upon detection is known. To achieve this, a photodetector with a highly pixelated sensitive surface is needed, with the ability to provide the position coordinates of each detected photon. The pixelated design should also maximize the fill factor, reducing the non-sensitive areas between cells and optimizing thus the photodetection efficiency. Assuming no blind areas in the micro-cell array (i.e. 100% fill factor) the grid size and the cell size are equal. The histograms in figure 4.9 show that the required grid size, related to the minimum detection distance between two same-event photons, is determined by both the size of the Cherenkov radiator as well as the number of photons to be sensed individually. For smaller crystals, the photon travel paths are shorter and the projected pattern is constituted by detection coordinates that are closer to each other. Consequently, smaller micro-cells are needed to detect all photons individually. At larger crystal sizes, it is more likely to recognize all photons individually due to the wider photon pattern projection, lowering the impact of the micro-cell size. Table 4.4 summarizes the percentage of same-event photons that would not be able to be individually detected for three different micro-cell sizes of 25, 50 and 100 μm.

Cell Size [μm]	Cube Length [mm]									
	1	**2**	**3**	**4**	**5**	**6**	**7**	**8**	**9**	**10**
25	12.6	5.8	3.8	2.9	2.2	1.8	1.6	1.3	1.2	1.1
50	23.5	11.3	7.5	5.6	4.4	3.7	3.1	2.7	2.3	2.3
100	41.5	21.2	14.5	10.9	8.6	7.2	6.1	5.3	4.6	4.5

Table 4.4: Percentage of non-individually detected same-event Cherenkov photons for cell sizes of 25, 50 and 100 μm. Values are obtained from figure 4.9 (right).

In the smallest case of a $1 \times 1 \times 1$ mm^3 CHERENCUBE, over 20% of the photons are detected closer than 50 μm. A micro-cell size larger than this would imply losing even more photon counts, which on turn has a bigger impact on the detection efficiency of the proposed concept, as shown in figure 4.4. These values, however, are strongly influenced by the simulated setup geometry, due to most of the cones originating next to the central axis of the cube. In a PET-like ring arrangement of sensors, the impinging gamma-rays would also interact closer to the sides of the cubic radiator, leading to shorter photon paths and,

with it, to shorter distances between detected photons. Therefore, the candidate CHERENCUBE photodetector would depend on the smallest possible micro-cell size for allowing the aimed individual photon recognition. The detector's dark-count-rate should also be reduced to a minimum, since dark-count-generated photons with an event-compatible time stamp would alter the recognition of the projected pattern.

4.5.3 Energy Threshold

Compared to traditional scintillation detection schemes, the Cherenkov-only proposed concept relies on the detection of very few optical photons, whose amount is not directly related to the energy deposited by the gamma-ray in the crystal. For its implementation in a PET scanner, this implies that scattered events (e.g. in the patient, see section 2.4.3) can't be recognized by these means.

Nonetheless, the lower threshold energy for Cherenkov photons generation is determined exclusively by the radiator's refractive index (see equation 4.3), being for the simulated system of the order of 40 - 70 keV (see table 4.3). By lowering the refractive index of the candidate radiator, this threshold could be raised towards the desired energy cut. As seen in figure 4.7, the maximum energy a recoil electron can get from a photoelectric effect interaction of a 511-keV quantum is well-defined by the emission of the material's characteristic x-rays. In the simplifying assumption that the refractive index could be changed without modifying further material properties, adjusting it to a value of $n = 1.202$ would imply a lower energy threshold of 410 keV, hence applying an intrinsic rejection of scattered gamma-rays comparable to that of clinical PET scanners (see section 2.4.3). However, under the same assumption and based on equation 4.2, lowering the refractive index results in a lower number of generated photons. This, following the results on figure 4.4, imposes a trade-off between a higher energy cut and detection efficiency. On the other hand, a higher refraction index sets a less restrictive threshold for Cherenkov photons generation and, therefore, an increased energy-based acceptance of PET events.

4.5.4 Depth of Interaction

As explained in section 2.4.4, the identification of the depth of interaction (DOI) of the gamma-ray in the crystal is one key parameter to improve the spatial resolution of PET scanners. The proposed detection concept uses the geometrical

distribution of the emitted Cherenkov photons to obtain the three dimensional DOI coordinates for each detected event.

As shown in figure 4.1, knowing the Cherenkov angle and the cone radius, the position of the cone apex can be calculated. This point differs from the gamma energy deposition due to the different photon emission points along the electron's trajectory. However, these values are in the range of a few tens of micrometers, thus negligible compared to the crystal size and the length of the optical photon paths (see figure 4.8). As a result, the cone apex can be assumed to be one point and the different projected radii for the same cone can be considered to be equal.

The uncertainty of the DOI determination is then defined by the accuracy of the fit to the detected photon pattern to obtain the radius and by the range of possible angle values. For example, a 10% inaccuracy in these two parameters (radius and angle) can have an impact of up to 40% in the geometrical DOI determination. This error is more relevant for detected cones with larger radii and, therefore, for larger crystals due to the wider projected photon pattern. For the biggest simulated crystal size, assuming a cone with radius equal to the cube length (r = 10 mm) and the maximum Cherenkov angle (see table 4.3), the 10% inaccuracy in both parameters induces a DOI error of 2.1 mm. This is comparable to current three dimensional DOI approaches based on scintillation light detection (51)(68) and can be further improved by means of more precise radius and angle values. The latter depends on the refractive index and the electron's energy (see equation 4.4), being 0° at the threshold energy and around 60° for direct photoelectric interactions, i.e. with the maximum energy (see table 4.3). Therefore, adjusting the refractive index of the radiator to accept only high-energetic interactions also reduces the Cherenkov angle range and improves the DOI precision. On the other hand, the histogram in figure 4.7 depicts the higher frequency with which photoelectric events generate Cherenkov cones compared to low-energy interactions. Consequently, a crystal with a higher photoeffect-to-compton probability would statistically diminish the error of directly including only the maximum Cherenkov angle in the DOI calculation.

The DOI recognition procedure relies on the ability to discriminate between multiple Cherenkov cones originating by one impinging gamma-ray and the posterior scatter of the recoil electron in the material. This phenomenon happens in over 90% of the interactions (see figure 4.5). The apex of the first emitted cone is the closest to the interaction point. Nevertheless, because of the short electron range until its complete energy deposition, the origins of the following cones are still located within very short distances. Therefore, recognizing at least one cone

per event is sufficient for a negligible error in the DOI determination. This is no longer true for gamma-rays being scattered and absorbed (or multi-scattered) inside the crystal, where the different cones might be emitted at considerable distances. Without multiple-cones recognition, no radius can be obtained from the detection coordinates and no DOI estimation is possible.

4.6 Conclusion

The theory of a new concept for a Cherenkov-only PET detector block has been introduced and thoroughly analyzed by means of Monte Carlo simulations. The discussed results show that the 6-sided readout design of the CHERENCUBE is needed in order to improve detection efficiency and take advantage of the well-defined geometrical and fast temporal properties of Cherenkov radiation for a PET system. To achieve this, the candidate photodetector needs to provide several characteristics. First, due to the low number of generated optical photons compared to traditional scintillation PET setups, it needs to have very high photodetection efficiency with single-photon-measurement ability. Every missed Cherenkov photon reduces the detection efficiency of the proposed concept considerably. Furthermore, all detected photons need to be registered with an individual time-stamp, with an intrinsic time resolution in the range of a few tens of picoseconds. By these means, all photons with a common detection time value (i.e. within a setup-defined time window) could be associated to the same impinging gamma-ray. Additionally, the position of each detector's micro-cell hit by a photon needs to be provided as well, since detection coordinates are the only possibility to discriminate among same-event multiple Cherenkov cones. The micro-cell grid size and layout, on its turn, defines the ability to distinguish individual photons reaching the detector closely together, further influencing the detection efficiency.

Ongoing photodetector developments are already aiming towards highly pixelated sensors featuring these characteristics (116)(86). These approaches, however, are either still prototype concepts or focus on providing only multiple time-stamps per pixel, without the position information per fired micro-cell. On the other hand, currently available position-sensitive photodetectors detecting either the center of gravity of a group of fired cells (i.e., not individual coordinates as required) (117)(118) or providing multiple signals per sensor (119) have an intrinsic spatial resolution in the range of several hundreds of micrometers. Thus, the implementation of the introduced detection concept depends on further pho-

todetector developments.

The procedure for DOI recognition using the conical Cherenkov geometry relies on the photon time stamps (group photons to one event), detection coordinates (obtain projected photon-pattern) and the crystal's refractive index. This parameter defines the energy threshold for Cherenkov photon generation and its emission angle. With a proper material selection, an intrinsic energy cut to reject low energy incoming gamma quanta (e.g. previously scattered in a patient) can be achieved. High-energy photons being scattered in a small angle would still be considered within this energy acceptance window. However, gamma-rays being Compton-scattered in the crystal would be discarded as well, reducing the sensitivity. A narrower energy acceptance window also restricts the possible Cherenkov angle values, consequently increasing the accuracy of the DOI recognition algorithm. Its precision is also improved by a crystal with a high photoeffect-to-compton probability. The implemented radiator should have a high stopping power at 511 keV as well, to increase the interaction probability of the gamma-rays, and good light transmission at the Cherenkov photons wavelength (mostly blue - near UV), to avoid losing detection efficiency because of optical absorption.

With an accurate cone radius estimation, the three dimensional DOI recognition allows to improve the sensitivity by means of larger crystals (higher interaction probability) without worsening the spatial resolution. However, the probability of event pile-up at higher detection rates increases with larger crystal sizes, affecting the proposed time-window-based event classification. Therefore, an application-based compromise between spatial resolution, detection efficiency and sensitivity is needed to achieve an optimized detector's design.

The analyzed results regarding timing and spatial distribution of the detected Cherenkov photons are strongly influenced by the simulated setup geometry. Therefore, in order to gain a deeper understanding of the benefits and limitations of the proposed concept, the simulations should be extended to a complete PET-like ring arrangement with non-scintillating crystal materials like lead fluoride (PbF_2) or lead glass. To configure a more realistic scenario, the simulations should also include distributed sources and image reconstruction, aiming for a proper quantification and assessment of the potential impact of Cherenkov radiation in TOF-PET.

5

Summary and Outlook

The work presented in this thesis consisted of two different approaches towards reaching high resolution in PET imaging.

The first one was a thorough performance analysis of newly developed photodetectors, namely *digital silicon photomultipliers* (digital SiPMs). The investigation included two different scintillators, a standard one used in current PET systems (LYSO) and a recently developed one with a very high light yield (GAGG). Both kinds of crystals had dimensions of $2 \times 2 \times 6$ mm^3 and were optically coupled one-to-one to the center of one detector's pixel, an arrangement found in scanners with high image resolution. The effects on the sensor's performance resulting from variations in five different operational parameters were studied, aiming to define an optimum configuration for its implementation in a PET system. The experiments were carried out in a laboratory-bench setup through measurements of single and coincidence events of a ^{22}Na point source.

The results achieved showed that the analyzed photodetectors have a similar performance in terms of time and energy resolution compared to state-of-the-art analog SiPMs. For LYSO and GAGG, respectively, coincidence time resolution (CTR) values of less than 180 ps and 460 ps (FWHM) were achieved, while the average energy resolution after applying saturation correction was around 13.5% and 12.9% (FWHM). The main differences between the analog and digital approaches arise due to the logic of the implemented acquisition sequence. Under operating conditions producing high dark-count-rates (DCR), wrongly validated events induce dead-time that can greatly affect the system's sensitivity. With a less restrictive combination of acquisition thresholds, these false-positive events can account for up to 100% of the sensor's active time. This ratio can be considerably improved to less than 10% by raising the thresholds. However, the most

effective solution is to reduce the sensor's DCR by cooling it to, at least, temperatures around 0°C. A lower DCR allows a lower cell inhibition of the sensor, improving the photodetection efficiency and consequently the CTR.

For a potential integration into large scale scanners, the demand for an incorporated cooling system represents a trade-off to the advantage offered by the highly integrated electronics. Improved versions of the analyzed devices as well as alternative approaches currently being developed might help to overcome these limitations, suggesting an auspicious future in PET for this kind of photodetectors.

The second investigated approach was a novel definition of a PET detector. Instead of converting the impinging gamma-rays into measurable scintillation light, the proposed idea relies exclusively on another light generation mechanism known as *Cherenkov radiation*. The advantages compared to scintillation are the prompt emission of photons and a well-defined conical orientation, while the main drawback is the very low number of generated optical photons. To fully benefit from the Cherenkov characteristics, the new detection concept modifies the common single-sided readout of scintillation-based detectors into a six-sided readout of a cubic crystal. By this means, not only the photon detection time is minimized, but also the origin of each cone could be precisely determined, resulting in a PET detector suitable for time-of-flight acquisitions and three-dimensional depth-of-interaction (DOI) recognition. Due to the material-related energy threshold for Cherenkov light generation, a proper radiator election could lead to an intrinsic rejection of previously scattered gamma-rays.

Ten different cube dimensions of the new concept were analyzed through Monte Carlo simulations of a single detector being hit by a 511 keV photon. The results showed that for a single gamma-ray, multiple Cherenkov cones were generated. In order to group them into a common event, individual time-stamps for every optical photon are needed. The width of the time window in which all same-event photons are detected is dependent on the size of the radiator, being 30 ps for the smaller configuration ($1 \times 1 \times 1$ mm^3) and 150 ps for the larger one ($10 \times 10 \times 10$ mm^3). To discriminate between different cones and achieve the proposed DOI recognition, the individual detection coordinates of each photon are necessary. Therefore, a suitable photodetector should be a two dimensional array of densely positioned sensitive micro-cells. The size of these cells directly affects the number of individually detected photons and, consequently, the accuracy of the DOI recognition as well as the detection efficiency.

Smaller crystals result in a tighter detected pattern of photons, imposing smaller detector micro-cells for the needed individual photon recognition. The detection efficiency is reduced as well, due to the lower interaction probability of the gamma-ray in a smaller volume. Due to the three-dimensional DOI ability, the size of the crystal doesn't limit the achievable resolution as compared to traditional scintillation-based PET setups. For these reasons, a larger crystal is better suited for a higher detection efficiency and sensitivity, as well as requiring less spatial resolution from the photon detection coordinates. However, at higher activity rates, possible pile-up of gamma-rays interacting in the same crystal could ruin the cone recognition and hereby the DOI algorithm. Similar to standard scintillator block detectors in PET, this results in a practical limitation of the amount of activity inside the system's field of view. Therefore, a balance needs to be found between the activity rate of a particular application and the size of the cubic radiator.

The main limitation of the proposed concept is the very low number of generated photons, up to a maximum of a few tens. Currently, no photodetectors are able to reliably measure this low light intensity and at the same time provide individual time and position stamps upon detection. A possible practical implementation thus depends on further progress in this area, with ongoing developments already aiming towards sensors featuring some of these characteristics.

For the two analyzed approaches, the presented results are strongly dependent on the characteristics of the experimental or simulated setups. Therefore, future work should consider expanding the scope of the investigation to scenarios representing more closely the final application.

In the case of the digital SiPMs, the analysis to find the optimum parameter configuration is application dependent. For an investigation in a PET-similar architecture, the used crystal should completely cover the pixel's sensitive area and all the sensor channels should be occupied and activated. The total activity distribution and intensity should be consistent with real PET examinations, for a proper assessment of the impact of the sensor's dead time on the system's sensitivity.

Similar steps should be followed for further understanding of the novel detection concept based solely on Cherenkov radiation. Initially, the simulations should be expanded to a back-to-back configuration of two detector blocks including the photodetector properties. This study, analogous to that presented with the digital SiPMs, should provide an evaluation of the performance limits in

terms of CTR. Finally, an expansion to a ring arrangement should be investigated. By means of distributed sources including image reconstruction techniques, the final goal would be an evaluation of the potential improvements in image quality introduced by the intrinsic energy-based rejection of scattered gamma-rays, the three-dimensional DOI recognition and the time-of-flight (TOF) ability.

The latest scintillation-based TOF-PET scanners have a CTR around 350 ps, i.e. an accuracy of about 5 cm to recognize the origin of the annihilation gamma-rays. A system based on the proposed Cherenkov detector might provide a highly improved timing performance that, in case of reaching CTR values better than 30 ps (4.5 mm), would potentially eliminate the need for image reconstruction techniques, allowing thus the achievement of unprecedented image resolution in positron emission tomography.

Appendix A

Measurement Results with Digital SiPMs

DCR vs Overvoltage

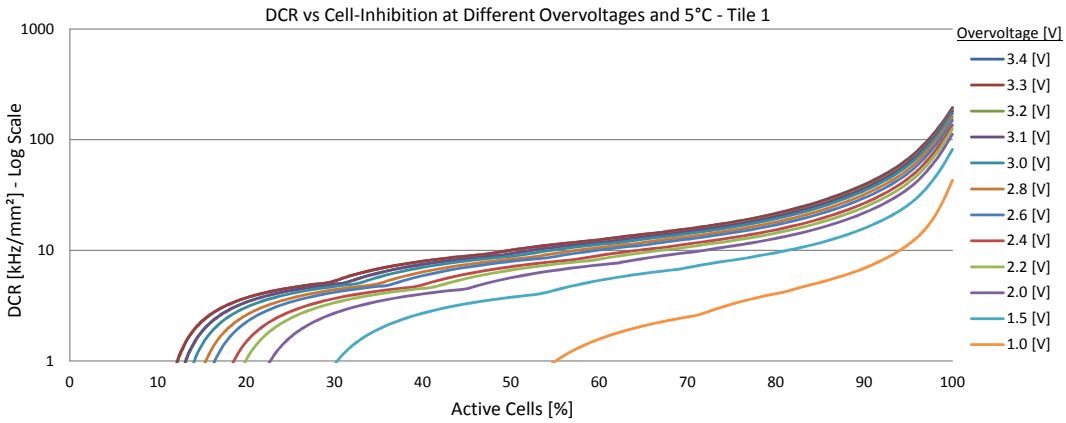

Figure A.1: DCR vs active cells at different overvoltages at constant 5°C.

DCR Coefficient per Overvoltage

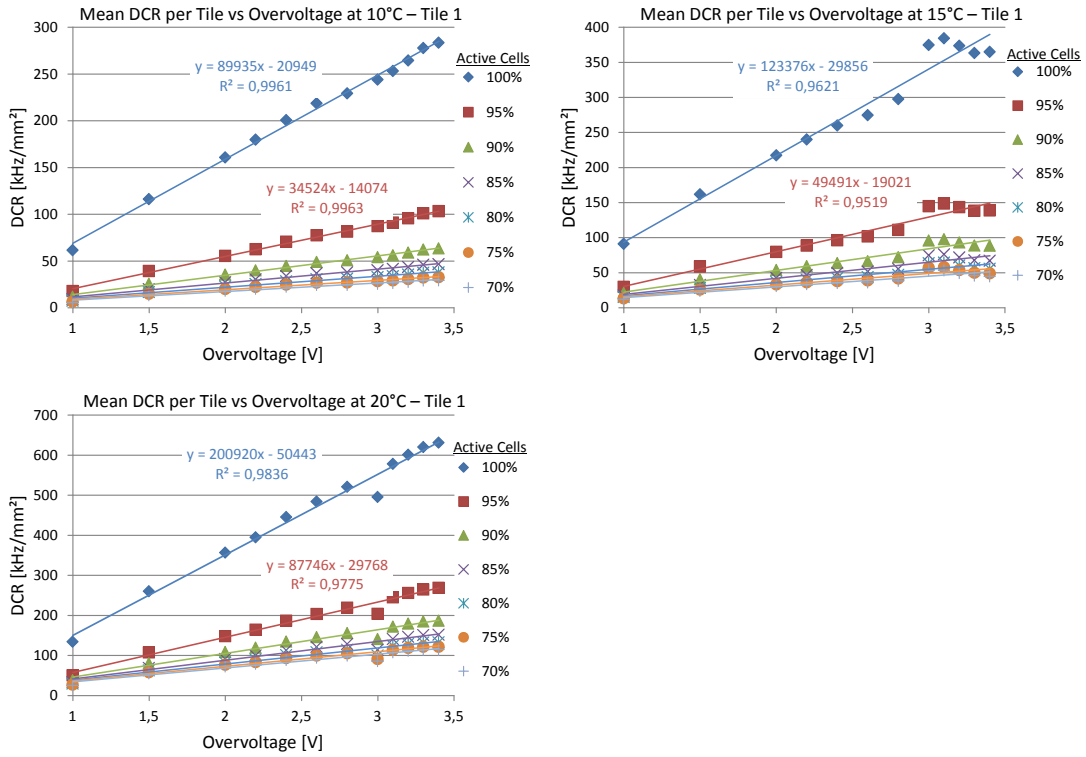

Figure A.2: Linear increase of DCR with overvoltage at constant 10°C, 15°C and 20°C and different cell inhibitions. The slope of each linear trend corresponds to the DCR coefficient per voltage. For better visualization, only the two first parameters of the linear trends are shown.

CTR vs Cell Inhibition

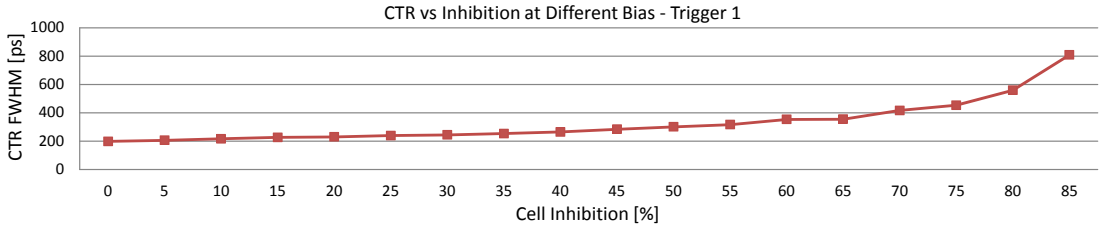

Figure A.3: CTR against cell inhibition up to 85% for LYSO using trigger scheme 1. At higher inhibition percentages, CTR decreases exponentially.

Energy Resolution vs Trigger and Validation Schemes

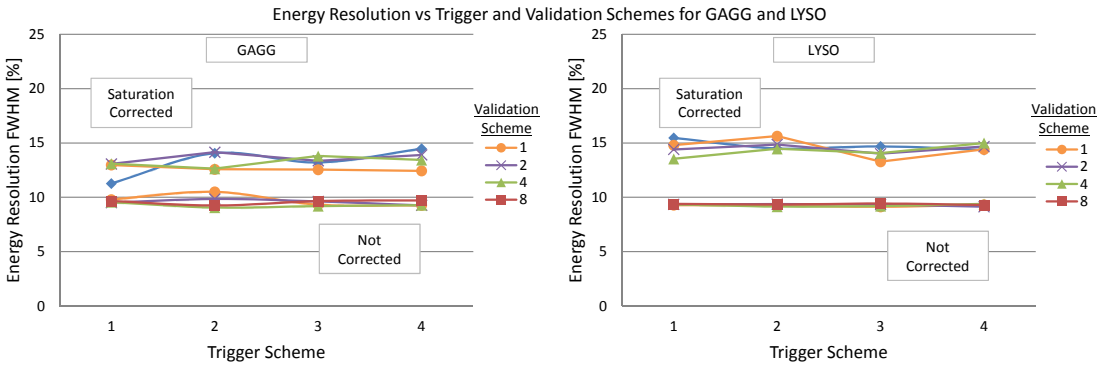

Figure A.4: Singles energy resolution (% FWHM) versus trigger and validation schemes at overvoltage 3.0 V and 5.6°C for GAGG (left) and LYSO (right). Energy resolution is not affected by changing both schemes. Fluctuations around the linear trend are due to the fitting procedure and the approximations of the applied saturation correction (see section 3.2.2).

Energy Resolution vs Temperature

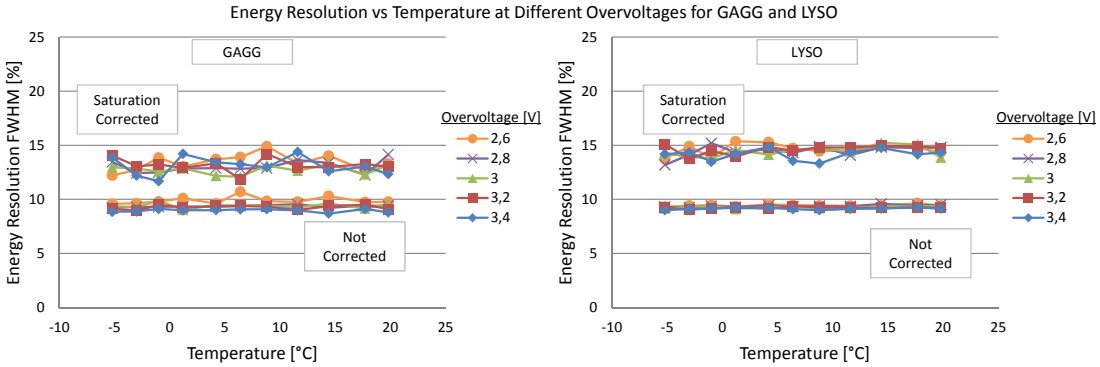

Figure A.5: Singles energy resolution (% FWHM) versus temperature at different overvoltages for GAGG (left) and LYSO (right). Energy resolution is not affected by changes in temperature between -5°C and 20°C. Fluctuations around the linear trend are due to the fitting procedure and the approximations of the applied saturation correction (see section 3.2.2).

^{22}Na LYSO Energy Spectra at Different Overvoltages

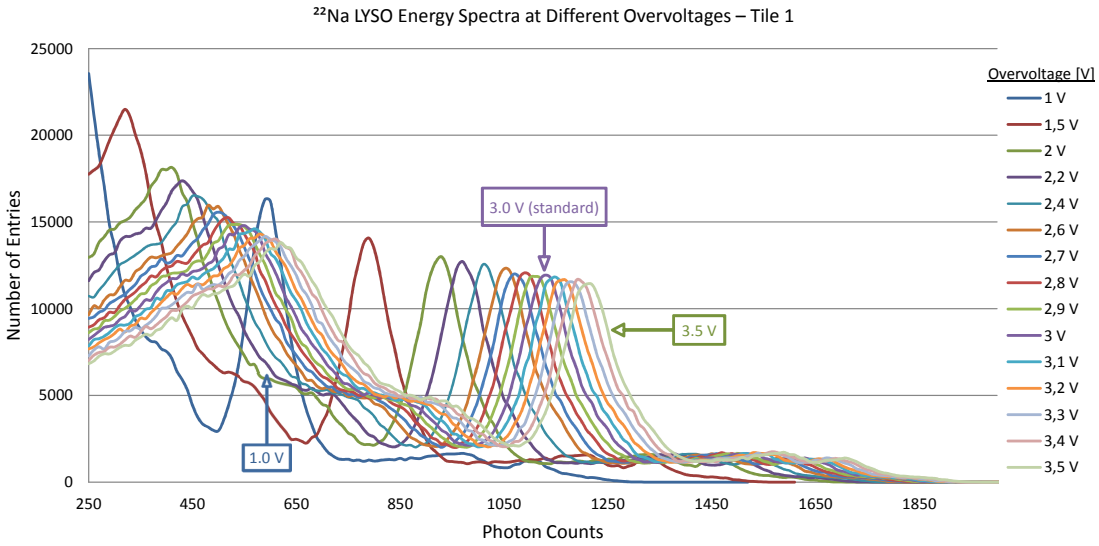

Figure A.6: ^{22}Na singles energy spectra for LYSO applying different overvoltages (not corrected for saturation). At higher voltages, the 511 keV photopeak is located at a higher value of photon counts, due to the increased photodetection efficiency, and the peak's amplitude in the histogram is reduced.

Duty-Cycle vs Cell Inhibition

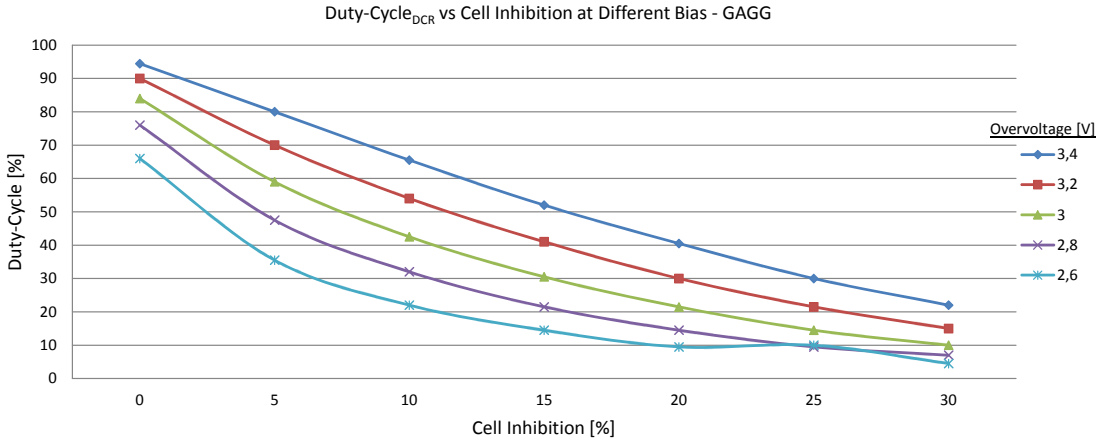

Figure A.7: Duty-cycle versus cell inhibition for different overvoltages for GAGG. The values are the average between both pixels.

Duty-Cycle vs Temperature

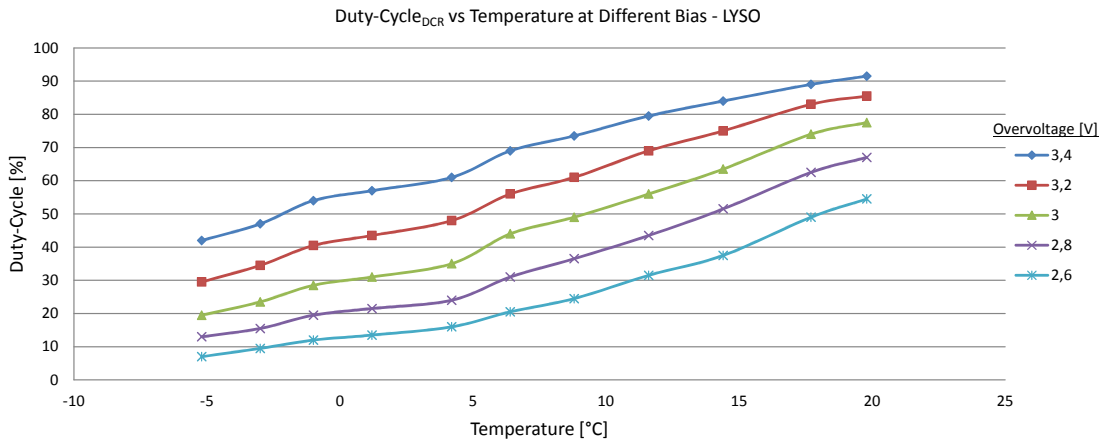

Figure A.8: Duty-cycle versus tile temperature for different overvoltages for LYSO. The values are the average between both pixels.

Duty-Cycle vs Validation and Trigger Schemes

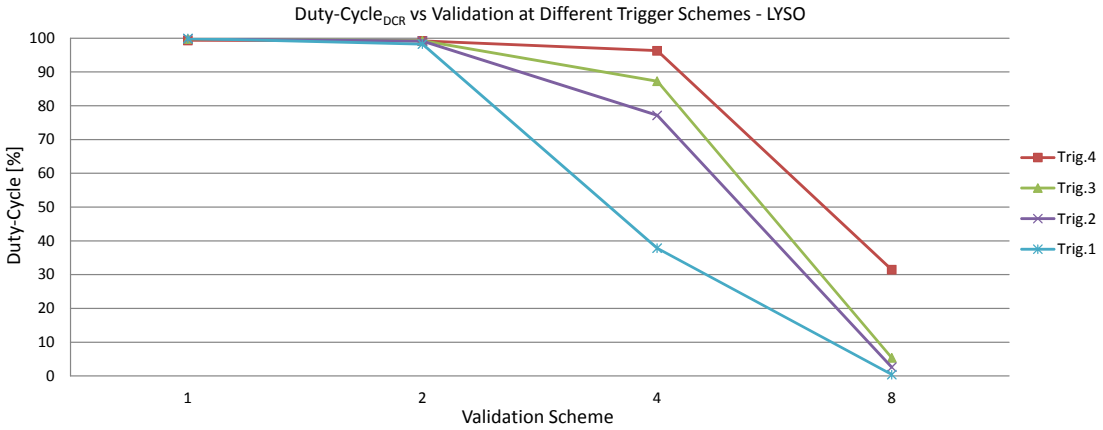

Figure A.9: Duty-Cycle versus validation and trigger schemes for LYSO. The values are the average between both pixels.

Appendix B

Simulation Results of a Cherenkov-Based Detector Block for PET

Detection efficiency vs Photon Threshold

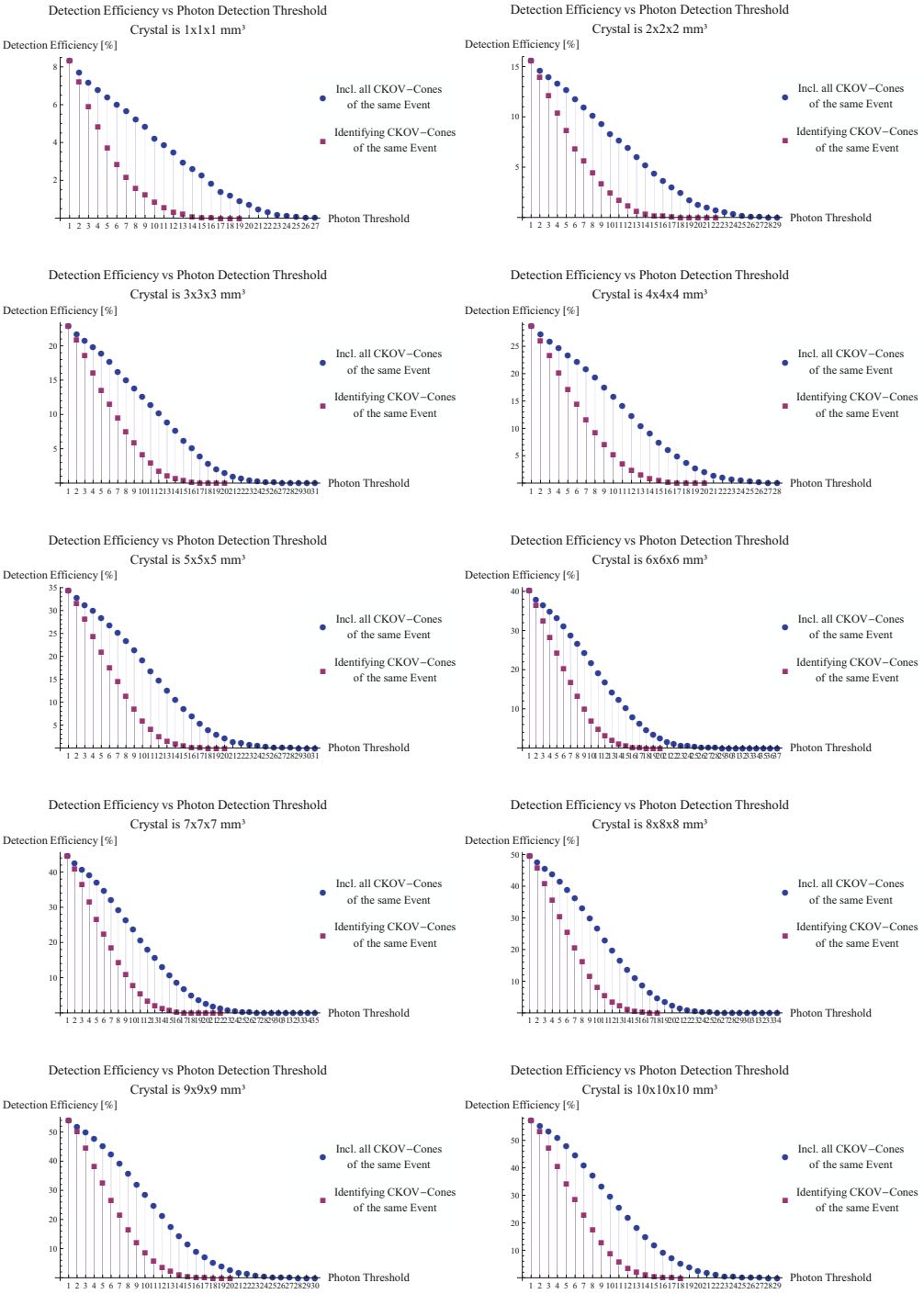

Figure B.1: Detection efficiency vs photon threshold for all CHERENCUBE sizes.

Number of Different Cherenkov Cones per Detected Event

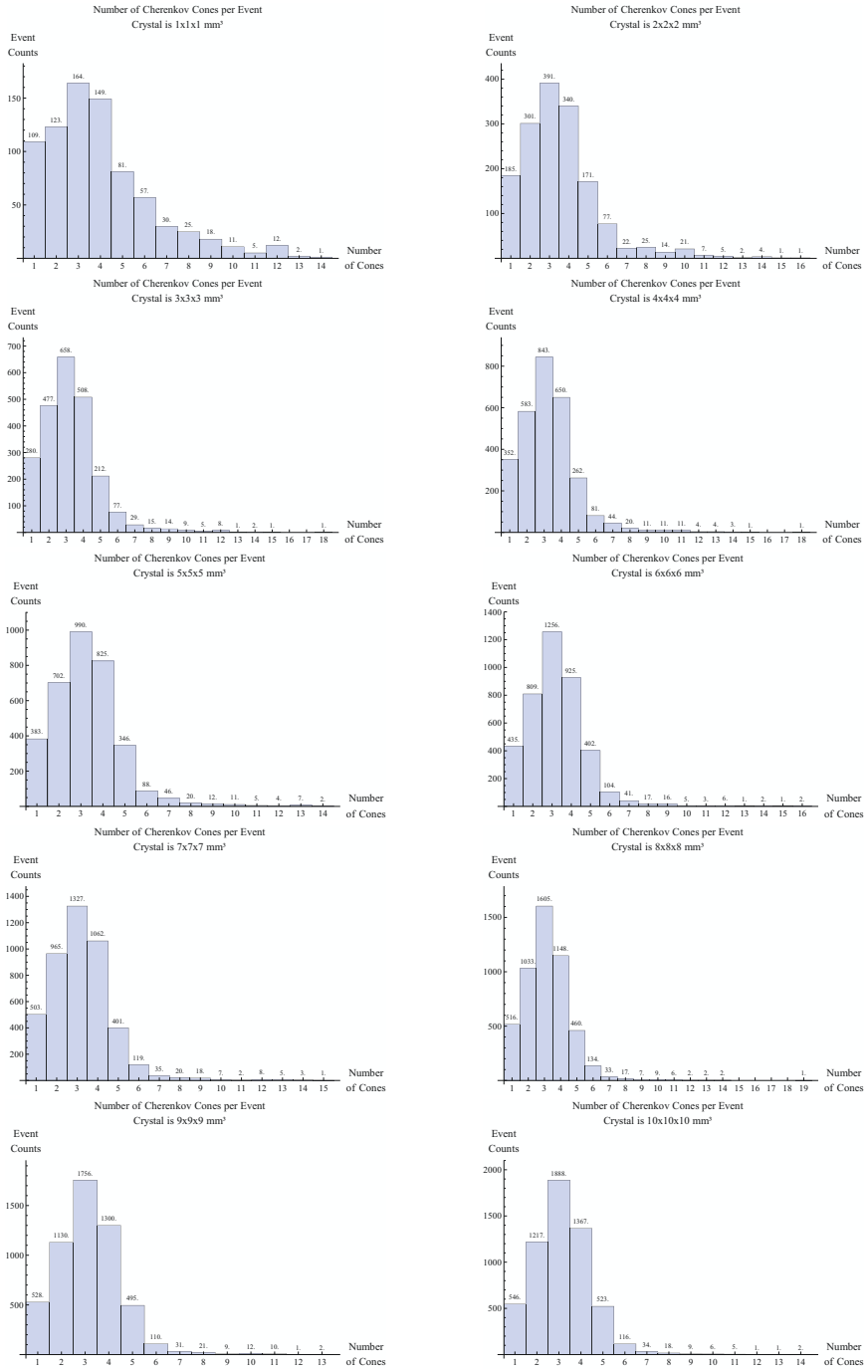

Figure B.2: Number of different Cherenkov Cones per detected event for all CHERENCUBE sizes.

Parent Initial Kinetic Energy of the First Cherenkov Cone per Event

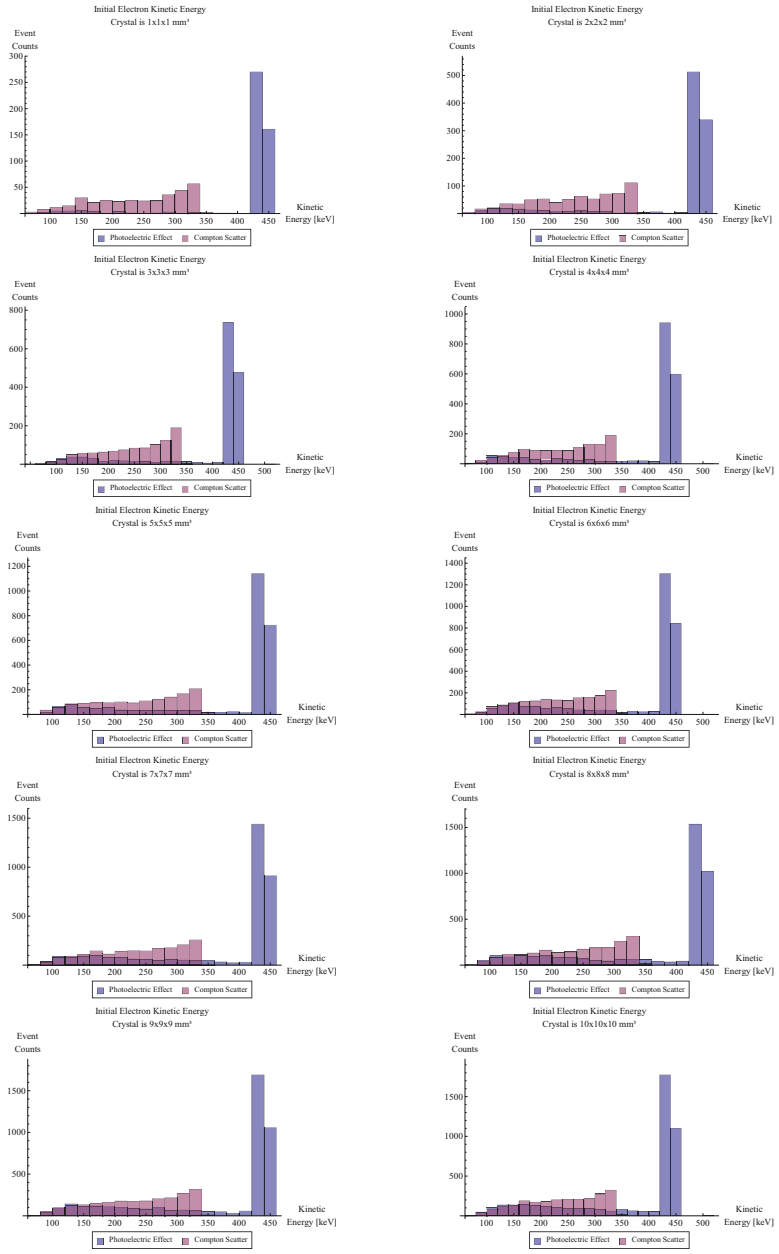

Figure B.3: Initial kinetic energy of the photoelectric and Compton generated electrons producing the first Cherenkov cone per detected event. The two photoelectric energy peaks at 422.9 and 441.4 keV correspond to the gamma-ray energy (511 keV) minus the energy of the two characteristic x-ray emissions of PWO.

Origin Distances Between Electron and Related Cherenkov Photons

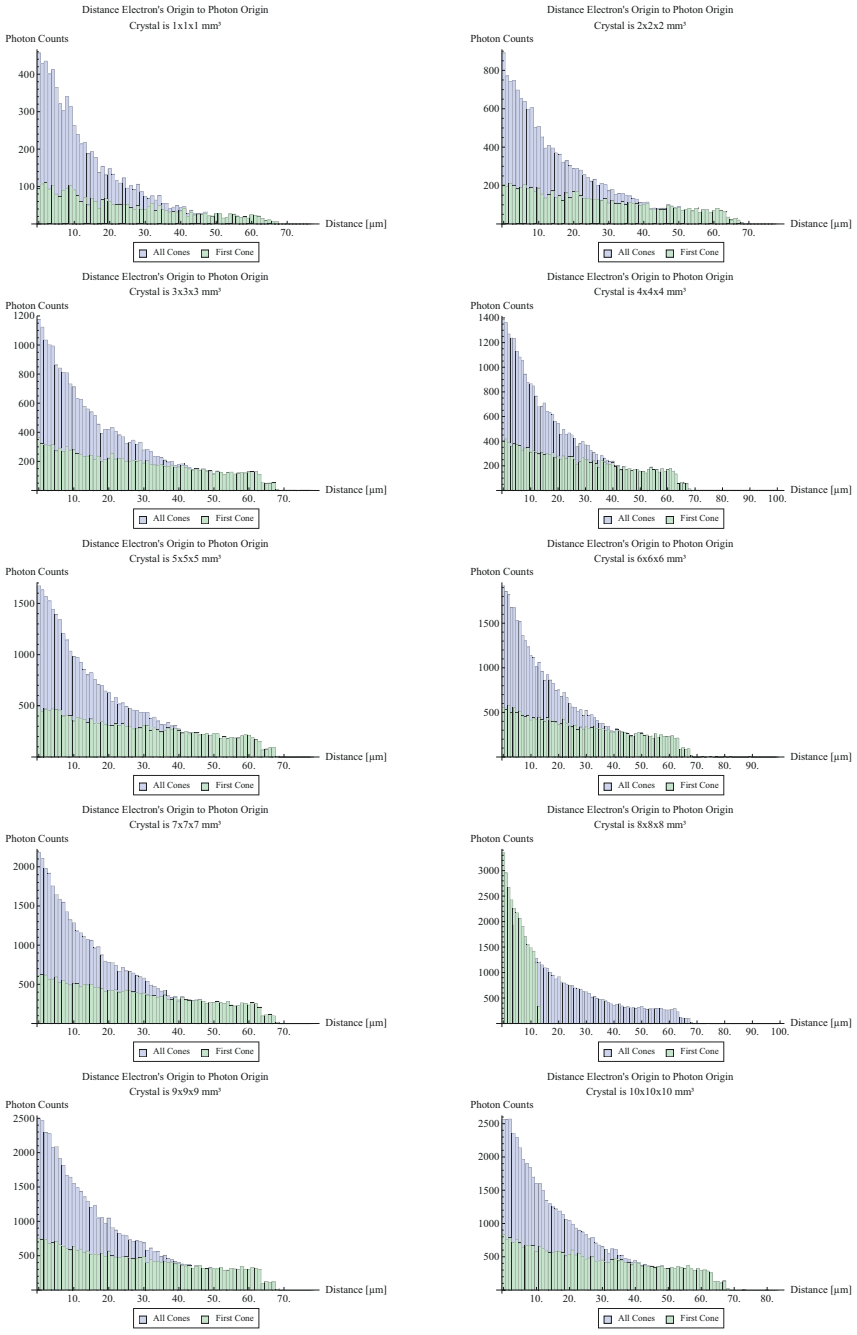

Figure B.4: Distance between the origin of each electron's trajectory and the point of emission of its related Cherenkov photons for all CHERENCUBE sizes. The maximum distance is of the order of 70 μm, regardless of the crystal size.

Path Length of Cherenkov Photons from Generation until Detection

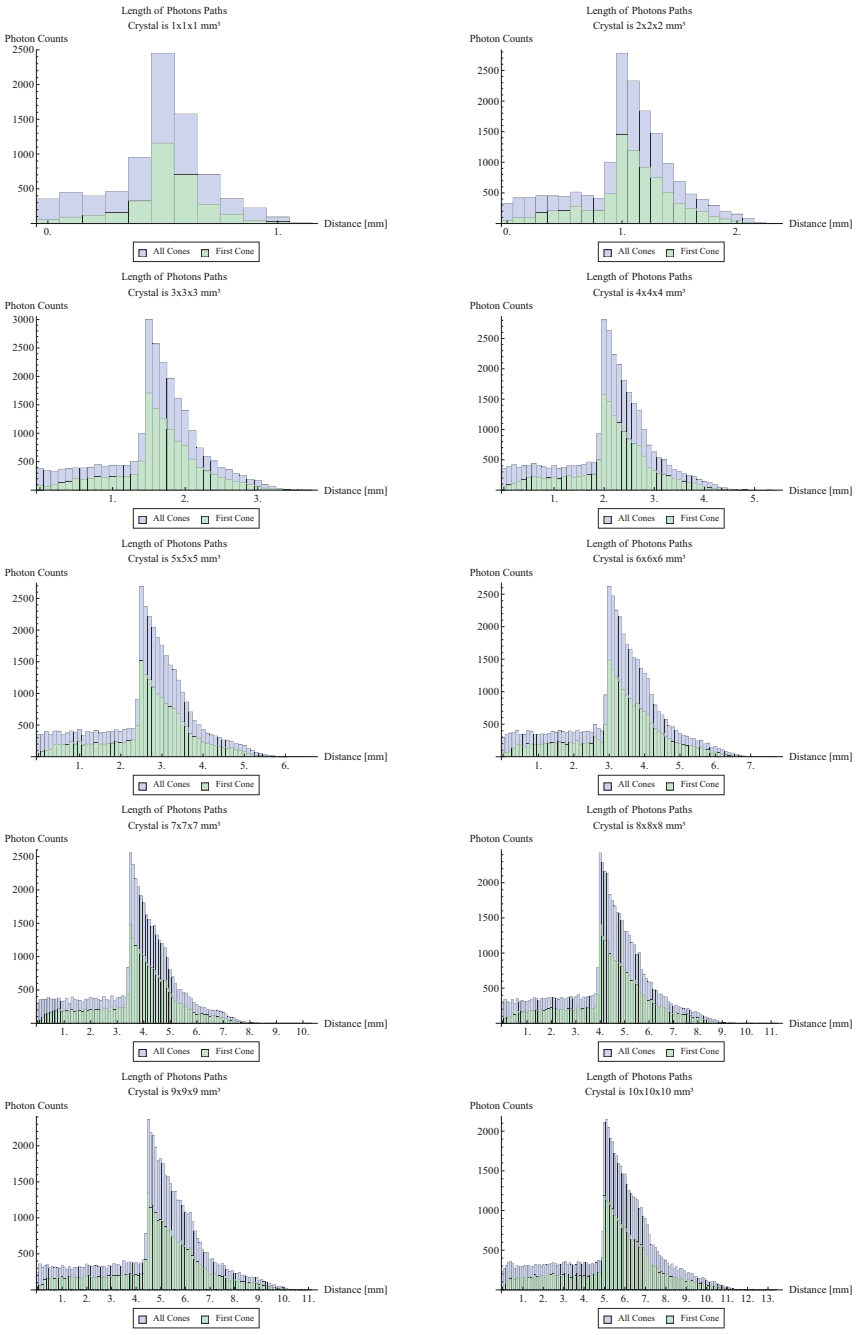

Figure B.5: Length of each Cherenkov photon's path from generation until detection for all CHERENCUBE sizes. The sharp at half the corresponding cube's size is due to the simulated scenario and the short electron range.

Absolute Detection Time of all Cherenkov Photons

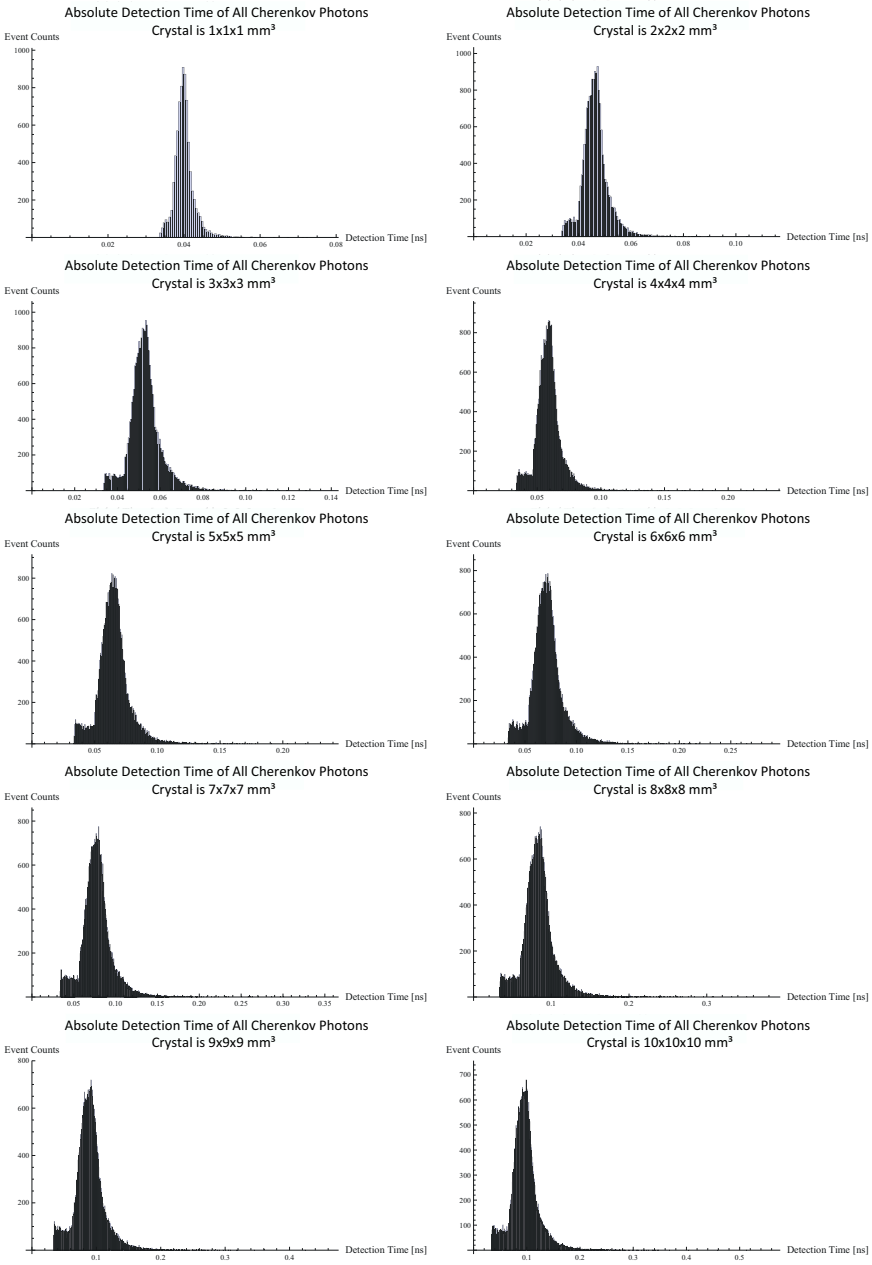

Figure B.6: Absolute detection times t_i of all photons for all CHERENCUBE sizes. The distribution is similar to that of the photon path lengths (see figure 4.8), with an offset due to the gamma-ray time-of-flight until interaction in the crystal and slightly blurred due to the different propagation velocities of the 511 keV photon (c) and the Cherenkov photons (c/n).

Appendix C

Report on the Collaborative Research between TUM and NIRS

Over the last 2 years, an international research collaboration has been established between the research group "Imaging Physics Team" of the Molecular Imaging Center at NIRS in Chiba, Japan, and the"Medical Physic" research group at the Department of Nuclear Medicine, Klinikum rechts der Isar, TUM, Munich. The main goal of this cooperation is to implement new detector technologies to achieve cutting-edge results in imaging quality for positron emission tomography (PET).

Within the framework of this project, 3 researchers from the group at NIRS have spent different periods in Munich. Among others, their work focused in experimental measurements with a new generation of photodetectors (digital silicon photomultipliers). The main result of these research stays is the publication "Parameter optimization of a digital photon counter coupled to a four-layered DOI crystal block with light sharing", submitted to scientific journal *IEEE Transactions on Nuclear Science* (TNS) in August 2014 (see appendix D). As a continuation of these activities, a two-week research stay at the group's facilities in Japan has been carried out. This report summarizes the principal tasks performed during that period.

The research group at NIRS has recently acquired the newest available version of digital silicon photomultipliers, DPCs, provided by Philips. Compared to those available at the facilities in Munich, these new sensors have been upgraded both in terms of hardware (fourfold sensor array) and software (modified functions

and data output). Therefore, the two-week work consisted in checking the proper functioning of the system, adapting the new version to the previously developed software for processing and analysing measurement data, set up a cooling system to improve the sensor's performance and finally perform measurements of low number of photons.

During the initial operation of the system, it was established that two functions (known from the previous version) were not properly working, namely the ability to apply custom inhibition masks (to activate only a specific area of the whole sensor-array) and the possibility to perform coincidence measurements between pixels of the same module. After executing different tests, the first problem was finally solved by means of a firmware update provided by the manufacturer, achieving the desired functionality. However, the second feature is currently not available and, consequently, no coincidence measurements were carried out. This feature could be implemented by means of a self-developed software-based offline coincidence sorting of data acquired in singles mode.

With the system running, the software developed in Munich for data analysis was adapted to match the new data format of the upgraded sensor version. This software converts the DPC output (text) into a ROOT file (better data compression and analysis tools), generates energy spectra histograms for every pixel and outputs the corresponding relevant information and, in the case of coincidence measurements, creates the timing histogram and saves the pertinent information. To finally check the complete data acquisition and analysis chain, a standard single-events measurement with an individual $2 \times 2 \times 8$ mm^3 LGSO scintillator, wrapped in Teflon and coupled with optical grease, was performed with a ^{22}Na radioactive source at room temperature. The system setup and output can be seen in figure C.1.

Previous experience in Munich has shown that reducing the sensor's operating temperature contributes to improve greatly its performance by reducing its intrinsic dark-count-rate. To achieve this, a Peltier-based cooling system was implemented. To avoid the appearance of condensation water while cooling down, the sensors are placed in a closed box and the air is flushed with dry nitrogen gas (see figure C.2). With this setup, the Peltier element manages to stabilize the box temperature to around 0°C, which results in a sensor temperature of 8°C. This temperature is then raised to 11°C when the sensors are fully operating, due to the heat generated by the integrated electronics.

Finally, with the temperature lowered and stabilized, a measurement of low number of impinging photons was performed. For this purpose, two different

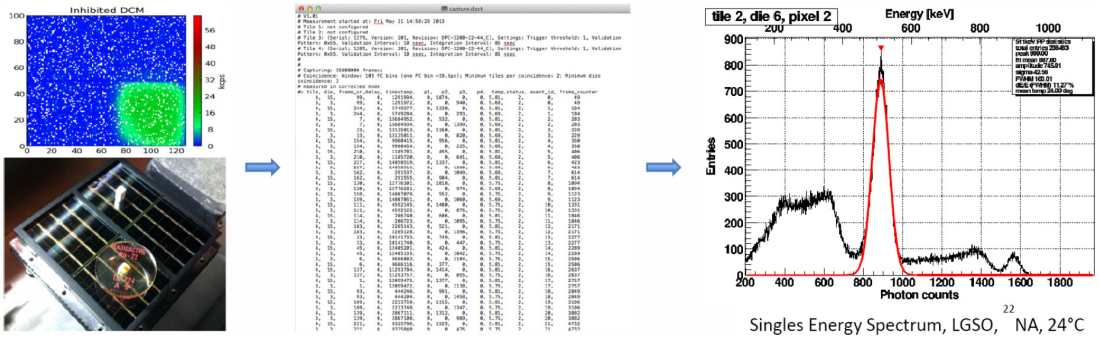

Figure C.1: System setup and output of a ^{22}Na single-events measurement with an individual $2 \times 2 \times 8$ mm^3 LGSO scintillator wrapped in Teflon and coupled with optical grease.

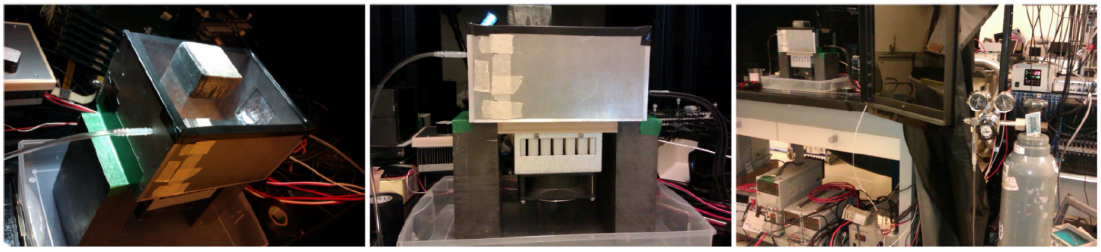

Figure C.2: Peltier-based cooling system consisting of a box filled with dry nitrogen gas.

crystal materials were coupled to the sensors using optical grease. On one tile, a $17 \times 17 \times 17$ mm^3 cube of Lead Tungstate ($PbWO_4$) was placed, whilst on other tile 2 pieces of lead glass ($3.1 \times 3.7 \times 15$ mm^3 each) were positioned. The Lead Tungstate and one of the lead glass crystals (vertically placed) were wrapped in Teflon, the second lead glass crystal was wrapped in ESR (reflecting foil) and positioned horizontally. A total of four ^{137}Cs point sources with each 3.7 MBq were placed over the crystals. The measurement was carried out by means of a dark-count map measured with longer statistics, first for 1000 frames per microcell (327.68 ms, total ca. 20 min), then repeated for 3000 frames (983.04 ms, total ca. 60 min). The measurement setup and the obtained results can be seen in figure C.3. The amount of photons generated by the lead tungstate block (about 100 ph/MeV, scintillation and Cherenkov) can be clearly recognized, while the few photons generated by the lead glass (only Cherenkov) cannot be distinguished from the dark-count activity.

Future work consists in further development of the cooling system to achieve lower temperatures and reduce the dark-count-rate to a minimum. A combination

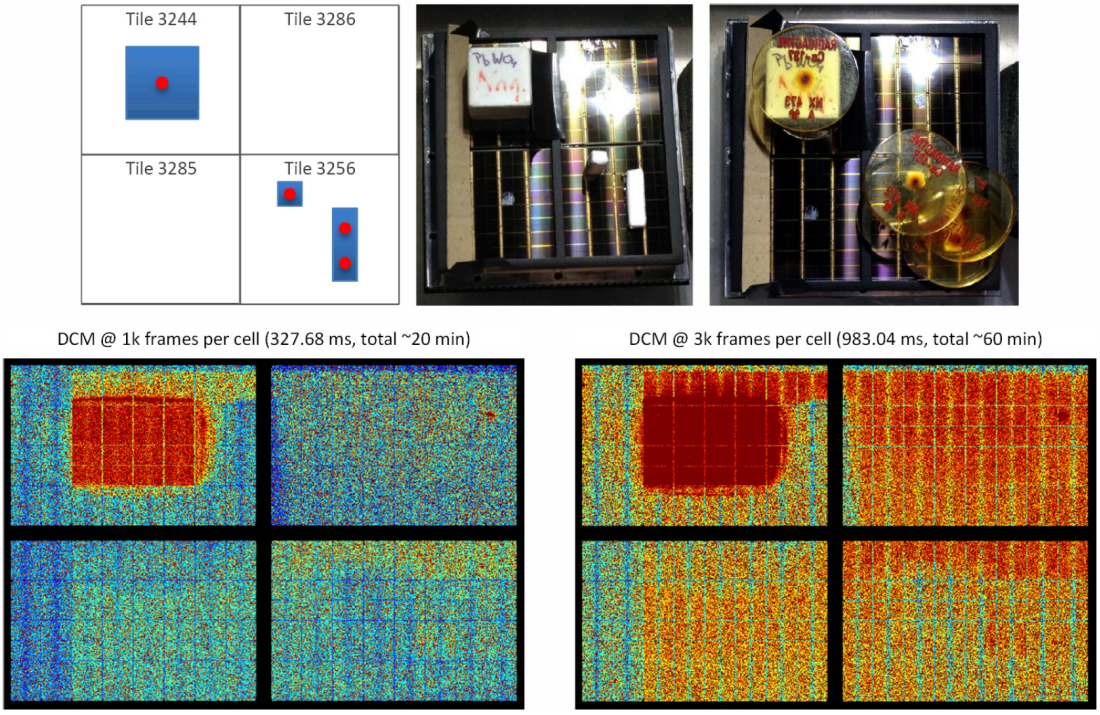

Figure C.3: Setup and results of measurement of low number of photons by means of dark-count maps.

of this and other measurement procedures (e.g. coincidence data and/or using neighbour logic) might lead to a successful recognition of a very low number of photons.

Appendix D

Publications and Active Participation in Conferences

Journal Publications as First Author

I **I. Somlai-Schweiger**, S. I. Ziegler, **CHERENCUBE: Concept Definition and Implementation Challenges of a Cherenkov-based Detector Block for PET**, accepted for publication in *Medical Physics* in April 2015, in press.

II **I. Somlai-Schweiger**, F. R. Schneider, S. I. Ziegler, **Performance Analysis of Digital Silicon Photomultipliers for PET**, submitted to the *Journal of Instrumentation* (JINST) in February 2015, reviews received and revised manuscript resubmitted.

Journal Publications as Co-Author

I E. Yoshida, **I. Somlai-Schweiger**, H. Tashima, S. I. Ziegler, T. Yamaya, **Parameter optimization of a digital photon counter coupled to a four-layered DOI crystal block with light sharing**, accepted for publication in *IEEE Transactions on Nuclear Science* (TNS) in 2015, in press.

II F. R. Schneider, K. Shimazoe, **I. Somlai-Schweiger**, S. I. Ziegler, **A PET detector prototype based on digital SiPMs and GAGG scintillators**, published in *Physics in Medicine and Biology*, Phys. Med. Biol. 60 (2015) 1667-1679. (2015)

III T. L. Schenck, U. Hopfner, M. N. Chávez, H. G. Machens, **I. Somlai-Schweiger**, R. E. Giunta, A. V. Bohne, J. Nickelsen, M. L. Allende, J. T. Egaña, **Photosynthetic Biomaterials: A Pathway Towards Autotrophic Tissue Engineering**, published in *Acta Biomaterialia*, 2015, 15, 39 - 47. (Publication resulting from the first lab rotation required for the PhD program.) (2015)

IV N. Aubry, E. Auffray, F. B. Mimoun, N. Brillouet, R. Bugalho, E. Charbon, O. Charles, D. Cortinovis, P. Courday, A. Cserkaszky, C. Damon, K. Doroud, J. M. Fischer, G. Fornaro, J. M. Fourmigue, B. Frisch, B. Frst, J. Gardiazabal, K. Gadow, E. Garutti, C. Gaston, A. Gil-Ortiz, E. Guedj, T. Harion, P. Jarron, J. Kabadanian, T. Lasser, R. Laugier, P. Lecoq, D. Lombardo, S. Mandai, E. Mas, T. Meyer, O. Mundler, N. Navab, C. Ortigo, M. Paganoni, D. Perrodin, M. Pizzichemi, J. O. Prior, T. Reichl, M. Reinecke, M. Rolo, H. C. Schultz-Coulon, M. Schwaiger, W. Shen, A. Silenzi, J. C. Silva, R. Silva, **I. Somlai-Schweiger**, R. Stamen, J. Traub, J. Varela, V. Veckalns, V. Vidal, J. Vishwas, T. Wendler, C. Xu, S. I. Ziegler, M. Zvolsky, **EndoTOFPET-US: a novel multimodal tool for endoscopy and positron emission tomography**, published in *Journal of Instrumentation* 8[04]:C04002, 2013. (Publication resulting from the work done in the EU project ENDOTOFPET-US.) (2013)

Participation in International Conferences

I **I. Somlai-Schweiger**, S. I. Ziegler, **Monte Carlo Simulations of a Cherenkov-Only PET Detector Block with 6-Sided-Readout**, IEEE NSS/MIC 2014, Seattle, Oral Presentation M12-8 (Student Paper Competition and MIC Trainee Grant).

II E. Yoshida, **I. Somlai-Schweiger**, H. Tashima, S. I. Ziegler, T. Yamaya, **Optimization of Digital SiPMs Coupled to a Four-Layered DOI Crystal Block with Light Sharing**, IEEE NSS/MIC 2014, Poster Presentation M19-115.

III **I. Somlai-Schweiger**, **State-Of-The-Art Photodetectors for TOF-PET**, GMP Workshop PET/CT, Wien, 19th September 2014, Oral Presentation.

IV **I. Somlai-Schweiger**, **Basics of Nuclear Medicine Imaging - Positron Emission Tomography (PET) Instrumentation**, International Workshop on Biological Sciences - UACH, Valdivia, 3rd - 5th January 2014, Oral Presentation.

V J. Cabello, F. R. Schneider, **I. Somlai-Schweiger**, G. Llosa, M. Rafecas, S. I. Ziegler, **Compton Interaction Identification in Monolithic Scintillators: a Simulation Study with Ce:GAGG**, IEEE NSS/MIC 2013, Seoul, Poster Presentation M11-40.

VI **I. Somlai-Schweiger**, F. R. Schneider, K. Shimazoe, H. Takahashi, S. I. Ziegler, **Performance Analysis of Digital Silicon Photomultipliers for PET**, IEEE NSS/MIC 2013, Seoul, Poster Presentation NPO1-107.

VII K. Shimazoe, T. Orita, H. Takahashi, **I. Somlai-Schweiger**, F. R. Schneider, S. I. Ziegler, **Development of a Compton Camera Based on Digital SiPMs and GAGG Crystals**, IEEE NSS/MIC 2013, Seoul, Poster Presentation NPO1-152.

VIII F. R. Schneider, K. Shimazoe, **I. Somlai-Schweiger**, K. Kamada, H. Takahashi, S. I. Ziegler, **A PET prototype based on digital SiPMs and GAGG scintillators**, The Journal of Nuclear Medicine Meeting Abstracts, May 2013; 54: 429.

List of Figures

List of Tables

Bibliography

[1] Terry Jones. **The role of positron emission tomography within the spectrum of medical imaging**. *European Journal of Nuclear Medicine*, **23**[2]:207–211, 1996. doi:10.1007/BF01731847. 1

[2] Michael Kassiou, Richard Banati, R.M. Damian Holsinger, and Steve Meikle. **Challenges in molecular imaging of Parkinsons disease: A brief overview**. *Brain Research Bulletin*, **78**[23]:105 – 108, 2009. Movement Disorders: Focus on the thalamus and basal ganglia. doi:http://dx.doi.org/10.1016/j.brainresbull.2008.08.006. 1

[3] M.N. Wernick and J.N. Aarsvold. *Emission Tomography: The Fundamentals of PET and SPECT*. Elsevier Science, 2004. 4

[4] D.L. Bailey, D.W. Townsend, P.E. Valk, and M.N. Maisey. *Positron Emission Tomography: Basic Sciences*. Springer, 2006. 4, 5, 7, 8, 10, 12, 14, 16, 26, 27, 30, 104, 112

[5] S.R. Cherry, J.A. Sorenson, and M.E. Phelps. *Physics in Nuclear Medicine*. Elsevier Health Sciences, 2012. 5, 6, 8, 9, 11, 14, 25, 27, 30, 104, 112

[6] William C Eckelman. **Sensitivity of New Radiopharmaceuticals**. *Nuclear Medicine and Biology*, **25**[3]:169 – 173, 1998. doi:http://dx.doi.org/10.1016/S0969-8051(97)00207-2. 6

[7] Philip H Elsinga. **Radiopharmaceutical chemistry for positron emission tomography**. *Methods*, **27**[3]:208 – 217, 2002. doi:http://dx.doi.org/10.1016/S1046-2023(02)00076-2. 6

[8] David J. Schlyer. **PET tracers and radiochemistry.** *Ann Acad Med Singapore*, **33(2)**[0304-4602 (Linking)]:146–154, 2004. 6

[9] O. Warburg, F. Wind, and E. Negelein. **The Metabolism Of Tumors In The Body**. *J Gen Physiol*, **8(6)**[0022-1295 (Linking)]:519530, 1927. 7

[10] T Ido, C-N Wan, V Casella, JS Fowler, AP Wolf, M Reivich, and DE Kuhl. **Labeled 2-deoxy-D-glucose analogs. 18F-labeled 2-deoxy-2-fluoro-D-glucose, 2-deoxy-2-fluoro-D-mannose and 14C-2-deoxy-2-fluoro-D-glucose**. *Journal of Labelled Compounds and Radiopharmaceuticals*, **14**[2]:175–183, 1978. 7

[11] M Reivich, D Kuhl, A Wolf, J Greenberg, M Phelps, T Ido, V Casella, J Fowler, E Hoffman, A Alavi, P Som, and L Sokoloff. **The [18F]fluorodeoxyglucose method for the measurement of local cerebral glucose utilization in man.** *Circulation Research*, **44**[1]:127–37, 1979. arXiv:http://circres.ahajournals.org/content/44/1/127.full.pdf+html, doi:10.1161/01.RES.44.1.127. 7

[12] D A Silver, I Pellicer, W R Fair, W D Heston, and C Cordon-Cardo. **Prostate-specific membrane antigen expression in normal and malignant human tissues.** *Clinical Cancer Research*, **3**[1]:81–85, 1997. arXiv:http://clincancerres.aacrjournals.org/content/3/1/81.full.pdf+html. 7

[13] Sven Perner, Matthias D. Hofer, Robert Kim, Rajal B. Shah, Haojie Li, Peter Mller, Richard E. Hautmann, Juergen E. Gschwend, Rainer Kuefer, and Mark A. Rubin. **Prostate-specific membrane antigen expression as a predictor of prostate cancer progression**. *Human Pathology*, **38**[5]:696 – 701, 2007. doi:http://dx.doi.org/10.1016/j.humpath.2006.11.012. 7

[14] Ali Afshar-Oromieh, ChristianM. Zechmann, Anna Malcher, Matthias Eder, Michael Eisenhut, HeinzG. Linhart, Tim Holland-Letz, BorisA. Hadaschik, FrederikL. Giesel, Jrgen Debus, and Uwe Haberkorn. **Comparison of PET imaging with a 68Ga-labelled PSMA ligand and 18F-choline-based PET/CT for the diagnosis of recurrent prostate cancer**. *European Journal of Nuclear Medicine and Molecular Imaging*, **41**[1]:11–20, 2014. doi:10.1007/s00259-013-2525-5. 7

[15] J. Radon. **Über die Bestimmung von Funktionen durch ihre Integralwerte längs gewisser Mannigfaltigkeiten**. *Akad. Wiss.*, **69**:262–277, 1917. 8

[16] R.E. Henkin. *Nuclear medicine*. Number Bd. 2 in Nuclear Medicine. Mosby Elsevier, 2006. 8, 104

[17] A. P. Dempster, N. M. Laird, and D. B. Rubin. **Maximum Likelihood from Incomplete Data via the EM Algorithm**. *Journal of the Royal Statistical Society. Series B (Methodological)*, **39**[1]:pp. 1–38, 1977. 12

[18] L.A. Shepp and Y. Vardi. **Maximum Likelihood Reconstruction for Emission Tomography**. *Medical Imaging, IEEE Transactions on*, **1**[2]:113–122, Oct 1982. doi:10.1109/TMI.1982.4307558. 12

[19] H.M. Hudson and R.S. Larkin. **Accelerated image reconstruction using ordered subsets of projection data**. *Medical Imaging, IEEE Transactions on*, **13**[4]:601–609, Dec 1994. doi:10.1109/42.363108. 12

[20] J.M. Ollinger and J.A. Fessler. **Positron-emission tomography**. *Signal Processing Magazine, IEEE*, **14**[1]:43–55, Jan 1997. doi:10.1109/79.560323. 12

[21] Richard M Leahy and Jinyi Qi. **Statistical approaches in quantitative positron emission tomography**. *Statistics and Computing*, **10**[2]:147–165, 2000. 12

[22] Carole Lartizien, Paul E. Kinahan, Richard Swensson, Claude Comtat, Michael Lin, Victor Villemagne, and Rgine Trbossen. **Evaluating Image Reconstruction Methods for Tumor Detection in 3-Dimensional Whole-Body PET Oncology Imaging**. *Journal of Nuclear Medicine*, **44**[2]:276–290, 2003. arXiv:http://jnm.snmjournals.org/content/44/2/276.full.pdf+html. 12

[23] O. Klein and Y. Nishina. **ber die Streuung von Strahlung durch freie Elektronen nach der neuen relativistischen Quantendynamik von Dirac**. *Zeitschrift fr Physik*, **52**[11-12]:853–868, 1929. doi:10.1007/BF01366453. 14

[24] S.E. Derenzo, M.J. Weber, W.W. Moses, and C. Dujardin. **Measurements of the intrinsic rise times of common inorganic scintillators**. *Nuclear Science, IEEE Transactions on*, **47**[3]:860–864, Jun 2000. doi:10.1109/23.856531. 15

[25] S Seifert, J H L Steenbergen, H T van Dam, and D R Schaart. **Accurate measurement of the rise and decay times of fast scintillators with solid state photon counters**. *Journal of Instrumentation*, **7**[09]:P09004, 2012. 15

[26] Robley Dunglison Evans. *The atomic nucleus*. International series in pure and applied physics. McGraw-Hill, January 1955. 15, 62

[27] M.E. Phelps. *PET: Physics, Instrumentation, and Scanners*. Springer, 2006. 16, 18, 22, 25, 104, 105, 112

[28] C.L. Melcher and J.S. Schweitzer. **Cerium-doped lutetium oxyorthosilicate: a fast, efficient new scintillator**. *Nuclear Science, IEEE Transactions on*, **39**[4]:502–505, Aug 1992. doi:10.1109/23.159655. 16

[29] M E Daube-Witherspoon, S Surti, A Perkins, C C M Kyba, R Wiener, M E Werner, R Kulp, and J S Karp. **The imaging performance of a LaBr 3 -based PET scanner**. *Physics in Medicine and Biology*, **55**[1]:45, 2010. 17, 28

[30] Kei Kamada, Petr Prusa, Martin Nikl, Claudio Piemonte, Alessandro Tarolli, Takayuki Yanagida, Takanori Endo, Kousuke Tsutumi, and Akira Yoshikawa. **2-inch size crystal growth of Ce:$Gd_3Al_2Ga_3O_{12}$ with various Ce concentration and their scintillation properties**. In *2012 IEEE Nuclear Science Symposium and Medical Imaging Conference Record (NSS/MIC)*, pages 1698–1701. IEEE, October 2012. doi:10.1109/NSSMIC.2012.6551401. 17, 36, 56

[31] D Renker and E Lorenz. **Advances in solid state photon detectors**. *Journal of Instrumentation*, **4**[04]:P04004–P04004, April 2009. doi:10.1088/1748-0221/4/04/P04004. 19, 41, 106

[32] SibylleI. Ziegler, BerndJ. Pichler, Guido Boening, Magdalena Rafecas, Wendelin Pimpl, Eckart Lorenz, Norbert Schmitz, and Markus Schwaiger. **A prototype high-resolution animal positron tomograph with avalanche photodiode arrays and LSO crystals**. *European Journal of Nuclear Medicine*, **28**[2]:136–143, 2001. doi:10.1007/s002590000438. 19, 24

[33] Bernd J. Pichler, Martin S. Judenhofer, Ciprian Catana, Jeffrey H. Walton, Manfred Kneilling, Robert E. Nutt, Stefan B. Siegel, Claus D. Claussen, and Simon R. Cherry. **Performance Test of an LSO-APD Detector in a 7-T MRI Scanner for Simultaneous PET/MRI**. *Journal of Nuclear Medicine*, **47**[4]:639–647, 2006. arXiv:http://jnm.snmjournals.org/content/47/4/639.full.pdf+html. 19

[34] Gaspar Delso, Sebastian Frst, Bjrn Jakoby, Ralf Ladebeck, Carl Ganter, Stephan G. Nekolla, Markus Schwaiger, and Sibylle I. Ziegler. **Performance Measurements of the Siemens mMR Integrated Whole-Body PET/MR Scanner**. *Journal of Nuclear Medicine*, **52**[12]:1914–1922, 2011. arXiv:http://jnm.snmjournals.org/content/52/12/1914.full.pdf+html, doi:10.2967/jnumed.111.092726. 19

[35] Bernd J. Pichler, Hans F. Wehrl, Armin Kolb, and Martin S. Judenhofer. **Positron Emission Tomography/Magnetic Resonance Imaging: The Next Generation of Multimodality Imaging?** *Seminars in Nuclear Medicine*, **38**[3]:199 – 208, 2008. Developments in Instrumentation. doi:http://dx.doi.org/10.1053/j.semnuclmed.2008.02.001. 19, 104

[36] Z. Sadygov. **Avalanche Detector**. *Russian Agency for Patents and Trademarks*, **Patent No. RU 2102820**, 1998. 20, 105

[37] Jozef Pulko. *A Monte-Carlo Model of a Silicon Photomultiplier*. PhD thesis, Physics Department E18, Technische Universitt Mnchen, Munich, Germany, 2011. 20, 21, 105

[38] Armin Kolb, Eckart Lorenz, Martin S Judenhofer, Dieter Renker, Konrad Lankes, and Bernd J Pichler. **Evaluation of Geiger-mode APDs for PET block detector designs**. *Physics in Medicine and Biology*, **55**[7]:1815, 2010. 20

[39] D Renker. **Geiger-mode avalanche photodiodes, history, properties and problems**. *Nuclear Instruments and Methods in Physics Research Section A: Accelerators, Spectrometers, Detectors and Associated Equipment*, **567**[1]:48–56, November 2006. doi:10.1016/j.nima.2006.05.060. 21, 33

[40] F R Schneider, T R Ganka, G Şeker, E Engelmann, D Renker, S Paul, W Hansch, and S I Ziegler. **Characterization of blue sensitive 3×3 mm^2 SiPMs and their use in PET**. *Journal of Instrumentation*, **9**[07]:P07027–P07027, July 2014. doi:10.1088/1748-0221/9/07/P07027. 21, 52, 56, 58, 59

[41] Gaspar Delso, Mehdi Khalighi, Marlena Hofbauer, Miguel Porto, Patrick Veit-Haibach, and Gustav von Schulthess. **Preliminary evaluation of image quality in a new clinical ToF-PET/MR scanner**. *EJNMMI Physics*, **1**[1]:1–2, 2014. doi:10.1186/2197-7364-1-S1-A41. 21, 33

[42] V. Schulz, T. Solf, B. Weissler, P. Gebhardt, P. Fischer, M. Ritzert, V. Mlotok, C. Piemonte, N. Zorzi, M. Melchiorri, S. Vandenberghe, V. Keereman, T. Schaeffter, and P.K. Marsden. **A preclinical PET/MR insert for a human 3T MR scanner**. In *Nuclear Science Symposium Conference Record (NSS/MIC), 2009 IEEE*, pages 2577–2579, Oct 2009. doi:10.1109/NSSMIC.2009.5402018. 21, 33

[43] Hyun Suk Yoon, Guen Bae Ko, Sun Il Kwon, Chan Mi Lee, Mikiko Ito, In Chan Song, Dong Soo Lee, Seong Jong Hong, and Jae Sung Lee.

Initial Results of Simultaneous PET/MRI Experiments with an MRI-Compatible Silicon Photomultiplier PET Scanner. *Journal of Nuclear Medicine*, **53**[4]:608–614, 2012. arXiv:http://jnm.snmjournals.org/content/53/4/608.full.pdf+html, doi:10.2967/jnumed.111.097501. 21, 33

[44] Hal O. Anger. **Scintillation Camera**. *Review of Scientific Instruments*, **29**[1]:27–33, 1958. doi:http://dx.doi.org/10.1063/1.1715998. 22

[45] Lars-Eric Adam, Joel S. Karp, Margaret E. Daube-Witherspoon, and Robin J. Smith. **Performance of a Whole-Body PET Scanner Using Curve-Plate NaI(Tl) Detectors**. *Journal of Nuclear Medicine*, **42**[12]:1821–1830, 2001. arXiv:http://jnm.snmjournals.org/content/42/12/1821.full.pdf+html. 23

[46] M.E. Casey and R. Nutt. **A Multicrystal Two Dimensional BGO Detector System for Positron Emission Tomography**. *Nuclear Science, IEEE Transactions on*, **33**[1]:460–463, Feb 1986. doi:10.1109/TNS.1986.4337143. 23

[47] Gaspar Delso and Sibylle Ziegler. **PET/MRI system design**. *European Journal of Nuclear Medicine and Molecular Imaging*, **36**[1]:86–92, 2009. doi:10.1007/s00259-008-1008-6. 23

[48] S.R. Cherry, Y. Shao, R.W. Silverman, K. Meadors, S. Siegel, A. Chatziioannou, J.W. Young, W.F. Jones, J.C. Moyers, D. Newport, A. Boutefnouchet, T.H. Farquhar, M. Andreaco, M.J. Paulus, D.M. Binkley, R. Nutt, and M.E. Phelps. **MicroPET: a high resolution PET scanner for imaging small animals**. *Nuclear Science, IEEE Transactions on*, **44**[3]:1161–1166, Jun 1997. doi:10.1109/23.596981. 24

[49] Jin Ho Jung, Yong Choi, Key Jo Hong, Jihoon Kang, Wei Hu, Hyun Keong Lim, Yoonsuk Huh, Sangsu Kim, Jiwoong Jung, and Kyu Bom Kim. **Development of brain PET using GAPD arrays**. *Medical Physics*, **39**[3]:1227–1233, 2012. doi:http://dx.doi.org/10.1118/1.3681012. 24

[50] J.S. Huber, W.W. Moses, S.E. Derenzo, H. Ho, M.S. Andreaco, M.J. Paulus, and R. Nutt. **Characterization of a 64 channel PET detector using photodiodes for crystal identification**. *Nuclear Science, IEEE Transactions on*, **44**[3]:1197–1201, Jun 1997. doi:10.1109/23.596987. 24

[51] Herman T van Dam, Stefan Seifert, Ruud Vinke, Peter Dendooven, Herbert Löhner, Freek J Beekman, and Dennis R Schaart. **A prac-**

tical method for depth of interaction determination in monolithic scintillator PET detectors. *Physics in medicine and biology*, **56**[13]:4135–45, July 2011. doi:10.1088/0031-9155/56/13/025. 24, 32, 78

[52] J Cabello, P Barrillon, J Barrio, M.G. Bisogni, A. Del Guerra, C Lacasta, M Rafecas, H Saikouk, C Solaz, P Solevi, C de La Taille, and G Llosá. **High resolution detectors based on continuous crystals and SiPMs for small animal PET**. *Nuclear Instruments and Methods in Physics Research Section A: Accelerators, Spectrometers, Detectors and Associated Equipment*, **718**[0]:148–150, August 2013. doi:10.1016/j.nima.2012.08.094. 24, 32

[53] W.W. Moses. **Time of flight in pet revisited**. *IEEE Transactions on Nuclear Science*, **50**[5]:1325–1330, October 2003. doi:10.1109/TNS.2003.817319. 27, 105

[54] Maurizio Conti. **State of the art and challenges of time-of-flight PET.** *Physica medica : PM : an international journal devoted to the applications of physics to medicine and biology : official journal of the Italian Association of Biomedical Physics (AIFB)*, **25**[1]:1–11, March 2009. doi:10.1016/j.ejmp.2008.10.001. 27

[55] Suleman Surti, Austin Kuhn, Matthew E. Werner, Amy E. Perkins, Jeffrey Kolthammer, and Joel S. Karp. **Performance of Philips Gemini TF PET/CT Scanner with Special Consideration for Its Time-of-Flight Imaging Capabilities**. *Journal of Nuclear Medicine*, **48**[3]:471–480, 2007. arXiv:http://jnm.snmjournals.org/content/48/3/471.full.pdf+html. 28

[56] Brad Kemp, John Williams, Royce Ruter, Val Lowe, and Brian Mullan. **Performance measurements of a whole body PET/CT system with time-of-flight capability**. *J NUCL MED MEETING ABSTRACTS*, **50**[2_MeetingAbstracts]:1546, 2009. 28

[57] B W Jakoby, Y Bercier, M Conti, M E Casey, B Bendriem, and D W Townsend. **Physical and clinical performance of the mCT time-of-flight PET/CT scanner**. *Physics in Medicine and Biology*, **56**[8]:2375, 2011. 28

[58] Michael Miller, Jerome Griesmer, David Jordan, Thomas Laurence, Raymond Muzic, Manoj Narayanan, Deepa Natarajamani, Kuan-Hao Su, and Sharon Wang. **Initial characterization of a prototype digital**

photon counting PET system. *J NUCL MED MEETING ABSTRACTS*, **55**[1_MeetingAbstracts]:658, 2014. 28, 34

[59] Cristina Lois, Bjoern W. Jakoby, Misty J. Long, Karl F. Hubner, David W. Barker, Michael E. Casey, Maurizio Conti, Vladimir Y. Panin, Dan J. Kadrmas, and David W. Townsend. **An Assessment of the Impact of Incorporating Time-of-Flight Information into Clinical PET/CT Imaging**. *Journal of Nuclear Medicine*, **51**[2]:237–245, 2010. arXiv:http://jnm.snmjournals.org/content/51/2/237.full.pdf+html, doi:10.2967/jnumed.109.068098. 28

[60] Stefan Seifert, Herman T. van Dam, Ruud Vinke, Peter Dendooven, Herbert Lohner, Freek J Beekman, and Dennis R Schaart. **A Comprehensive Model to Predict the Timing Resolution of SiPM-Based Scintillation Detectors: Theory and Experimental Validation**. *IEEE Transactions on Nuclear Science*, **59**[1]:190–204, February 2012. doi:10.1109/TNS.2011.2179314. 28, 62

[61] N Aubry, E Auffray, F B Mimoun, N Brillouet, R Bugalho, E Charbon, O Charles, D Cortinovis, P Courday, A Cserkaszky, C Damon, K Doroud, J M Fischer, G Fornaro, J M Fourmigue, B Frisch, B Frst, J Gardiazabal, K Gadow, E Garutti, C Gaston, A Gil-Ortiz, E Guedj, T Harion, P Jarron, J Kabadanian, T Lasser, R Laugier, P Lecoq, D Lombardo, S Mandai, E Mas, T Meyer, O Mundler, N Navab, C Ortigo, M Paganoni, D Perrodin, M Pizzichemi, J O Prior, T Reichl, M Reinecke, M Rolo, H C Schultz-Coulon, M Schwaiger, W Shen, A Silenzi, J C Silva, R Silva, I Somlai Schweiger, R Stamen, J Traub, J Varela, V Veckalns, V Vidal, J Vishwas, T Wendler, C Xu, S Ziegler, and M Zvolsky. **EndoTOFPET-US: a novel multimodal tool for endoscopy and positron emission tomography**. *Journal of Instrumentation*, **8**[04]:C04002, 2013. 28

[62] Craig S Levin and Habib Zaidi. **Current Trends in Preclinical PET System Design**. *PET Clinics*, **2**[2]:125–160, April 2007. doi:10.1016/j.cpet.2007.12.001. 31

[63] Yuchuan Wang, Jurgen Seidel, Benjamin M W Tsui, Juan J Vaquero, and Martin G Pomper. **Performance Evaluation of the GE Healthcare eXplore VISTA Dual-Ring Small-Animal PET Scanner**. *Journal of Nuclear Medicine*, **47**[11]:1891–1900, 2006. 31

[64] Virginia Spanoudaki, Irene Torres-Espallardo, Magdalena Rafecas, and Sibylle Ziegler. **Performance evaluation of MADPET-II, a small animal dual layer LSO-APD PET scanner with individual detector read out and depth of interaction information**. *Journal of Nuclear Medicine*, **48**[MeetingAbstracts2]:39, 2007. 32

[65] W.W. Moses and S.E. Derenzo. **Design studies for a PET detector module using a PIN photodiode to measure depth of interaction**. *IEEE Transactions on Nuclear Science*, **41**[4]:1441–1445, August 1994. doi:10.1109/23.322929. 32

[66] Y Shao, R.W. Silverman, R Farrell, L Cirignano, R Grazioso, K.S. Shah, G Vissel, M Clajus, T.O. Tumer, and S.R. Cherry. **Design studies of a high resolution PET detector using APD arrays**. *IEEE Transactions on Nuclear Science*, **47**[3]:1051–1057, June 2000. doi:10.1109/23.856546. 32

[67] T. Tsuda, H. Murayama, K. Kitamura, N. Inadama, T. Yamaya, E. Yoshida, F. Nishikido, M. Hamamoto, H. Kawai, and Y. Ono. **Performance evaluation of a subset of a four-layer LSO detector for a small animal DOI PET scanner: jPET-RD**. *Nuclear Science, IEEE Transactions on*, **53**[1]:35–39, Feb 2006. doi:10.1109/TNS.2005.862961. 32

[68] Taiga Yamaya, Takayuki Mitsuhashi, Takahiro Matsumoto, Naoko Inadama, Fumihiko Nishikido, Eiji Yoshida, Hideo Murayama, Hideyuki Kawai, Mikio Suga, and Mitsuo Watanabe. **A SiPM-based isotropic-3D PET detector X'tal cube with a three-dimensional array of 1 mm(3) crystals.** *Physics in medicine and biology*, **56**[21]:6793–807, November 2011. doi:10.1088/0031-9155/56/21/003. 32, 62, 78

[69] T Frach, G Prescher, C Degenhardt, R de Gruyter, A Schmitz, and R Ballizany. **The digital silicon photomultiplier - Principle of operation and intrinsic detector performance**. In *2009 IEEE Nuclear Science Symposium Conference Record (NSS/MIC)*, pages 1959–1965. IEEE, October 2009. doi:10.1109/NSSMIC.2009.5402143. 33, 39, 56

[70] York Haemisch, Thomas Frach, Carsten Degenhardt, and Andreas Thon. **Fully Digital Arrays of Silicon Photomultipliers (dSiPM) - a Scalable Alternative to Vacuum Photomultiplier Tubes (PMT)**. *Physics Procedia*, **37**[0]:1546–1560, 2012. doi:10.1016/j.phpro.2012.03.749. 33, 34, 105

[71] Ralf Schulze. *PDPC-TEK User Manual*. Philips Digital Photon Counting, v0.18 edition, 2013. 33, 35, 36, 37, 38, 39, 41, 52, 54, 58, 105, 112

[72] V Tabacchini, V Westerwoudt, G Borghi, S Seifert, and D R Schaart. **Probabilities of triggering and validation in a digital silicon photomultiplier**. *Journal of Instrumentation*, **9**[06]:P06016–P06016, June 2014. doi:10.1088/1748-0221/9/06/P06016. 34

[73] Herman T van Dam, Stefan Seifert, and Dennis R Schaart. **The statistical distribution of the number of counted scintillation photons in digital silicon photomultipliers: model and validation**. *Physics in Medicine and Biology*, **57**[15]:4885, 2012. 34

[74] Jung Yeol Yeom, R Vinke, M F Bieniosek, and C S Levin. **Comparison of end/side scintillator readout with digital-SiPM for ToF PET**. In *Nuclear Science Symposium and Medical Imaging Conference (NSS/MIC), 2013 IEEE*, pages 1–3, 2013. doi:10.1109/NSSMIC.2013.6829322. 34

[75] R Marcinkowski, S Espana, H Thoen, and S Vandenberghe. **Performance of Digital Silicon Photomultipliers for Time of Flight PET scanners**. In *2012 IEEE Nuclear Science Symposium and Medical Imaging Conference Record (NSS/MIC)*, pages 2825–2829. IEEE, October 2012. doi:10.1109/NSSMIC.2012.6551644. 34, 55

[76] Eiji Yoshida. **Parameter optimization of a digital photon counter coupled to a four-layered DOI crystal block with light sharing**. Submitted August 2014 to IEEE Transactions on Nuclear Science, under review, 2014. 34

[77] Herman T van Dam, Giacomo Borghi, Stefan Seifert, and Dennis R Schaart. **Sub-200 ps CRT in monolithic scintillator PET detectors using digital SiPM arrays and maximum likelihood interaction time estimation**. *Physics in Medicine and Biology*, **58**[10]:3243, 2013. 34

[78] Stefan Seifert, Gerben van der Lei, Herman T van Dam, and Dennis R Schaart. **First characterization of a digital SiPM based time-of-flight PET detector with 1 mm spatial resolution.** *Physics in medicine and biology*, **58**[9]:3061–74, May 2013. doi:10.1088/0031-9155/58/9/3061. 34

[79] Carsten Degenhardt, Pedro Rodrigues, Andreia Trindade, Ben Zwaans, Oliver Mulhens, Ralf Dorscheid, Andreas Thon, Andre Salomon, and Thomas Frach. **Performance evaluation of a prototype**

Positron Emission Tomography scanner using Digital Photon Counters (DPC). In *2012 IEEE Nuclear Science Symposium and Medical Imaging Conference Record (NSS/MIC)*, pages 2820–2824. IEEE, October 2012. doi:10.1109/NSSMIC.2012.6551643. 34

[80] Samuel España, Radoslaw Marcinkowski, Vincent Keereman, Stefaan Vandenberghe, and Roel Van Holen. **DigiPET: sub-millimeter spatial resolution small-animal PET imaging using thin monolithic scintillators.** *Physics in medicine and biology*, **59**[13]:3405–20, July 2014. doi:10.1088/0031-9155/59/13/3405. 34

[81] B Weissler, P Gebhardt, P Diippenbecker, B Goldschmidt, A Salomon, D Schug, J Wehner, C Lerche, D Wirtz, W Renz, K Schumacher, B Zwaans, P Marsden, F Kiessling, and V Schulz. **Design concept of world's first preclinical PET/MR insert with fully digital silicon photomultiplier technology**. In *Nuclear Science Symposium and Medical Imaging Conference (NSS/MIC), 2012 IEEE*, pages 2113–2116, 2012. doi:10.1109/NSSMIC.2012.6551484. 34

[82] Maria Georgiou, Giacomo Borghi, Spiridon V Spirou, George Loudos, and Dennis R Schaart. **First performance tests of a digital photon counter (DPC) array coupled to a CsI(Tl) crystal matrix for potential use in SPECT.** *Physics in medicine and biology*, **59**[10]:2415–30, May 2014. doi:10.1088/0031-9155/59/10/2415. 34

[83] Carmen Bouckaert, Stefaan Vandenberghe, and Roel Van Holen. **Influence of temperature on digital photon counter performance for SPECT**. *EJNMMI Physics*, **1**[Suppl 1]:A23, 2014. doi:10.1186/2197-7364-1-S1-A23. 34

[84] K Shimazoe, T Orita, H Takahashi, I Somlai-Schweiger, F R Schneider, S I Ziegler, and K Kamada. **Development of a Compton Camera based on digital SiPMs and GAGG crystals**. In *2013 IEEE Nuclear Science Symposium and Medical Imaging Conference (2013 NSS/MIC)*, pages 1–3. IEEE, October 2013. doi:10.1109/NSSMIC.2013.6829616. 34

[85] T Frach. **Optimization of the digital Silicon Photomultiplier for Cherenkov light detection**. *Journal of Instrumentation*, **7**[01]:C01112–C01112, January 2012. doi:10.1088/1748-0221/7/01/C01112. 34

[86] S Mandai and E Charbon. **A 4×4×416 digital SiPM array with 192 TDCs for multiple high-resolution timestamp acquisition**. *Journal of*

Instrumentation, **8**[05]:P05024–P05024, May 2013. doi:10.1088/1748-0221/8/05/P05024. 34, 79

[87] M.-A. Tétrault, É.D. Lamy, A. Boisvert, C. Thibaudeau, F. Dubois, R Fontaine, and J.-F. Pratte. **Real-Time Discrete SPAD Array Readout Architecture for Time of Flight PET**. Submitted June 2014 to IEEE Transactions on Nuclear Science, under review, 2014. 34

[88] Leo H C Braga, Leonardo Gasparini, Lindsay Grant, Robert K Henderson, Nicola Massari, Matteo Perenzoni, David Stoppa, and Richard Walker. **A Fully Digital 8×16 SiPM Array for PET Applications With Per-Pixel TDCs and Real-Time Energy Output**. *IEEE Journal of Solid-State Circuits*, **49**[1]:301–314, January 2014. doi:10.1109/JSSC.2013.2284351. 34

[89] Digital Photon Counting Philips. **Digital Silicon Photomultiplier**. 35

[90] Saint-Gobain. **PreLude 420 Datasheet**. 36

[91] Crystals&Applications. **Ce:GAGG scintillator**. 36

[92] Dow Corning. **DOW CORNING (R) 1-2577 CONFORMAL COATING**, 2013. 36

[93] Florian Schneider, Kenji Shimazoe, Ian Somlai Schweiger, Kei Kamada, Hiroyuki Takahashi, and Sibylle Ziegler. **A PET prototype based on digital SiPMs and GAGG scintillators**. *J NUCL MED MEETING ABSTRACTS*, **54**[2MeetingAbstracts]:429, 2013. 37, 57

[94] Rene Brun and Fons Rademakers. **ROOT An object oriented data analysis framework**. *Nuclear Instruments and Methods in Physics Research Section A: Accelerators, Spectrometers, Detectors and Associated Equipment*, **389**[1-2]:81–86, April 1997. doi:10.1016/S0168-9002(97)00048-X. 38

[95] T Szczesniak, M Kapusta, M Moszynski, M Grodzicka, M Szawlowski, D Wolski, J Baszak, and N Zhang. **MPPC Arrays in PET Detectors With LSO and BGO Scintillators**. *IEEE Transactions on Nuclear Science*, **60**[3]:1533–1540, June 2013. doi:10.1109/TNS.2013.2251002. 38

[96] J Pulko, F R Schneider, A Velroyen, D Renker, and S I Ziegler. **A Monte-Carlo model of a SiPM coupled to a scintillating crystal**. *Journal of Instrumentation*, **7**[02]:P02009–P02009, February 2012. doi:10.1088/1748-0221/7/02/P02009. 38

[97] A.L. Lacaita, F. Zappa, Stefano Bigliardi, and M. Manfredi. **On the bremsstrahlung origin of hot-carrier-induced photons in silicon devices**. *Electron Devices, IEEE Transactions on*, **40**[3]:577–582, Mar 1993. doi:10.1109/16.199363. 40

[98] A. Vacheret, G.J. Barker, M. Dziewiecki, P. Guzowski, M.D. Haigh, B. Hartfiel, A. Izmaylov, W. Johnston, M. Khabibullin, A. Khotjantsev, Yu. Kudenko, R. Kurjata, T. Kutter, T. Lindner, P. Masliah, J. Marzec, O. Mineev, Yu. Musienko, S. Oser, F. Retire, R.O. Salih, A. Shaikhiev, L.F. Thompson, M.A. Ward, R.J. Wilson, N. Yershov, K. Zaremba, and M. Ziembicki. **Characterization and simulation of the response of Multi-Pixel Photon Counters to low light levels**. *Nuclear Instruments and Methods in Physics Research Section A: Accelerators, Spectrometers, Detectors and Associated Equipment*, **656**[1]:69 – 83, 2011. doi:http://dx.doi.org/10.1016/j.nima.2011.07.022. 41, 106

[99] K Kamada, T Yanagida, J Pejchal, M Nikl, T Endo, K Tsutumi, Y Fujimoto, A Fukabori, and A Yoshikawa. **Scintillator-oriented combinatorial search in Ce-doped (Y,Gd) 3 (Ga,Al) 5 O 12 multicomponent garnet compounds**. *Journal of Physics D: Applied Physics*, **44**[50]:505104, December 2011. doi:10.1088/0022-3727/44/50/505104. 59

[100] W.W. Moses and M Ullisch. **Factors influencing timing resolution in a commercial LSO PET camera**. *IEEE Transactions on Nuclear Science*, **53**[1]:78–85, February 2006. doi:10.1109/TNS.2005.862980. 61

[101] P Lecoq, E Auffray, S Brunner, H Hillemanns, P Jarron, A Knapitsch, T Meyer, and F Powolny. **Factors Influencing Time Resolution of Scintillators and Ways to Improve Them**. *IEEE Transactions on Nuclear Science*, **57**[5]:2411–2416, October 2010. doi:10.1109/TNS.2010.2049860. 61, 62, 63

[102] R Dolenec, S Korpar, P Krizan, R Pestotnik, A Stanovnik, and R Verheyden. **Time-of-flight measurements with Cherenkov photons produced by 511 keV photons in lead crystals**. In *IEEE Nuclear Science Symposuim & Medical Imaging Conference*, pages 280–284. IEEE, October 2010. doi:10.1109/NSSMIC.2010.5873765. 61, 62, 66

[103] P. Cerenkov. **Visible Radiation Produced by Electrons Moving in a Medium with Velocities Exceeding that of Light**. *Physical Review*, **52**[4]:378–379, August 1937. doi:10.1103/PhysRev.52.378. 62

[104] S E Brunner, L Gruber, J Marton, K Suzuki, and A Hirtl. **Studies on the Cherenkov Effect for Improved Time Resolution of TOF-PET**. *IEEE Transactions on Nuclear Science*, **61**[1]:443–447, February 2014. doi:10.1109/TNS.2013.2281667. 62

[105] W.W. Moses and S.E. Derenzo. **Prospects for time-of-flight PET using LSO scintillator**. *IEEE Transactions on Nuclear Science*, **46**[3]:474–478, June 1999. doi:10.1109/23.775565. 62

[106] Matthew W Fishburn and Edoardo Charbon. **System Tradeoffs in Gamma-Ray Detection Utilizing SPAD Arrays and Scintillators**. *IEEE Transactions on Nuclear Science*, **57**[5]:2549–2557, October 2010. doi:10.1109/TNS.2010.2064788. 62

[107] Manabu Miyata, Hideki Tomita, Kenichi Watanabe, Jun Kawarabayashi, and Tetsuo Iguchi. **Development of TOF-PET using Cherenkov Radiation**. *Journal of Nuclear Science and Technology*, **43**[4]:339–343, April 2006. doi:10.1080/18811248.2006.9711101. 62, 66

[108] James William Rohlf. *Modern Physics from aα to Z*. Wiley, 1994. 64

[109] S Agostinelli, John Allison, K. Amako, J Apostolakis, H Araujo, P Arce, M Asai, D Axen, S Banerjee, G Barrand, F. Behner, L. Bellagamba, J. Boudreau, L. Broglia, A. Brunengo, H. Burkhardt, S. Chauvie, J. Chuma, R. Chytracek, G. Cooperman, G. Cosmo, P. Degtyarenko, A. Dell'Acqua, G. Depaola, D. Dietrich, R. Enami, A. Feliciello, C. Ferguson, H. Fesefeldt, G. Folger, F. Foppiano, A. Forti, S. Garelli, S. Giani, R. Giannitrapani, D. Gibin, J.J. Gómez Cadenas, I. González, G. Gracia Abril, G. Greeniaus, W. Greiner, V. Grichine, A. Grossheim, S. Guatelli, P. Gumplinger, R. Hamatsu, K. Hashimoto, H. Hasui, A. Heikkinen, A. Howard, V. Ivanchenko, A. Johnson, F.W. Jones, J. Kallenbach, N. Kanaya, M. Kawabata, Y. Kawabata, M. Kawaguti, S. Kelner, P. Kent, A. Kimura, T. Kodama, R. Kokoulin, M. Kossov, H. Kurashige, E. Lamanna, T. Lampén, V. Lara, V. Lefebure, F. Lei, M. Liendl, W. Lockman, F. Longo, S. Magni, M. Maire, E. Medernach, K. Minamimoto, P. Mora de Freitas, Y. Morita, K. Murakami, M. Nagamatu, R. Nartallo, P. Nieminen, T. Nishimura, K. Ohtsubo, M. Okamura, S. O'Neale, Y. Oohata, K. Paech, J. Perl, A. Pfeiffer, M.G. Pia, F. Ranjard, A. Rybin, S. Sadilov, E. Di Salvo, G. Santin, T. Sasaki, N. Savvas, Y. Sawada, S. Scherer, S. Sei, V. Sirotenko, D. Smith,

N. Starkov, H. Stoecker, J. Sulkimo, M. Takahata, S. Tanaka, E. Tcherniaev, E. Safai Tehrani, M. Tropeano, P. Truscott, H. Uno, L. Urban, P. Urban, M. Verderi, A. Walkden, W. Wander, H. Weber, J.P. Wellisch, T. Wenaus, D.C. Williams, D. Wright, T. Yamada, H. Yoshida, and D. Zschiesche. **Geant4a simulation toolkit**. *Nuclear Instruments and Methods in Physics Research Section A: Accelerators, Spectrometers, Detectors and Associated Equipment*, **506**[3]:250–303, July 2003. doi:10.1016/S0168-9002(03)01368-8. 65

[110] J.-F. Carrier, L Archambault, L Beaulieu, and R Roy. **Validation of GEANT4, an object-oriented Monte Carlo toolkit, for simulations in medical physics**. *Medical Physics*, **31**[3]:484, 2004. doi:10.1118/1.1644532. 65

[111] G.A.P. Cirrone, G Cuttone, F. Di Rosa, L Pandola, F Romano, and Q Zhang. **Validation of the Geant4 electromagnetic photon cross-sections for elements and compounds**. *Nuclear Instruments and Methods in Physics Research Section A: Accelerators, Spectrometers, Detectors and Associated Equipment*, **618**[1-3]:315–322, June 2010. doi:10.1016/j.nima.2010.02.112. 65

[112] K Amako, S Guatelli, V Ivanchencko, M Maire, B Mascialino, K Murakami, L Pandola, S Parlati, M.G. Pia, M Piergentili, T Sasaki, and L Urban. **Geant4 and its validation**. *Nuclear Physics B - Proceedings Supplements*, **150**[0]:44–49, January 2006. doi:10.1016/j.nuclphysbps.2004.10.083. 65

[113] N Akchurin, L Berntzon, A Cardini, G Ciapetti, R Ferrari, G Gaudio, J Hauptman, H Kim, F Lacava, L La Rotonda, M Livan, E Meoni, H Paar, A Penzo, D Pinci, A Policicchio, S Popescu, G Susinno, Y Roh, W Vandelli, and R Wigmans. **Čerenkov light contribution in lead tungstate crystals**. *Journal of Physics: Conference Series*, **110**[9]:92034, May 2008. doi:10.1088/1742-6596/110/9/092034. 66

[114] S Baccaro, L M Barone, B Borgia, F Castelli, F Cavallari, F de Notaristefani, M Diemoz, R Faccini, A Festinesi, and E Leonardi. **Optical properties of lead tungstate (PbWO4) crystal for LHC em-calorimetry**. Technical report, Citeseer, 1995. 66

[115] Inc. Wolfram Research. **Mathematica, Version 9.0**, 2012. 66

[116] Harry van der Graaf, Michiel Bakker, Hong Wah Chan, Edoardo Charbon, Fabio Santagata, Pasqualina Sarro, and Dennis Schaart. **The Tipsy single soft photon detector and the Trixy ultrafast tracking detector**. *2012 IEEE Nuclear Science Symposium and Medical Imaging Conference Record (NSS/MIC)*, **8**[01]:1952–1956, October 2012. doi:10.1109/NSSMIC.2012.6551451. 79

[117] Jeffrey P Schmall, Junwei Du, Martin S Judenhofer, Purushottam Dokhale, James Christian, Mickel McClish, Kanai S Shah, and Simon R Cherry. **A Study of Position-Sensitive Solid-State Photomultiplier Signal Properties**. *IEEE Transactions on Nuclear Science*, **61**[3]:1074–1083, June 2014. doi:10.1109/TNS.2014.2302635. 79

[118] I Sacco, P Fischer, A Gola, and C Piemonte. **Interpolating Silicon Photo-Multiplier: A novel position sensitive device with submillimeter spatial resolution and depth of interaction capability**. In *2013 IEEE Nuclear Science Symposium and Medical Imaging Conference (2013 NSS/MIC)*, pages 1–3. IEEE, October 2013. doi:10.1109/NSSMIC.2013.6829589. 79

[119] Takashi Okamoto, Kibou Ote, Koichi Sakai, Akihiro Noda, Keiji Shimizu, Keisuke Masuda, Tomohide Ohmura, and Mitsuo Watanabe. **An animal PET scanner using flat-panel position-sensitive PMTs.** *Annals of nuclear medicine*, **28**[1]:74–80, January 2014. doi:10.1007/s12149-013-0772-y. 79

Declaration

I hereby confirm that the content of this thesis entitled "Novel High Resolution Photon Detectors for PET Imaging", which is submitted by me in partial fulfillment of the requirement for the degree of doctor of Philosophy (Ph.D.), is the result of only my original work and due acknowledgement has been made in the text to all other material used.

Munich, November 7th 2014

Ian Andreas Somlai Schweiger